Recombination Dynamics in Zinc Oxide

Luigi Santamaria Amato

Ph.D. Candidate (XXIII cycle)

Tutors: Prof. P. Maddalena

Dr. S. Lettieri

Referees: Prof. L. Marrucci

Prof. D. Ninno

Introduction

Chapter 1

Zinc Oxide

1.1 ZnO-based applications

1.2 Crystal structure

1.3 Optical properties

1.4 Defects

1.5 Defects related emission

1.6 Effect of annealing on ZnO optical properties

1.7 High injection effects in ZnO

1.8 Stimulated emission in ZnO

Chapter 2

Photoluminescence

2.1 What is photoluminescence?

2.2 Emission and absorption

2.3 Summation over states

2.4 Discrete-continuum transitions

2.5 Continuum-continuum transitions

2.6 Relation between absorption and emission

2.7 Total emission rate and lifetime

2.8 Instantaneous τ_{eff}

2.9 Non-radiative recombination processes

2.10 Exciton

2.11 High injection effects in semiconductor

Chapter 3

Experimental Set-up

3.1 Nd:YAG laser

3.2 Streak

3.3 Spectrometer

3.4 CCD

3.5 Acquisition software

Chapter 4

Gas Sensing Applications

4.1 Adsorption and Langmuir model

4.2 Static quenching and dynamical quenching

4.3 Gas-induced PL quenching effects

4.4 Gas exposure effect on recombination lifetime

Chapter 5

Visible and UV emission in nanowires

5.1 Correlation between UV and visible emission

5.2 Three bands Model

5.3 Empirical test of three bands model

5.4 Visible emission in nanowires

5.5 UV emission in nanowires

Chapter 6

ZnO bulk

6.1 High injection effects

6.2 Generalization of τ_{eff}

6.3 Measure of material parameters by TRPL

6.4 Multi fitting procedure and competitive recombination channels

6.5 Oxygen annealing

6.6 Multi fitting extension

Conclusions

Introduction

Since the invention of the first semiconductor transistor in 1947, by the scientists of Bell Labs, the semiconductor industry has grown at an incredible rate, fabricating faster, smaller, more powerful and cheaper devices.

Due to the maturity of its fabrication technology, silicon continues to dominate the present commercial market in discrete devices and integrated circuits for computing, power switching, data storage and communication. For high-speed and optoelectronic devices such as high-speed integrated circuits and laser diodes, gallium arsenide (GaAs) is the material of choice. It exhibits superior electron transport properties and special optical properties. GaAs is a direct bandgap semiconductor, whereas Si is indirect, hence making GaAs better suited for optoelectronic devices. However, physical properties required for high power, high temperature electronics and UV/blue light emitter applications are beyond the limits of Si and GaAs. It is essential to investigate alternative materials in order to achieve these devices. Wide bandgap semiconductors exhibit inherent properties such as larger bandgap, higher electron mobility and higher breakdown field strength. Therefore, they are suitable for high power, high temperature electronic devices and short wavelength optoelectronics. Zinc oxide (ZnO) is a direct, wide bandgap semiconductor material with many promising properties for blue/UV optoelectronics, transparent electronics, spintronic devices and sensor applications.

In this work I will show some experimental results concerning with possible gas sensing applications of ZnO nanowires. Then will be shown some experimental results related to optical properties of this material confirming it as promising material for optoelectronics.

Moreover some models will be described to show that it is possible to use time resolved photoluminescence measurements (TRPL) to obtain information on semiconductor materials, then these models will be tested on ZnO bulk crystal.

Chapter 1

Zinc Oxide

In this thesis the optical properties of ZnO were studied but this material is a reference material for many applications in several fields of science and technology. For this reason in the first chapter I will show some applications of this semiconductor related to electrical, mechanical and optical properties to point out the results obtained in last few years and, at same time, to identify future areas that need work.

1.1 ZnO-based applications

Zinc Oxide, in polycrystalline form, was used in the past in a wide range of applications as facial powders, sunscreens, catalysts, paint pigmentation, piezoelectric transducers, varistors, and as transparent conducting electrodes. Only in few last year also the research is looking ZnO as material for application in several research fields. In fact, due to some of its properties as wide and direct bandgap, ZnO has numerous attractive characteristics for electronics and optoelectronics devices. The ZnO bandgap is 3.36 eV then it is transparent at visible light and suitable for application as light emitter in blue/near UV region. The exciton binding energy is 60 meV so the exciton is well separated from conduction band also at room temperature (kT_{Room}=25 meV) moreover the higher

binding energy, compared with other direct and wide bandgap materials as GaAs, enhances the efficiency of light emission.

This material shows also a low threshold for optical pumping and may be promising for laser fabrication using ZnO as active media moreover its biocompatibility justifies the research interest for this semiconductor. This material shows also unfavorable features, the main problem is the difficult to produce p-doped ZnO, and it represents the main effort of now day research.

The realization of ZnO nanostructures is quite simple promoting it for inexpensive nanotechnology devices. These nanostructures, due to large surface/volume ratio, are ideal for gas sensing application.

ZnO has been effectively used as a gas sensor material based on the near-surface modification of charge distribution with certain surface absorbed species The reversible chemisorption of reactive gases at the surface of these metal oxides can produce a large and reversible variation of material conductance that is the main property of an electric gas sensor material.

Moreover ZnO shows also visible emission peak strongly dependent on environment condition that could be the essential feature for optical gas detection, in future.

This semiconductor is naturally n-doped because of intrinsic defects that enhance the conduction band electron density. The bangap is tunable between 3 and 4 eV by means of substitution on cation site of dopant elements as Cd^{2+} or Mg^{2+}. The renewed interest in this semiconductor has arisen out of the development of growth technologies for the fabrication of high quality single crystals and epitaxial layers, allowing for the realization of ZnO - based electronic and optoelectronic devices.

1.2 Crystal structure

ZnO has the wurtzite structure that is a compact hexagonal structure with base, the first neighbors are atoms of the other species and are placed on vertexes of tetrahedron, the second neighbors make the hexagonal structure. The crystal can be seen as many alternating planes composed by Zn^{2+} tetrahedrons and O^{2-} tetrahedrons with lattice parameters a=0.3296 nm and c = 0.5206 nm (figure 1.1).

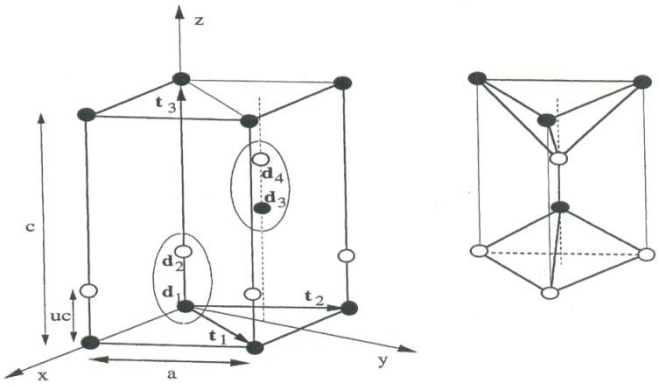

Figure 1.1 *The figure shows the structure of ZnO lattice*

A compact hexagonal in turn can be seen as two simple hexagonal lattices overlapped and translated or equivalently as a simple hexagonal lattice with base.

Every structure is uniquely identified by assigning three primitive translation vectors and the vectors of base that specifies the atoms position in primitive cell. Because in this case we have a compact hexagonal with base the base vectors are four.

The primitive translation vectors are:

$$t_1 = a\left(\frac{1}{2}, \frac{\sqrt{3}}{2}, 0\right) \qquad t_2 = a\left(-\frac{1}{2}, \frac{\sqrt{3}}{2}, 0\right) \qquad t_3 = c(0,0,1)$$

And base vector are:

$$d_1 = (0,0,0) \qquad d_2 = \left(0,0,\frac{3}{8}c\right) \qquad d_3 = \left(0,\frac{a}{\sqrt{3}},\frac{c}{2}\right) \qquad d_4 = \left(0,\frac{a}{\sqrt{3}},\frac{7}{8}c\right)$$

The crystal structure and ionic nature of bonding give to ZnO piezoelectricity properties, for this reason this material is a very interesting material also for applications as nanomechanical devices. It is important to underline the presence of polar planes caused by different charges of Zn and O ions that originates dipole momentum along c-axis with consequent surface charge density on planes of crystal perpendicular to c-axis. The four most common face terminations of ZnO are the polar Zn terminated (0001) and O terminated $(000\bar{1})$ faces (c-axis oriented), and the non-polar $(11\bar{2}0)$ (a-axis) and $(10\bar{1}0)$ faces which both contain an equal number of Zn and O atoms. Additionally, the polar surfaces and the $(10\bar{1}0)$ surface are found to be stable, however the $(11\bar{2}0)$ face is less stable and generally has a higher level of surface roughness than its counterparts. Tuning opportunely the growing velocity it's possible to obtain a variety of nanostructures.

1.3 Optical properties

ZnO is a direct bandgap semiconductor, the lowest conduction band level is constituted by 4s empty orbital of Zn^{2+} and by hybrid antibound orbital sp^3 while the valence band is constituted by occupied 2p orbital of O^{2-} and by hybrid bound orbital sp^3.

The valence band is split in three twofold sublevel due to spin-orbit coupling and due to splitting of intrinsic electric field.

These levels are called band A (heavy hole), band B (light hole), and C (crystal-field split band) the attribution of symmetry is still debated.

The transition between A or B valence band level and conduction band are allowed only for polarization parallel to c-axis instead transitions between C band and conduction band are possible only for polarization states perpendicular to c-axis.

Because the VB→CB transition is dipole allowed a generic photon with energy higher then bandgap can excite an electron to CB leaving an hole in valence band. These two particles, because of Coulomb interaction, will form free exciton states with energy placed under conduction band minimum. The possible exciton species are three because the valence band are three. In ZnO the exciton occurs as Wannier exciton where exciton Bohr radius (a_b~ 2 nm) [1] is bigger than lattice parameters.

The excitons are often bound to defects as explained in chap 2, in these kinds of exciton the translational degrees of freedom are off so the spectral width of emission is very small, and in low temperature condition it is possible observe several peaks between 3.35 and 3.37eV but the attribution of the peaks to particular bound exciton is difficult because the energy region is very thin and the emission energy of a particular complex can depend on synthesis method so different samples may show shifted wavelength of exciton emission .

1.4 Defects

ZnO is a good conductor at room temperature, the free electron density strongly depends on layer quality but usually is about 10^{17} cm^{-3} in undoped material. The donor states, responsible for this density, were attributed to several kind of intrinsic imperfection across the year.

In the past the donor states were attributed to intrinsic defects as O vacancy (V_O) and Zn interstitial (Zn_i). This statement was challenged by Kohan et al. [2] who calculated those states have a

formation energy very high so that it's very difficult to find them in measurable quantity. Moreover Kohan calculated also the energy level of this defects showing that they are deep defects and not shallow donors even if the theoretical calculations do not agree with experimental results.

Van de Walle suggested high concentration of donors was likely a dominant background donor in ZnO materials that were exposed to H during growth [3]. This proposal has been subjected to tests confirming shallow donors due to H exist in seeded chemical vapor transport (SCVT) grown ZnO [4,5,6] and can contribute significantly to its conductivity. This fact, coupled with the theoretical evidence of high formation energies for the native donors has led to a prevailing opinion that native donors do not play a significant role in the conductivity of as-grown ZnO.

The theoretical results are obtained on isolated defects and these results assert defects don't contribute to conduction electrons while defect complexes (two or more interacting defect) may contribute to density in conduction band.

Besides H there are many elements that can n-dope ZnO, the favorite elements are the group III elements as Al, Ga and In that substitute the Zn in lattice, using them it's possible to obtain a concentration larger than 10^{20} cm^{-3} [7].

The p-doping of ZnO is a very important research topic because the realization of UV LED, possible trough p-n junction, could have a very strong consequences in solid state industry.

Dopant elements of I group substituting for Zn or dopant elements of V group substituting for O should dope ZnO in p-type.

Two elements studied in past are Li and Na, theory predicts shallow acceptor levels for Li_{Zn} and Na_{Zn} [8,9] but they doesn't produce a considerable concentration of holes in valence band [10].

The theory predicts that many elements of group V produce deep acceptors [8] when they occupy the O location (P_O, As_O, Sb_O) but instead they produce a considerable concentration of holes in valence band [11,12]. Some explanations are exposed in literature but the p-doping of ZnO is nowadays an open problem.

The acceptor defects always present in ZnO for all kind of sample preparation are the Zn vacancy, they are the dominant acceptors in nominally undoped ZnO. The kind of defect listed above are point defects, but on crystal surface also other kind of defects are present as terraces and ledges.

Nowadays works studying these defects in ZnO don't exist but probably these defects (surface defects) affect the optical properties because the penetration length of these material (at photon energy larger than bandgap) is very small and then surface effects became important.

Nowadays it's clear that H and some elements of group III are background donors and contribute in a substantial way to electron conductivity instead regarding properly intrinsic defects it's very difficult to assert some ☒established theories.

The main examples, because simply producible, concern with Zn_I interstitial that doesn't contribute to conduction and V_O that produces deep levels according to theory [2] and to electron paramagnetic resonance (EPR) experiment.

Concerning with intrinsic acceptor, some studies [2] assert that O interstitial (O_I) probably behaves as acceptor but it is still an open problem. Instead much is known on zinc vacancy V_{Zn}, it behaves as acceptor and the small acceptors concentrations 10^{15} cm^{-3}, observed in many samples, can be completely explained by V_{Zn}- related defects [13].

In summary ZnO technology has improved in the last year but the main problem is the production of high conductivity p-type material. The theoretical open problem is to understand how P, As and Sb form acceptors and which lattice site each occupies.

1.5 Defects related emission

ZnO shows a non zero contribution also in visible part of spectrum, the attribution to particular defects it's very difficult because the relative intensity of visible bands depends on sample preparation, environment composition and temperature and in some case they overlap each other in some spectral region.

The ZnO visible bands are: the green band (2.5 eV), yellow band (2.2 eV) and red band (1.75 eV) observed only in particular conditions.

The strongest visible band is the green band, the origin of transitions involved in this emission was debated across the years and an universally accepted explanation is not still obtained. It is generated by defects near surface as can be seen by (figure 1.2)

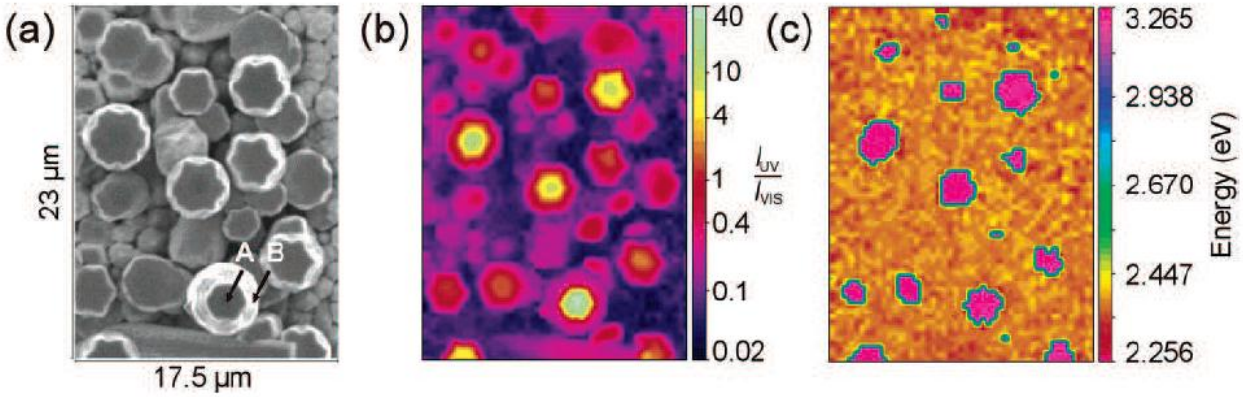

Figure 1.2 *The first picture shows a SEM image of ZnO micropillars the second one is a false color image representing the ratio* $\frac{I_{UV}(x,y)}{I_{vis}(x,y)}$ *(where x and y are the spatial dimensions) and the third picture shows a map of spectral maximum.*

In the figure the authors [26] show a SEM image of ZnO micropillars (figure 1.2a), a false color image (figure 1.2b) representing the ratio $\frac{I_{UV}(x,y)}{I_{vis}(x,y)}$ (where x and y are the spatial dimensions) and a map of spectral maximum (fig 1.2c), we can see that the ratio tend to zero near surfaces.

Some works ascribe this emission to donor-deep acceptor transitions (DAP) [14,15], the donor states placed some meV under conduction band and deep acceptor states about 0.8 eV above valence band, are due to zinc vacancies V_{Zn} .

Kohan and Ceder [2] ascribe green emission to transition between conduction band and deep acceptor due to V_{Zn} .

Korsunska and Borkovska carried out some measurements of luminescence applying a variable electric field to a ZnO samples and they argued green luminescence band is due to transitions between donor levels, generated by zinc interstitial (Zn_i), and holes in valence band.

Another possible transition involved in GL is a transition between conduction band and O_{Zn} deep acceptor as suggested by Lin and Fu [16].

The previous explanation concern only intrinsic defects but there are some evidences that defects states, originated by extrinsic doping, are partly responsible for GL.

Garces et al., [17] studying PL of a bulk ZnO sample before and after annealing in air at 900◦C for one hour, observed a remarkable transformation of a broad structureless green band peaking at 500 nm into a structured emission peaking near 510 nm with a structure identical to the Cu related GL. These authors suggested that there might be two distinct mechanisms giving rise to GL band, and that both involve Cu impurities but with different stable charge states (Cu^+ and Cu^{2+}). Based on their EPR study on several samples they concluded that the structureless GL band of the as-grown ZnO sample is due to DAP recombination between an electron bound to a shallow donor and a hole loosely bound to the Cu^+ ion before annealing, while the structured green emission after the 900◦C annealing was assigned to localized excitation of the isolated Cu^{2+} ion.

Another band, characteristic of ZnO emission, is the yellow band centered at 2.2eV with a FWHM of 0.5eV, its temporal dynamic is slower then green band dynamic after excitation source off.

In Li doped ZnO samples the yellow band is increased and the intensity increases as temperature decreases, this band is probably originated by DAP transition between shallow donor and deep acceptor (Li_{Zn}) that dominate at low temperature as observed by optical detected magnetic resonance measurement (ODMR) [18].

The yellow band and relative properties are observed also in undoped crystals this band saturates before green band as pump power increases indicating low concentrations of the related defects. Instead if sample is irradiated for long time the yellow band increases and green luminescence gradually bleached.

The last spectral region where an emission is present is the red region in fact a band centered at 1.75eV appears in undoped crystals after annealing in air. This band is observable only at very low temperature when temperature increases the red band quenching causes the appearance of green band it may be a result of competition for holes between the acceptors responsible for green and red band.

In summary because of many degrees of freedom it's very difficult to assign each band to a specified transition, probably the emission of a given band is the sum of contributions due to many of transitions above explained and a generic transition is more or less important apiece the sample preparation.

1.6 Effect of annealing on ZnO optical properties

Several studies concerning with annealing effects on ZnO electrical and optical properties were carried out over the years. The annealing is a process where a sample is heat up in a controlled environment conditions. For sake of simplicity, we consider only annealing process in air, oxygen and vacuum.

When a ZnO crystal is annealed in air at temperature higher than 600 C, the transmittance spectrum changes because the absorption becomes non-zero at 550 nm and it causes the crystal to appear yellow. The reason is the appearance of deep acceptors states originated by nitrogen as demonstrated by Garces and Giles trough EPR measurements [19] moreover Hall effect measurements, after annealing in air, demonstrated the decreasing of free electron concentration due to diminishing of shallow neutral donor states in fact nitrogen acceptors compensate a portion of the donors because nitrogen are in non-paramagnetic ionized state N^-.

If the sample is exposed to yellow light (or a more energetic one) some of nitrogen acceptor are converted to the paramagnetic neutral acceptor state N^0 with transition of electron to shallow donors.

The influence of annealing in air was studied also in nanostructured systems, in these case the produced effects depends on nanostructures type, however usually the intensity of exciton emission enhances as annealing temperature increases [20,21] and FWHM decreases. The reason of FWHM decreasing is probably due to diffusion of Zn interstitials from the ZnO lattice that induce ordering in the intrinsic defects, which would lead to a decrease of the number of non-radiative recombination centers and to a greater definition of the exciton-binding donor levels [22].

The intensity of green and yellow bands also increases but their ratio is not a constant in fact the green emission increases faster [23] and its position depend on annealing temperature.

Concerning with effects of annealing in oxygen and vacuum environment, an interesting work was carried out by Wang and Seo [24] on nanorods sample. They demonstrated that annealing in oxygen decreases the ratio between exciton emission and visible emission I_{UV}/I_{Vis} and the annealing in vacuum increases it. To gain information about density of oxygen vacancy the same annealing process performed on nanorods was performed on bulk crystals measuring a diminishing of electrical resistivity after vacuum annealing and an increasing after oxygen annealing. These measurement suggest that green luminescence is not generated by oxygen vacancy even if other evidences suggest that it is a surface phenomenon [25, 26].

Wang and Seo proposed a model to explain the I_{UV}/I_{Vis} behavior after annealing in oxygen and vacuum, which explains also other effect such as UV illumination enhanced photoluminescence and faster intensity saturation of green luminescence as pump power increases in comparison of UV luminescence. Because of oxygen annealing an amount of O^{2-} ions is chemisorbed at surface, the adsorbed oxygen provoke an upward band bending of ZnO [27]. After optical excitation, the photogenerated electrons and holes are swept to opposite directions across the depletion region so, in this region the probability of recombination via excitonic process is reduced. The electric field in depletion region sweeps the impurity as Cu^{+} or Zn_i to the surface [28] so the holes, before reaching the O^{2-} on surface, can recombine with deep level defect states, as Cu^{+}, to generate green luminescence explaining the I_{UV}/I_{Vis} variation before and after annealing. The holes that don't recombine and reach the surface are captured by adsorbed oxygen ion, followed by transforming into physisorbed state. The physisorbed oxygen is less stable and is prone to be desorbed from the surface, thus reducing the thickness of depletion layer explaining also the UV illumination enhanced PL effect [29].An opposite situation happens when the annealing is performed in vacuum reducing the density of chemisorbed O^{2-} in un-annealed sample as showed in figure 1.3. The figure shows the band diagram in an un-annealed sample, in an annealed in oxygen sample and in annealed in vacuum sample.

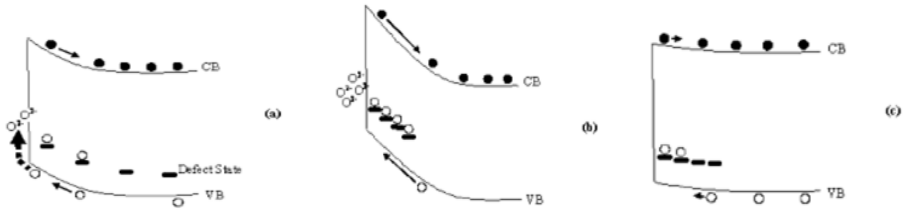

Figure 1.3 *This figure shows the band diagram in an un-annealed sample (a) , in an annealed in oxygen sample (b) and in annealed in vacuum sample (c).*

1.7 High injection effects in ZnO

The study of ZnO behavior under different carrier concentration is needful to tune ZnO properties and to optimize device performances.

A first carrier concentration effect regards the bandgap width and may be used to work on bandgap engineering, in fact, the distance between conduction band minimum and valence band maximum decreases if doping increases because of band gap renormalization due to exchange interaction (see chap 2). But, at same time, the exciton bound energy decreases because of screening effect that produces also an exciton resonance dumping also due to appearance of non-radiative recombination channels introduced by doping.

The previous effects regards emission but doping produces effects also on absorption spectrum in fact, for example, the enhancement of donors increases the Fermi energy with a subsequent raising of absorption wavelength (Burstein Moss effect see chapter 2).

Moreover to understand ZnO properties, useful to optoelectronic applications, the study of carrier dynamics after excitation with intense ultrafast laser pulses it is necessary.

Because of intense excitation, semiconductors undergo effects as melting, ablation, and resolidification, which modify material structure permanently.

For example figure 1.4 shows the surface permanent modification after strong laser exposure.

The typical ZnO applications do not require permanent changes in the material but many applications involve a large population of excited carriers. Lasers and waveguides depend on the carrier concentration and other material properties. It is so necessary to understand how ZnO behaves under high carrier densities over time in order to optimize ZnO-based devices.

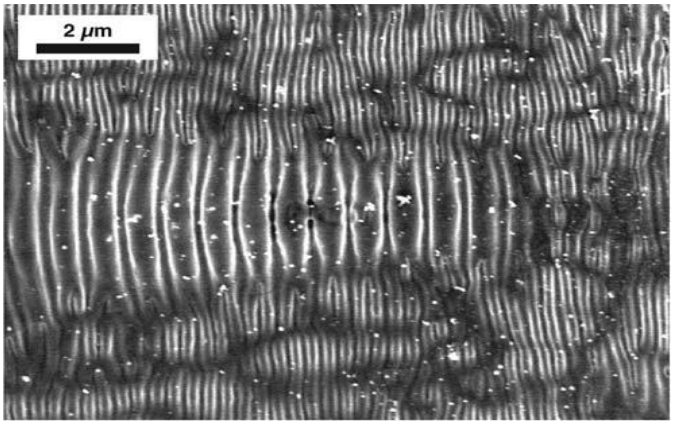

Figure 1.4 *SEM image of a bulk ZnO after strong laser exposure.*

All previous effect are observed in ZnO but obviously they depend on sample preparation and also on shape if the sample is nanostructured. Examining the dielectric function of bulk ZnO it is

possible to find some high excitation properties above described. Figure 1.5 represents the real and imaginary part of dielectric function at different time delay between a strong excitation pulse and the start of acquisition, the measure was performed by means of pump-probe reflectivity measure above bandgap energy [30].

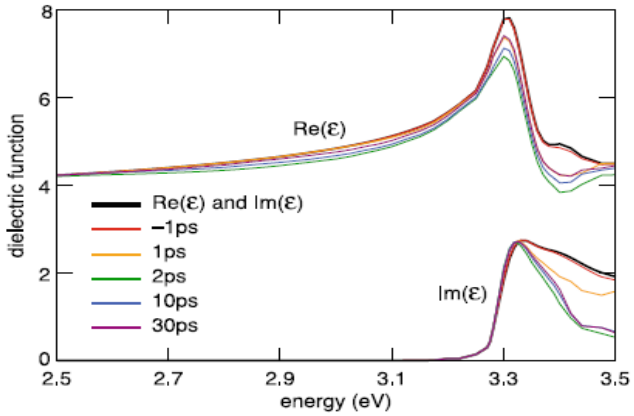

Figure 1.5 *Real and imaginary part of excited ZnO dielectric function at different time after excitation*

It can be noted that real part of dielectric function shows a 20% decreasing at 3.3eV, it means that after excitation the carrier density originates a screening that dumps the exciton resonance. Moreover the red shift of imaginary part of dielectric function gives information on band gap renormalization effect.

Change of properties was also observed due to carrier density originated by doping as Al [31], Sn [32], Ga [33]. In figure 1.6 the bandgap energy, measured by means of absorption spectrum, [31] is showed for several samples with different doping concentrations originating conduction band electron between $5*10^{18}$ and $1.5*10^{21}$ cm^{-3}.

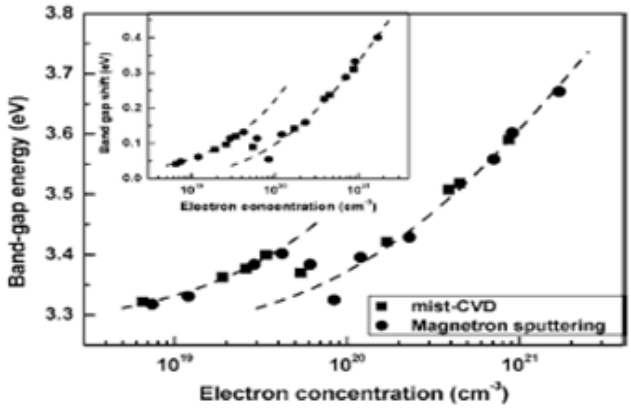

Figure 1.6. *The figure shows bandgap of ZnO samples with different doping concentrations. The bandgap is calculated using absorption measurement and the red shift due to Burstein-Moss effect is clear as doping concentration increases.*

The bandgap is almost constant until 6-7 *10^{18} cm^{-3} because, under this value, the density is lower than density of states in conduction band N_C ($N_C = \frac{2(2\pi m^* kT)^{3/2}}{h^3} \sim$ 4*10^{18} cm^{-3}[31]) .

The energy gap starts to increase with a rate proportional to $n^{2/3}$ (where n is the electron density in conduction band) until 4*$10^{19}$$cm^{-3}$ because of Burstein-Moss effect, in fact in this region the effect concerning with Mott transition are not observed but when density exceeds 4*10^{19} the energy gap shows a decreasing because of Mott transition, then after the density of 10^{20} cm^{-3} the bandgap starts to increase again but at difference rate because of two competitive effects (Burstein-Moss and Mott).

In ZnO at intermediate pumping rate, before to observe Mott transition, the emission spectrum shows a very sharp peak called p-line and due to exciton-exciton scattering.

When the exciton density it's large enough, the exciton-exciton scattering starts to appear. If the collision is elastic the initial energy will be equal to final energy otherwise if it is inelastic, two excitons for example in the fundamental state that hit each other will be scattered one to another energy value given by to Rydberg series or to continuum state (very probable at room temperature) and the other exciton will be scattered to an energy value given by following relation [34]:

$$E_{emission} = E_{exc}(n_B = 1) - E_{exc}^B \left(1 - \frac{1}{n_{B,f}^2}\right) - \frac{3}{2}kT \qquad (1.1)$$

Where exc is $E_{exc}(n_B = 1)$ is exciton energy in fundamental state, E_{exc}^B is exciton binding energy, $n_{B,f}$ is the quantum number of other exciton, k is the Boltzman constant and T is the absolute temperature.

At room temperature, neglecting BGR effect, $E_{emission}$ = 3.2 eV that is in a good agreement with experimental results as it can be seen by the figure 1.7 where the luminescence spectra at different pump energy measured at room temperature are shown [35].

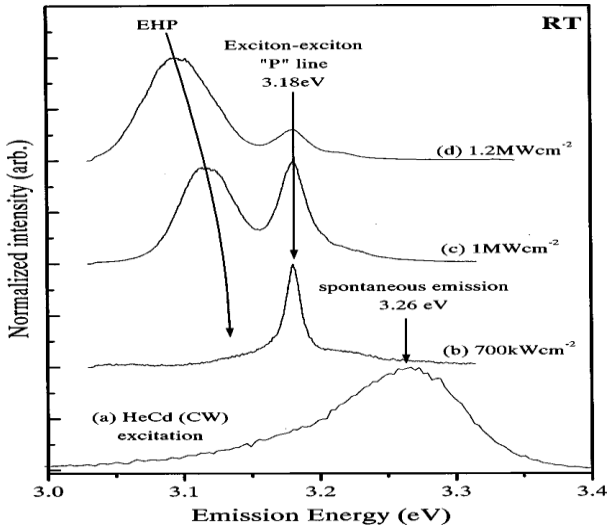

Figure 1.7. *The figure shows the emission spectrum of ZnO at different injection conditions.*

This p-line shows a large quantum efficiency and a very low stimulated emission threshold so it's very important for applications in the field of light emitting devices.

1.8 Stimulated emission in ZnO

The difficulty to produce p-doped ZnO implies difficulty to observe electrically pumped lasing in ZnO-based structures. Instead, stimulated emission induced by optical pumping was observed in several structures as for example epitaxial layers [35, 36]. The research aim regards the optimization of nanostructure parameters to enhance emission efficiency.

For wide band-gap semiconductor materials, an high carrier concentration is usually required to obtain lasing action by means of an electron-hole plasma (EHP) process. Such EHP mechanism, which is common for conventional laser diode operation, typically requires high lasing threshold. As an alternative to EHP process, excitonic recombination in semiconductors is a more efficient radiative process and can facilitate low-threshold stimulated emission. To achieve efficient excitonic laser action at room temperature, the binding energy of the exciton must be much greater than the thermal energy at room temperature and this is the case of ZnO.

Concerning the shape of structures many works assert the nanowires are probably the most efficient nanostructure to obtain optical amplification.

A frequently observed process in nanowires [37] is the amplified spontaneous emission (ASE), when the spontaneously emitted photons pass through a long gain medium, the spontaneous emission may be strongly amplified through a stimulated process in the gain medium. As a result, the spectrum becomes narrower and the output power becomes more intense in comparison with spectrum of unamplified spontaneous emission, and beam quality is also close to conventional laser. It is different from the general laser because no cavity configuration for positive feedback is required for ASE generation and therefore no longitudinal and transverse modes appear in the output light. As a good natural waveguide in air, one-dimensional ZnO nanomaterials are beneficent to confine and amplify the spontaneous emission.

Stimulated emission was recently observed in a single nanowires [38]. They observed the total emitted intensity as function of pump intensity and it shows a linear dependence al low injection regime, a superlinear one (that is the lasing threshold) in intermediate region, and again a linear behavior in high energy region. The threshold dependence on longitudinal and transverse dimension was studied treating the nanowire as a cavity.

They observed emission occurs trough end facets of nanowire and observed equispatial modes related to round trip of nanowire, carrying out measurement on many nanowires they observed enhancement of laser effect when longitudinal dimension (L) enhances and transversal (D) dimension decreases but when D is lower than 150nm the nanowire doesn't reach threshold for any longitudinal dimension.

Emission induced by electrical pumping has never been observed in pure ZnO structure but very recently was observed [39] in heterostructures where the n-doped material was a ZnO nanowire and the p-doped material was an heavily p-doped Si.

Chapter 2

Photoluminescence

This chapter describes the phenomenon of photoluminescence from a theoretical point of view then PL theory is applied to particular case of semiconductor materials. The same phenomenon is discussed in non equilibrium condition and a general method to obtain information about some material parameters, by means of time resolved photoluminescence measurements, is exposed for the ideal case (constant quantum efficiency). In the last part of chapter the high injection effects are shown from a theoretical point of view.

2.1 What is photoluminescence?

The term photoluminescence refers to emission of optical incoherent radiation by a physical system which is made out of equilibrium by radiation. The phenomenon is divided in three different temporal stages:

1) Out of equilibrium electron-hole pairs creation through radiation absorption
2) Relaxation to quasi-equilibrium through phonon collisions and electron-electron collisions
3) Radiative recombination of pairs

After the first stage, the excited pairs density in a layer placed at sample surface with a depth of about a penetration length is higher than density in bulk.
Diffusive processes in competition with recombination processes rule the evolution of pairs density, all these processes try to restore the equilibrium.
Moreover the material may re-adsorb the radiation generated by radiative recombination (auto-adsorption)
Main contribution of photoluminescence is due to portion of material next to surface then,
in many experiment, the detection is carried out on same surface on which the excitation occurs (front surface photoluminescence).
It is possible to acquire signal on back side (transmission photoluminescence) only when samples have thickness lower than penetration length.

2.2 Emission and absorption

The interaction between a classic electromagnetic field (at optical frequency) and a quantum electron is described at microscopic scale through the following Hamiltonian (quadratic term is neglected):

$$H_1 = -\left(\frac{e}{mc}\right)\boldsymbol{A}\cdot\boldsymbol{p}$$

where $\boldsymbol{A}$ is the vector potential and $\boldsymbol{p}$ is the electron momentum. Expanding vector potential in plane waves, the Hamiltonian becomes:

$$H_1 = \sum_{\lambda} H_{\lambda}^{ab}\, exp(-i\omega_{\lambda}t) + \sum_{\lambda} H_{\lambda}^{em}\, exp(i\omega_{\lambda}t)$$

where:

$$H_{\lambda}^{ab,em} = -\left(\frac{e}{mc}\right) A_{0\lambda} exp\,[\pm(i\boldsymbol{k_{\lambda}}\cdot\boldsymbol{r})]\,\hat{\boldsymbol{\varepsilon}}_{\boldsymbol{\lambda}}\cdot\boldsymbol{p}$$

and the sum index λ includes two polarization directions and $\hat{\boldsymbol{\varepsilon}}_{\boldsymbol{\lambda}}$ is polarization versor, ω is the frequency and $\boldsymbol{k}$ is the wave vector. Using time dependent perturbation theory we find that two hamiltonian terms represent the photon emission and absorption.
The number of transitions per unit time is given by:

$$W_{ab,em} = \left(\frac{2\pi}{\hbar}\right)\sum_{\lambda}\sum_{i,f}|\langle f|H^{ab,em}|i\rangle|^2\,\delta(E_{f,\lambda} - E_{i,\lambda})$$

Where i and f refer to initial and final state and sum is performed on all degenerate components of initial and final state.

$E_{f,\lambda}$ and $E_{i,\lambda}$ are the initial and final energies of system e.m. field + electron

$$E_{j,\lambda} = E_j + N_{j,\lambda}\hbar\omega_\lambda$$

where $N_{l,\lambda}$ is the occupation number of λ mode.

Absorption represents the transition between initial low energy state (l) and final high energy state (u) by means photon. The opposite situation occurs for emission.

$$E_{l,\lambda} = E_l + N_{l,\lambda}\hbar\omega_\lambda$$
$$E_{u,\lambda} = E_u + (N_{l,\lambda} - 1)\hbar\omega_\lambda$$

defining:

$$\left|P_{ul}^{ab,em}\right| = |\langle u,l|exp\,[\pm(i\boldsymbol{k_\lambda}\cdot\boldsymbol{r})]\,\hat{\boldsymbol{\varepsilon}}_\lambda\cdot\boldsymbol{p}|l,u\rangle|$$

the absorption and emission rates became:

$$W_{ab,em} = \pm\left(\frac{2\pi e^2}{\hbar m^2 c^2}\right)\sum_{\lambda}|A_{0\lambda}|^2\sum_{u,l}|P_{ul}^{ab,em}|^2\,\delta(E_{ul} - \hbar\omega_\lambda)$$

Using the relation between electric field and vector potential $\boldsymbol{E} = -\frac{1}{c}\frac{\partial \boldsymbol{A}}{\partial t}$ it is possible to calculate the expression of energy density U_λ:

$$U_\lambda = \frac{\varepsilon_r}{4\pi}\langle|Re[\boldsymbol{E}_\lambda]|^2\rangle = \frac{\varepsilon_r\omega_\lambda^2}{2\pi c^2}|A_{0\lambda}|^2$$

As the energy density of λ mode is $U_\lambda = N_\lambda\hbar\omega_\lambda$, also we have:

$$|A_{0\lambda}|^2 = \frac{2\pi c^2}{\varepsilon_r\omega_\lambda^2}U_\lambda = \frac{2\pi\hbar c^2}{\varepsilon_r\omega_\lambda}N_\lambda$$

where ε_r is real part of dielectric function.

It is clear from this semiclassical result that absorption and emission rates vanish as N_λ approaches to zero (the spontaneous emission is not expected).

To include a spontaneous emission term a full quantum treatment is needful and the final result is:

$$|A_{0,\lambda}^{em}|^2 = \frac{2\pi\hbar c^2}{\varepsilon_r \omega_\lambda}(N_\lambda + 1)$$

Even if the field approaches to zero (N_λ= 0) the spontaneous emission is possible.

So expressions describing absorption and emission rate are:

$$W_{ab} = \left(\frac{2\pi}{\hbar}\right)\sum_\lambda \sum_{u,l} |H_{ul}^{ab}|^2 \, N_\lambda \delta(E_{ul} - \hbar\omega_\lambda)$$

and

$$W_{em} = -\left(\frac{2\pi}{\hbar}\right)\sum_\lambda \sum_{u,l} |H_{lu}^{em}|^2 \, (N_\lambda + 1) \, \delta(E_{ul} - \hbar\omega_\lambda)$$

where: $|H_{lu}^{em,ab}|^2 = \frac{2\pi\hbar}{m^2 \varepsilon_r \omega_\lambda} |P_{lu}^{em,ab}|^2$

We are interested in transition involving photons in a spectral range so it is useful to define the differential transition rate:

$$dW = \left(\frac{dW}{d\omega}\right) d\omega$$

obtained by summing over all modes satisfying the condition $\omega < \omega_\lambda < \omega + d\omega$.

Assuming that beam is contained in a solid angle $d\Omega_k$, if N_λ is the number of photons contained in λ mode we have for absorption rate:

$$dW_{ab} = \left(\frac{2\pi}{\hbar}\right)\sum_\lambda \sum_{u,l} \left|H_{ul}^{ab}\right|^2 \, N_\lambda \, \delta(E_{ul} - \hbar\omega_\lambda)$$

$$= \left(\frac{2\pi}{\hbar}\right)\sum_{u,l} \left|H_{ul}^{ab}\right|^2 N(\boldsymbol{k}, \hbar\omega) \, \delta(E_{ul} - \hbar\omega_\lambda) \, d\hbar\omega \, d\Omega_k$$

where $N(\boldsymbol{k},\hbar\omega)$ is number of photons per unit energy interval, per unit volume, per steradian.
In other words we can express the sum over the occupation number N_λ of the radiation modes λ contained within the frequency interval ω , $\omega + d\omega$ and within the solid angle $d\Omega_k$
in following way:

$$\sum_\lambda N_\lambda = N(\boldsymbol{k},\hbar\omega)\ d\hbar\omega\ d\Omega_k = \overline{N_\lambda}\mathrm{G}_\Omega(\hbar\omega)\ d\hbar\omega\ d\Omega_k$$

in the previous relation also the quantities $\overline{N_\lambda}$ and $G_\Omega(\hbar\omega)$ are defined, they are respectively the average number of photons per mode and the number of modes contained in $d\hbar\omega\ \mathrm{d}\Omega_k$
For emission rate:

$$dW_{st.em} = -\left(\frac{2\pi}{\hbar}\right)\sum_{u,l}|H_{lu}^{em}|^2\ N(\boldsymbol{k},\hbar\omega)\ \delta(E_{ul} - \hbar\omega_\lambda)\ d\hbar\omega\ d\Omega_k$$

Previous formulas are valid when all initial states are occupied and all final states are empty (T=0 K). When T > 0 we have to correct the results introducing the probability that a generic j state was occupied P_j or empty $P_j^{'}$.
Using these correction factors the expressions for the rates at which transitions occur are:

$R_{ab}(\hbar\omega)\ d\hbar\omega = \ dW_{ab}P_lP_u^{'}$ for absorption

$R_{st.em}(\hbar\omega)\ d\hbar\omega = \ -dW_{st.em}P_uP_l^{'}$ for stimulated emission

summing up previous equations we have:

$$R_{st}(\hbar\omega)\ d\hbar\omega = \left(\tfrac{2\pi}{\hbar}\right)\textstyle\sum_{u,l}|H_{ul}|^2\ [\,P_uP_l^{'} - P_lP_u^{'}]\ N(\boldsymbol{k},\hbar\omega)\delta(E_{ul} - \hbar\omega_\lambda)\ d\hbar\omega\ d\Omega_k$$

defining photon flux $\mathbf{F}(\boldsymbol{k},\hbar\omega)$ and spectral photon flux $\mathbf{F}(\hbar\omega)$ in following way:

$\mathbf{F}(\boldsymbol{k},\hbar\omega) = \boldsymbol{V}_{en}(\hbar\omega)\ \mathrm{N}(\boldsymbol{k},\hbar\omega)$ $\qquad \mathbf{F}(\hbar\omega) = \int \mathbf{F}(\boldsymbol{k},\hbar\omega)d\Omega_k$

where $\boldsymbol{V}_{en}(\hbar\omega)$ is the energy propagation velocity transported by e.m field.

Considering that absorption coefficient $\alpha(\hbar\omega)$ is the rate of decrease in $\boldsymbol{F}$ per unit distance in direction of propagation $\hat{\mathbf{x}}$ we have:

$$\alpha\ (\hbar\omega) = -\left(\frac{1}{\boldsymbol{F}}\right)\frac{d\boldsymbol{F}}{dx}$$

Using continuity equation it's possible to relate $\mathbf{F}(\hbar\omega)$ to spectral density $\mathrm{N}(\hbar\omega)$ (where $\mathrm{N}(\hbar\omega) = \int \mathrm{N}(\boldsymbol{k}, \hbar\omega) d\Omega_k$) :

$$div\ \boldsymbol{F}(\hbar\omega) + \frac{\partial N(\hbar\omega)}{\partial t} = 0$$

and in one dimension it becomes:

$$-\left(\frac{1}{\boldsymbol{F}(\hbar\omega)}\right)\frac{d\boldsymbol{F}(\hbar\omega)}{dx} = \left(\frac{1}{\boldsymbol{F}(\hbar\omega)}\right)\frac{\partial N(\hbar\omega)}{\partial t} = \left(\frac{1}{\boldsymbol{F}(\hbar\omega)}\right)[-R_{st}(\hbar\omega)]$$

so:

$$\alpha\ (\hbar\omega) = \frac{-R_{st}(\hbar\omega)d\hbar\omega}{\mathbf{F}(\boldsymbol{k}, \hbar\omega)d\Omega_k d\hbar\omega}$$

$$= \left(\frac{2\pi}{\hbar}\right)\sum_{u,l} V_{en}^{-1}\ |H_{ul}|^2\ [\,P_l P_u^{'} - P_u P_l^{'}]\ \delta(E_{ul} - \hbar\omega_\lambda)$$

Concerning spontaneous emission, it does not depend on incident beam, consequentially an excited system can emit a photon in any direction and any polarization state.
The spontaneous emission rate is:

$$R_{sp}(\hbar\omega)\ d\hbar\omega = -\ dW_{sp} P_u P_l^{'}$$

$$= \left(\frac{2\pi}{\hbar}\right)\sum_{\lambda;\omega_\lambda=\omega}^{\omega+d\omega}\sum_{u,l} |H_{ul}|^2 1_\lambda\ P_u P_l^{'}\ \delta(E_{ul} - \hbar\omega_\lambda)$$

$$= \left(\frac{2\pi}{\hbar}\right) \sum_{u,l} |H_{ul}|^2 \, G(\hbar\omega) \, P_u P_l' \delta(E_{ul} - \hbar\omega_\lambda) \, d\hbar\omega$$

where $G(\hbar\omega) = \int G_\Omega(\hbar\omega) d\Omega_k$
[40].

2.3 Summation over states

The sum in previous paragraph over u and l may be split in two parts, a sum over E_u , E_l and a sum over D_u , D_l, where E_u and E_l are the energy levels and D_u e D_l respectively refer to total number of states at energy E_u and E_l .

$$\sum_{u,\, l} \rightarrow \sum_{Eu,\ Eu} \sum_{Dl,\ Du}$$

We broke previous sum over the states because the probability that a state was occupied depends only on its energy and it doesn't depend on particular d_j component of the degenerate set of D_j states.
Defining an average interaction Hamiltonian:

$$\langle |H_{ul}|^2 \rangle_{av} = \frac{1}{D_u D_l} \sum_{d_u d_l}^{D_u, D_l} |H_{ul}|^2$$

the emission rate becomes:

$$R_{sp}(\hbar\omega) = \left(\frac{2\pi}{\hbar}\right) \sum_{E_l, E_u} \left[\frac{1}{D_u D_l} \sum_{d_u d_l}^{D_u, D_l} |H_{ul}|^2 \right] G(\hbar\omega) D_u P_u D_l P_l' \delta(E_{ul} - \hbar\omega) =$$

$$= \left(\frac{2\pi}{\hbar}\right) \sum_{E_l, E_u} < |H_{ul}|^2 >_{av} \, G(\hbar\omega) n(E_u) n'(E_l) \delta(E_{ul} - \hbar\omega)$$

In which n(E) represents density of states ρ times occupation probability and its definition is valid for both discrete (for example impurity states) and continuum states (bands).
For discrete states the density of states is proportional to delta function:

$$\rho(E_j^{'}) \rightarrow N_j \delta(E_j^{'} - E_j)$$

The rate $R_{sp}(\hbar\omega)$ has a different forms according to kind of transition (continuum → continuum, discrete → continuum, continuum → discrete, discrete → discrete)
In following paragraph only first and second kind of transitions are described because the measurements performed in this work concern only with these kind of transitions [40].

2.4 Discrete-continuum transitions

Considerer a donor-valence band recombination, using a parabolic approximation for valence band:

$$E_v(\boldsymbol{k}) = -\frac{(\hbar k)^2}{2m_v}$$

It's possible to demonstrate that:

$$R_{sp}(\hbar\omega) = \frac{2\pi}{\hbar} G(\hbar\omega) \langle |H_{ul}|^2 \rangle_{av} n_u \rho_l (E_u - \hbar\omega) P_l^{'}(E_u - \hbar\omega)$$

$R_{sp}(\hbar\omega)$ linearly depends on occupied intragap states concentration n_u, moreover the principal variation of $R_{sp}(\hbar\omega)$ (figure xxx) is due to $\rho(E_u - \hbar\omega)P_l^{'}(E_u - \hbar\omega)$ product, where ρ shows a square root dependence on $\hbar\omega$ and $P_l^{'}$ has an exponential dependence on $\hbar\omega$ [40].

2.5 Continuum-continuum transitions

In this case the transitions occur across the gap between conduction and valence band and there are selections rule that allow only particular transitions.
If the Bloch function $exp(\boldsymbol{k}_j \boldsymbol{r}) u_{j\boldsymbol{k}_j}(\boldsymbol{r})$ are assumed for both valence and conduction states, it is possible to show that the matrix element $\langle u|exp(\boldsymbol{k}_j \boldsymbol{r})|l\rangle$ doesn't vanish if following relation is true $\boldsymbol{k}_u = \boldsymbol{G} + \boldsymbol{k} + \boldsymbol{k}_l$ where $\boldsymbol{k}_u$ and $\boldsymbol{k}_l$ are the momentum vector of the upper and lower states, $\boldsymbol{k}$ is the wave vector of radiation and $\boldsymbol{G}$ is a vector of reciprocal lattice.

In optical frequency interval, **k** vector may be neglected and the only solution is:

$\boldsymbol{G = 0 \ \rightarrow \ k_u = k_l}$

so:

$$\langle |H_{ul}|^2 \rangle_{av} = \langle |H_{ul}|^2 \rangle_{av} \, \delta_{k_u k_l}$$

.

Defining:

$$\rho_{red} = \frac{1}{2\pi^2} \frac{k^2}{\left[\left(\frac{d}{dk} \right) \left(E_u(k_u) - E_l(k_l) \right) \right]_{E_u = E_l + \hbar\omega}}$$

Using a parabolic approximation for the bands we have:

$$\rho_{red} = \frac{1}{(2\pi)^2} \left(\frac{2\mu}{\hbar^2} \right)^{3/2} \left(\hbar\omega - \varepsilon_g \right)^{1/2}$$

(μ is reduced mass between effective masses of valence and conduction band)

It's possible to demonstrate that the spontaneous emission rate is approximated by following expression:

$$R_{sp}(\hbar\omega) \sim \left(\hbar\omega - \varepsilon_g \right)^{1/2} exp\left(-\frac{\hbar\omega}{kT} \right)$$

[40, 41] .

2.6 Relation between absorption and emission

The spontaneous emission rate when there is only one upper level and only one lower level is:

$$R_{sp}(\hbar\omega) = \frac{2\pi}{\hbar} \langle |H_{ul}|^2 \rangle_{av} G(\hbar\omega) n_u n_l' \delta(E_{ul} - \hbar\omega)$$

in same condition the absorption coefficient is given by:

$$\alpha(\hbar\omega) = \frac{2\pi}{\hbar}\frac{1}{V_{en}}\langle|H_{ul}|^2\rangle_{av}\left(n_l n_u^{'} - n_u n_l^{'}\right)\delta(E_{ul} - \hbar\omega)$$

So the relation between R_{sp} and α is:

$$R_{sp}(\hbar\omega) = V_{en}G(\hbar\omega)\alpha(\hbar\omega)\frac{n_u n_l^{'}}{\left(n_l n_u^{'} - n_u n_l^{'}\right)}$$

In all the quantities calculated until now we have used the Fermi-Dirac distribution to describe the occupation probability of electrons and holes but this distribution describes the system only in equilibrium condition.

When the system is illuminated, it is made out equilibrium and it is needful another function to describe the occupation probability of the system by means of introduction of quasi Fermi levels.

After illumination there is a transient period, during this period the electrons and holes relax through phonon collisions ($\sim 10^2\ fs$) and electron-electron collisions, after this time the electrons in conduction band and holes in valence band are well described by two Fermi functions with different Fermi energy called quasi Fermi level for electron F_n and for holes F_p with

$F_n > E_F$ and $F_p < E_F$ where E_F is the equilibrium Fermi level.

When the system returns to equilibrium $F_n \to E_F$ and $F_p \to E_F$.

So, out of equilibrium, the number of occupied states in conduction band is:

$$n_u = \rho(E_c)f(E_c)$$

the number of empty states in conduction band is:

$$n_u^{'} = \rho(E_c)[1 - f(E_c)]$$

where f is the quasi Fermi function of conduction band

$$f(E_c) = \frac{1}{1 + exp\left(\frac{E_c - F_n}{kT}\right)}$$

The number of empty states in valence band (occupied with holes) is

$$n_l^{'} = \rho(E_v)f'(E_v)$$

The number of occupied states in valence band is:

$$n_l^{'} = \rho(E_v)[1 - f'(E_v)]$$

where: $f'(E_v) = \frac{1}{1+exp\left(\frac{Fp-E_v}{kT}\right)}$

So the ratio between occupation numbers in recombination rate expression becomes:

$$\frac{n_u n_l^{'}}{\left(n_l n_u^{'} - n_u n_l^{'}\right)} = \frac{f(E_c)[1 - f(E_v)]}{f(E_v) - f(E_c)} = \frac{1}{exp\left(\frac{\hbar\omega - \Delta F}{kT}\right) - 1}$$

Where: $\hbar\omega = E_c - E_v$ and $\Delta F = F_n - F_p$ which gives a measurement of excitation degree of the system.

If $\hbar\omega \gg \Delta F$ the relation between R_{sp} and α becomes:

$$R_{sp}(\hbar\omega) = \frac{exp\left(\frac{\Delta F}{kT}\right)}{(\pi c)^2\hbar^3} n^2 \alpha(\hbar\omega)(\hbar\omega)^2 exp\left(-\frac{\hbar\omega}{kT}\right)$$

in which we assumed V_{en} velocity equal to group velocity.

This relation is very useful to analyze material for which adequate theory is not available. [40].

2.7 Total emission rate

The rate expression $R_{st}(\hbar\omega)$, as seen in paragraph 2.2, is:

$$R_{st}(\hbar\omega)\, d\hbar\omega = -\alpha\,(\hbar\omega)F(\hbar\omega)\mathrm{d}\,\hbar\omega$$

$$\left(\frac{2\pi}{\hbar}\right)\sum_{E_u E_l} < \left| H_{ul} \right|^2 >_{av} G(\hbar\omega)\bar{N}(n_u n_l^{'} - n_l n_u^{'})\delta(E_{ul} - \hbar\omega_\lambda)$$

where $\bar{N}$ is the average number of photons per radiation mode.

The total recombination rate R_T is the sum of the stimulated emission rate R_{st} and spontaneous emission rate R_{sp}:

$$R_T(\hbar\omega)d\hbar\omega = \left[R_{sp}(\hbar\omega) + R_{st}(\hbar\omega)\right] d\hbar\omega$$

$$= \left(\frac{2\pi}{\hbar}\right) \sum_{E_u E_l} < \left| H_{ul} \right|^2 >_{av} G(\hbar\omega)\delta(E_{ul} - \hbar\omega_\lambda)[n_u n_l' + \bar{N}(n_u n_l' - n_l n_u')]\, d\hbar\omega$$

$$= R_{sp}(\hbar\omega)[1 + \bar{N}\frac{(n_u n_l' - n_l n_u')}{n_u n_l'}]d\hbar\omega$$

So total emission rate is given by:

$$R_T(\hbar\omega) = R_{sp}(\hbar\omega)\{1 - \bar{N}\,[\exp\left(\frac{\hbar\omega - \Delta F}{kT}\right) - 1]\}$$

In thermal equilibrium, the average number of photons per mode is given by Bose-Einstein distribution and the difference between quasi Fermi level is zero $\Delta F = 0$ so the total rate $R_T(\hbar\omega)$ vanishes in agreement with detailed balance principle.

In photoluminescence experiment the excess density of pairs is optically generated so the total emission rate becomes non zero due two reason:

1) ΔF becomes non-zero therefore the occupational number of pairs changes
2) The photon occupation number per mode is changed

Could happen that spontaneous emission photons are re-adsorbed by material generating other pairs, if this phenomenon is not negligible, the non-radiative recombinations increase and the reason is the increasing of radiative recombination time compared to non-radiative time.

In previous discussion we have assumed that the sample deviates slightly from thermal equilibrium.

ΔF increases when the excitation increases and re-absorption phenomena decrease.

$R_{st}(\hbar\omega)$ becomes positive when $\bar{N}\,[\exp\left(\frac{\hbar\omega - \Delta F}{kT}\right) - 1]$ becomes negative ($\Delta F > \hbar\omega$)

So when this condition occurs, excess radiation provokes almost as many downward as upwards transitions that is the threshold for laser action.

The recombination dynamic of excited pairs depends on many material parameters, for sake of simplicity we neglect the absorption and stimulated emission so considering only spontaneous emission lifetime that is the main process analyzed in measurements of this work .

The electron-hole pairs radiative lifetime is ruled by spontaneous recombination rate $R_{sp}(\hbar\omega)$.

Performing the integral of $R_{sp}(\hbar\omega)$ on frequency domain we obtain the number of pairs per unit volume that recombine per unit time:

$$R_{sp} = \int_0^{\infty} R_{sp}(\hbar\omega)\ d\hbar\omega$$

If n is the number of occupied high energy states n_u and p is the empty low energy states n_l' we have:

$$R_{sp} = \left(\frac{R_{sp}^0}{n_0 p_0}\right) np$$

Where R_{sp}^0 represents the value that R_{sp} assumes at thermal equilibrium.

So the equation describing the behavior of electrons and holes number is:

$$-\frac{dn}{dt} = -\frac{dp}{dt} = Bnp = R_{sp}^0 \left(\frac{np}{n_0 p_0}\right)$$

This equation hides a problem, in fact the numeric value of time derivative is non zero at equilibrium ($n \to n_0 \quad e \quad p \to p_0$).

This problem is a consequence of neglecting absorption and stimulated emission.

To avoid this problem we integrate the total recombination rate $R_T(\hbar\omega)$.

$$-\frac{dn}{dt} = -\frac{dp}{dt} = \int_0^{\infty} R_T\,(\hbar\omega) d\hbar\omega = -B\left[n_u n_l'(\bar{N}+1) - n_l n_u'(\bar{N})\right]$$
$$= -(R_{em} - G_R)$$

Where R_{em} contains both stimulated and spontaneous emission term and G_R represents the absorption.

At thermal equilibrium $R_{em}^0 = G_R^0$ and we can define the radiative lifetime in following way:

$$\frac{1}{\tau_R} \equiv -\frac{1}{(\Delta n)}\frac{d(\Delta n)}{dt} = \frac{(R_{em} - G_R)}{(\Delta n)}$$

Where Δn and Δp are the displacements of n and p from equilibrium values.

$$\Delta \mathrm{n}(\mathrm{x}, \mathrm{t}) = \mathrm{n}(\mathrm{x}, \mathrm{t},) - \mathrm{n}_0$$

$$\Delta \mathrm{p}(\mathrm{x}, \mathrm{t}) = \mathrm{p}(\mathrm{x}, \mathrm{t},) - \mathrm{p}_0$$

so Δn and Δp represent the injection of carriers due to excitation.
If the external radiation generates a number of pairs that excited occupied states is smaller than number of non-excited occupied states, the absorption coefficient doesn't change because of excitation so G_R is equal to its equilibrium value

$$G_R = G_R^0 = R_{em}^0$$

so we have:

$$\frac{dn}{dt} = -(R_{em} - G_R^0) = -(R_{em} - R_{em}^0)$$

$$= -\left[R_{em}^0\left(\frac{np}{n_0 p_0}\right) - R_{em}^0\right]$$

$$= R_{em}^0\left(\frac{np - n_0 p_0}{n_0 p_0}\right)$$

Using the law of mass action $np = n_i^2(T)$ valid only for a non-degenerate semiconductor we have:

$$\frac{dp}{dt} = \frac{dn}{dt} = -R(n,p) = r(n,p)[np - n_i^2]$$

Where in some case, as seen before, $\mathrm{r}(\mathrm{n}, \mathrm{p})$ doesn't depend on n and p (in this case for clarity we define B as $r(n,p) = B = const$).

In a doped semiconductor the concentrations of carriers are:

$n_0 = N_D \qquad p_0 = \frac{n_i^2}{N_D}$ for an n-type semiconductor

$p_0 = N_A \qquad n_0 = \frac{n_i^2}{N_A}$ for an p-type semiconductor

Where N_D and N_A are the density of donors and acceptors.

For a n-type semiconductor (ZnO is naturally n-doped) the equation describing the concentration of minority carriers (holes) is:

$$\frac{dp}{dt} = \frac{d\Delta p}{dt} = -B[(N_D + \Delta n)(p_0 + \Delta p) - n_i^2]$$

Using $N_D p = n_i^2$ we have:

$$\frac{d\Delta p}{dt} = -B[N_D \Delta p + \Delta p^2]$$

In low injection limit the equation becomes:

$$\frac{d\Delta p}{dt} = -BN_D \Delta p$$

whose solution is:

$\Delta p(t) = \Delta p_0 exp\left(-\frac{t}{\tau_R}\right)$ where: $\frac{1}{\tau_R} = BN_D$

In low injection limit, the lifetime doesn't depend on time.

For a general injection level the solution of rate equation is :

$$\Delta p(t) = \frac{\Delta p_0 exp\left(-\frac{t}{\tau_R}\right)}{1+\frac{\Delta p_0}{N_D}\left(1-exp\left(-\frac{t}{\tau_R}\right)\right)}$$

In high injection limit and when $t << \tau_R$, the behavior of $\Delta p(t)$ is:

$\Delta p(t) = \frac{\Delta p_0}{1+BN_D t}$ when $\Delta p_0 >> N_D$ and $t << \tau_R$,

$\Delta p(t)$ approaches again to a simple exponential function when t >> τ_R .

All previous considerations regard a semiconductor with unitary quantum efficiency (η=1)

The PL intensity is given by:

$$I_{PL}(t) = K\left\{rN_D\frac{\Delta p_0 exp\left(-\frac{t}{\tau}\right)}{1+\frac{\Delta p_0}{N_D}\left(1-exp\left(-\frac{t}{\tau}\right)\right)} + r\left[\frac{\Delta p_0 exp\left(-\frac{t}{\tau}\right)}{1+\frac{\Delta p_0}{N_D}\left(1-exp\left(-\frac{t}{\tau}\right)\right)}\right]^2\right\} \qquad (2.1)$$

This formula means that the luminescence decays very quickly when the density of excited pairs is large in comparison with N_D at early stage of decay (figure 2.1).

When the time go on, the luminescence's decrement slows and approaches to a single exponential as in low injection limit.

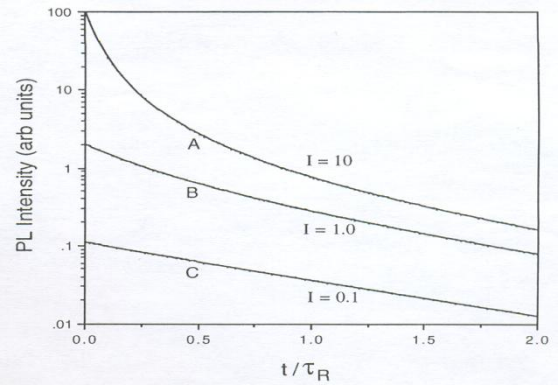

Figure 2.1. *The picture shows three decays at different injection level as function of ration between time and lifetime.*

The measure of $I_{PL}(t)$ give us information on physical parameters involved in recombination, but this measure and the relative fitting procedure is not trivial because time scale when the intensity shows a perceptible variation, especially at early stage of decay, is of order of $10^{-10}sec$ and the function is a very sophisticated function with many parameters so performing the fit in a standard way could cause unreliability on the estimated parameters. For this reason usually the decay is separated in several parts (depending on p_0 and t) and the fit is performed using approximation of generic injection function.

Another method used to obtain physical parameters by time resolved measurement is explained in the following paragraph [40, 42].

2.8 Instantaneous lifetime $\tau_{eff}(t)$

The characteristic time of $I_{PL}(t)$ is not a constant but it's possible to define an instantaneous effective time (τ_{eff}) in this way:

$$\frac{1}{\tau_{eff}(t)} \equiv -\frac{\frac{dI_{PL}(t)}{dt}}{I_{PL}(t)} = \frac{BN + 2B\rho}{BN\rho + B\rho^2}\frac{d\rho}{dt}(t) = \frac{N + 2\rho}{N\rho + \rho^2}\frac{d\rho}{dt}(t)$$

where a symmetric notation has been adopted $\Delta n = \Delta p = \rho$

If previous quantity is calculated at the onset of the decay (t=0) and the η is equal to one we have:

$$\frac{1}{\tau_{eff}}(0) = B\,[N + 2\rho(0)] \qquad (2.2)$$

If several decays are acquired for different value of $\rho(0)$ and $\frac{1}{\tau_{eff}}(0)$ is calculated using the definition, it's possible to fit this measured $\frac{1}{\tau_{eff}}(0)$ value using function in (2.2) obtaining the values of B and N. If the excitation is carried out by a pulsed laser with time duration negligible in comparison with time constant involved in the process, the density of excited pairs $\rho(0)$ is related to laser energy in following way:

$$\rho(0) = \frac{E\,\alpha\,(1 - R)}{h\nu\,S}$$

where E is the energy of laser pulse, α is the absorption coefficient of material at laser wavelength, R is the sample reflectivity and S is the laser spot area.

The formula assumes that entire radiation is adsorbed in a depth equal to the penetration length in homogeneous way.

Unfortunately to find a system with unitary quantum efficiency is very difficult for a wide excited carrier density range so it's needful to generalize the previous method.

All previous consideration are valid only for band to band recombination in an n-doped semiconductor [42].

2.9 Non-radiative recombination processes

The recombination described in previous paragraph regards a radiative band to band recombination but, in an excited semiconductor, the excited electron-holes pairs can decay in several way. The non-radiative intergap relaxations take place by means of phonons while non-radiative intragap transitions are also possible. From a theoretical point of view, an intragap transition is possible also by means of phonons only but such process is very unlikely at room temperature in a widegap semiconductor as it should take place as a multiphonons process. Other kinds of nonradiative transitions are due to Auger effect and defects-assisted transitions that are exposed next.

Auger process

Auger process is an electron-hole pair recombination in which the e-h pair energy is transferred to a third free carrier that will move to higher energy value of conduction band (if it is an electron) or to lower energy value of valence band (if it is an hole). In Auger process a pair recombines without photon emission reducing quantum efficiency, this process is a three-bodies process because an electron and two holes or an hole and two electrons are needful. For this reason only in very high injection regime the Auger recombination affects quantum efficiency. The inverse of Auger effect is called impact ionization, in this process an high energy free carrier transfers its kinetic energy to an electron in valence band with following creation of e-h pair. This effect becomes considerable if the energy of the exciting photon is much higher than bandgap.

Shockley-Read-Hall process and lifetime

These recombinations take place because of trapping carriers by defect levels which energies lying in the forbidden gap of semiconductor. The description of this kind of processes is very difficult because a system of two equations is needful (one for electron and one for hole density); in fact, for a generic deep level concentration, the photogenerated electrons and holes density are different each other. When the concentration of deep levels is low only an equation is sufficient to describe the system.

The recombination of e-h pairs at defect levels in this condition was studied for the first time by Shockley Read and Hall in 1952.

The rate of SRH recombination is:

$$R_{SHR} = \frac{\sigma_p \sigma_n v_{th} N_t [pn - n_i^2]}{\sigma_n \left[n + n_i exp\left(\frac{E_t - E_i}{kT}\right)\right] + \sigma_p \left[p + n_i exp\left(\frac{E_i - E_t}{kT}\right)\right]}$$

Here, N_t is the volume density of intragap levels, σ_p and σ_n are the holes and electrons capture cross-section respectively, E_t is the intragap level energy and $E_i = \frac{E_{gap}}{2}$.

If ρ is the injected e-h pairs density we have in a n-type material:

$$R_{SHR} = \frac{\sigma_p \sigma_n v_{th} N_t [\rho N_D + \rho^2]}{\sigma_n \left[n + n_i exp\left(\frac{E_t - E_i}{kT}\right)\right] + \sigma_p \left[p + n_i exp\left(\frac{E_i - E_t}{kT}\right)\right]}$$

When the defect level lies near midgap, the R_{SHR} rate shows a maximum and the level is a recombination center, when the E_i energy lies near the valence band or conduction band one of the terms in the denominator becomes very large, the R_{SHR} rate becomes very small and the defect is a hole or electron trap respectively because of electron trapping (in case of $E_t \cong E_c$ for example) decreases the number of electron in CB thus the band to band recombination is decreased and the SRH recombination is a very improbable process because of E_t is too high in comparison with E_v.

Defining: $\tau_n = \frac{1}{\sigma_n N_t v_{th}}$, $\tau_p = \frac{1}{\sigma_p N_t v_{th}}$

and considering that $N_D \gg n_i$ the rate for near-midgap states becomes:

$$R_{SRH} = \frac{[\rho N_D + \rho^2]}{\tau_p [N_D + \rho] + \tau_n \rho}$$

Using symmetric notation valid for n and p-type semiconductors:

$$R_{SRH} = \frac{[\rho N + \rho^2]}{\tau_{min} [N + \rho] + \tau_{maj} \rho}$$

where N is the dopant concentration and τ_{min}, τ_{maj} are the minority and majority carriers lifetime respectively. In low injection limit we have:

$$-\frac{d\rho}{dt} = R_{SRH} = \frac{\rho}{\tau_{min}}$$

In low injection limit the recombination is controlled by the minority carrier capture cross section. In this condition $\rho \ll N$ so after the capture of a minority carrier the center is reset by the instantaneous capture of a majority carrier because of the high concentration of majority carrier [42].

2.10 Exciton

The band structure of a semiconductor describes the so-called $N \pm 1$ particles problem because it considers completely full valence band containing N electrons and completely empty conduction band. The only way to put an electron in conduction band is to take it from valence band. When the electron moves to CB and leaves an hole in VB (for example by photon absorption) the interaction and so the band structure should change so the second excited electron should experiences another band structure and so on.

When a photon is adsorbed, a system of N electrons is brought to an excited state.

What we need to understand optical properties of the electronic system in a semiconductor is therefore a description of the excited states of the N particle problem. The quanta of this excitation are called excitons.

The state in which valence band is full and conduction band is empty is the zero energy state.

Another point of view is the following. If an electron is excited to conduction band, simultaneously an hole in VB is created so an optical excitation is a two-particle transition. The same is true for recombination process.

It's possible to describe the exciton at several level of approximation. If the exciton is seen as an electron-hole bound system when the Bohr radius is much larger then unit cell dimension (so dielectric constant is small) it's possible to describe the exciton in effective mass approximation (Wannier exciton).

In ZnO the Bohr radius is about 2nm [1] and is larger than maximum unit cell dimension that is about 0.5nm, so the Wannier exciton description is adopted in the following.

Using the effective mass approximation the problem is hydrogen-like provided to substitute the dielectric constant of material in Coulomb potential expression. Separating the relative motion of electron and hole and the motion of the center of mass, the dispersion relation is:

$$E_{ex}(n_{B,}\boldsymbol{K}) = E_g - R_y^* \frac{1}{n_B^2} + \frac{\hbar \boldsymbol{K}^2}{2M} \qquad (2.3)$$

where $n_{B,}$ is the principal quantum number, R_y^* is the exciton binding energy,

$M = m_e + m_h$ is the translational mass of exciton and $\boldsymbol{K} = \boldsymbol{k}_e + \boldsymbol{k}_h$ is the exciton wave vector.

Using the formula (2.3) we can see that transitions are possible also when the involved energies in the process are lower than band gap.

When point defects are in crystal some of this defects can bind an exciton resulting in a bound exciton complexes (BEC). It's possible to have exciton bound to ionized donor D^+X , neutral donor D^0X and neutral acceptor A^0X . It's very difficult to find an exciton bound to ionized acceptor because a neutral acceptor and a free electron are energetically more favorable.
The excite-complex binding energy usually increases in following way:

$$E^b_{D^+X} < E^b_{D^0X} < E^b_{A^0X}$$

So in the emission spectrum the most energetic emission, after free exciton emission, is due to $E^b_{D^+X}$ emission [34].

2.11 High injection effects in semiconductor

The phenomena above described regard semiconductor which electron-hole density is not too large and it's possible to have an electron more or less bound to a correspondent hole to produce an exciton. When the electron-hole pairs density is large the exciton disappears and the free carriers in the semiconductor can be described as a plasma, the large number of free carriers leads to many body effects like bandgap renormalization.
Consider an exciton in the semiconductor, when the density of pairs ρ increases, the screening effects appear and exciton binding energy decreases so the exciton state approaches to conduction band edge resulting in a blue shift of exciton (this effect is weak in wide bandgap semiconductor like ZnO).
Due to screening effects, the Coulomb potential transforms in to a Yukawa potential given by:

$$\frac{1}{4\pi\varepsilon_0\varepsilon}\frac{e^2}{|\boldsymbol{r}_e-\boldsymbol{r}_h|} \rightarrow \frac{1}{4\pi\varepsilon_0\varepsilon(\rho)} exp\left\{-\frac{|\boldsymbol{r}_e-\boldsymbol{r}_h|}{l(\rho)}\right\}\cdot\frac{1}{|\boldsymbol{r}_e-\boldsymbol{r}_h|}$$

The dielectric constant and the l quantity depends on density ρ.
If l falls below l_c , the Yukawa potential no longer has bound states, l_c is a constant depending on exciton Bohr radius a_b in following way:

$$a_b l_c^{-1} = 1.19$$

It's possible to demonstrate that the density of pairs at which electron-hole plasma starts to exist is:

$$\rho_M = 1.19^2 \frac{k_B T}{2 a_B^3 R_y^*}$$

This density is called Mott density and it describe the transition from an insulating gas of exciton to a metal-like state of electron-hole pairs.

When density increases the gap dimension decreases due exchange effect. In fact if electrons and holes were randomly distributed the Coulomb attraction and repulsion energies would cancel exactly and gap size would be independent on density.

But due the Pauli principle the particles are not randomly distributed because for example two electron with same spin couldn't occupy the same unit cell.

The average distance among the electrons increases so the Coulomb energy decreases and the bandgap size gets lower.

The exciton emission experiences two competitive effects when ρ increases: 1) a blue shift due to decreasing of exciton binding energy 2) a red shift due to bandgap renormalization.

Moreover the screening effects enhance the exciton Bohr radius resulting in an oscillator strength dumping.

Another many body effect is the Moss-Burstein effect, it results from the Pauli Exclusion Principle and it appears in semiconductors as a blue shift of the band-gap when doping increases (or density of excited pairs increases).

When the material is excited and the e-h pair density increases, the unoccupied states in conduction band become full and an opposite situation happens for hole in valence band. The energy distance between the lower empty state in CB and higher occupied states in VB became larger and the needful energy to a photon to be adsorbed increases. The final result is that the absorption spectrum changes but emission spectrum doesn't [34].

Chapter 3

Experimental Set-up

The experimental set-up employed for TRPL measurements is schematically shown in figure 3.1. The optical excitation was provided by the third harmonic (355 nm wavelength) of a mode-locked Nd:YAG laser, while time-resolved detection of the photoluminescence emission was provided by a streak camera coupled to a spectrometer. After blocking the fundamental (1064 nm wavelength) beam by an absorptive filter (F1), the third harmonic beam was separated from the second harmonic beam through a dichroic mirror (M3) and focused on the samples placed inside a test chamber. The PL signal emitted by the excited sample was collected by a large-area mirror (not shown in the figure) and focused, through converging lenses (L2, L3), on the input slit of a spectrometer that dispersed the different monochromatic components of light and sent them on input slit of the streak camera. An high pass optical filters (F2) (360nm cut-off wavelength) attenuated the elastic scattering of pump. A silicon photodiode (PD) was used to detect the small transmitted fraction of the 355 nm beam in order to monitor the laser pulse energy impinging on the sample. The time and wavelength-resolved images were stored in a personal computer.

Typical laser pulse energies E (fluences F) employed for measurements ranged from E = 10 μJ (Fluence = 10 μJ cm^{-2}) to about E = 2000 μJ (Fluence = 1.5×10^4 μJ cm^{-2}) with a pulse duration of 25ps FWHM. All TRPL data were collected at room temperature.

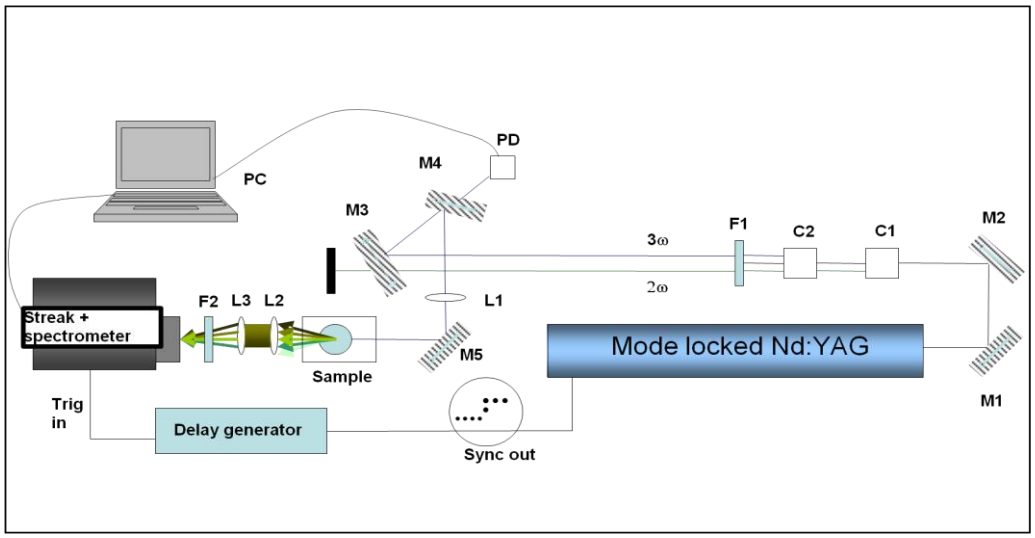

Figure 3.1 *TRPL experimental setup*

3.1 Nd:YAG laser

For time resolved PL analysis the laser used is an EKSPLA PL2143 which is a mode locked Nd:YAG laser producing 10 pulses/second of about 25ps time duration at 1064 nm wavelength. The laser is composed by a master oscillator producing a train of pulses (about 5μJ energy) using a Nd YAG rod as active medium, a regenerative amplifier where the pulse is amplified to 500μJ and a power amplifier which amplifies the pulses up to 30 mJ by means of a double pass through another Nd YAG rod.
A detailed description of laser system is showed in appendix A.

3.2 Streak

The acquisition setup of time resolved measurements is composed by a streak camera, a CCD and a spectrometer which exit slit is coupled with entrance slit of the streak. The acquisition setup (figure 3.2), entirely computer controlled, is used to perform optical measurements synchronously time-resolved and wavelength-resolved.

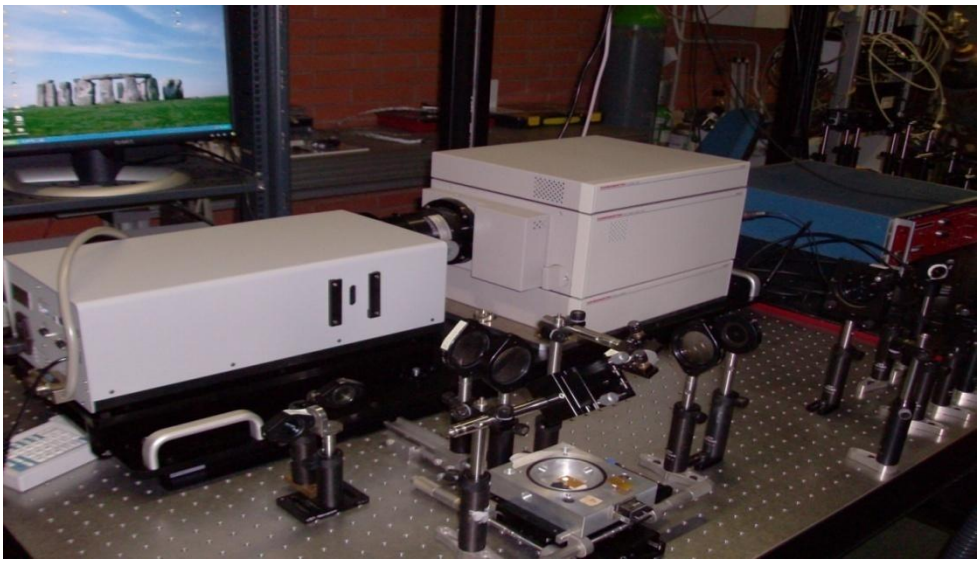

Figure 3.2. *The picture shows the spectrometer and streak camera of acquisition setup*

The streak camera is used to study time-dependent optical phenomena and it is composed (figure 3.4) by: A) photocathode, B) accelerating mesh, C) slit, D) sweep electrode, E) Microchannel plate (MCP), F) phosphor screen.

The used streak camera is a C5680 model of Hamamatsu, with this model it is possible to detect light with wavelength between 200nm and 850nm, the quantum efficiency and photocathode radiant sensitivity are shown in figure 3.3a.

The incident light impinges on the photocatode that via photoelectric effect emits electrons that are accelerated by means of electric field generated by mesh B. The accelerated electrons cross the silt C and cross a uniform vertical electric field region. The electric field is generated by a sawtooth voltage between electrodes D. So the vertical electron's deflection is proportional to $t-t_0$ where t is the instant when the generic electron goes in sweep-electrode region and t_0 is the instant when sawtooth starts so that the time distribution of incident photons is transformed in a spatial distribution (on vertical axis) like in oscilloscope. Then the electrons hit the microchannel plate that enhances the number of electrons until 1000 times the incident electrons apiece the MCP gain outwardly selected. The MCP gain (figure 3.3b) can be adjusted in 64 steps, ranging from 0 to 63. If the MCP gain is set to 0, a voltage of 400 V is applied. And when the setting is 63 the applied voltage is 900 V. Between 0 and 63 the voltage is applied in linear step.

a

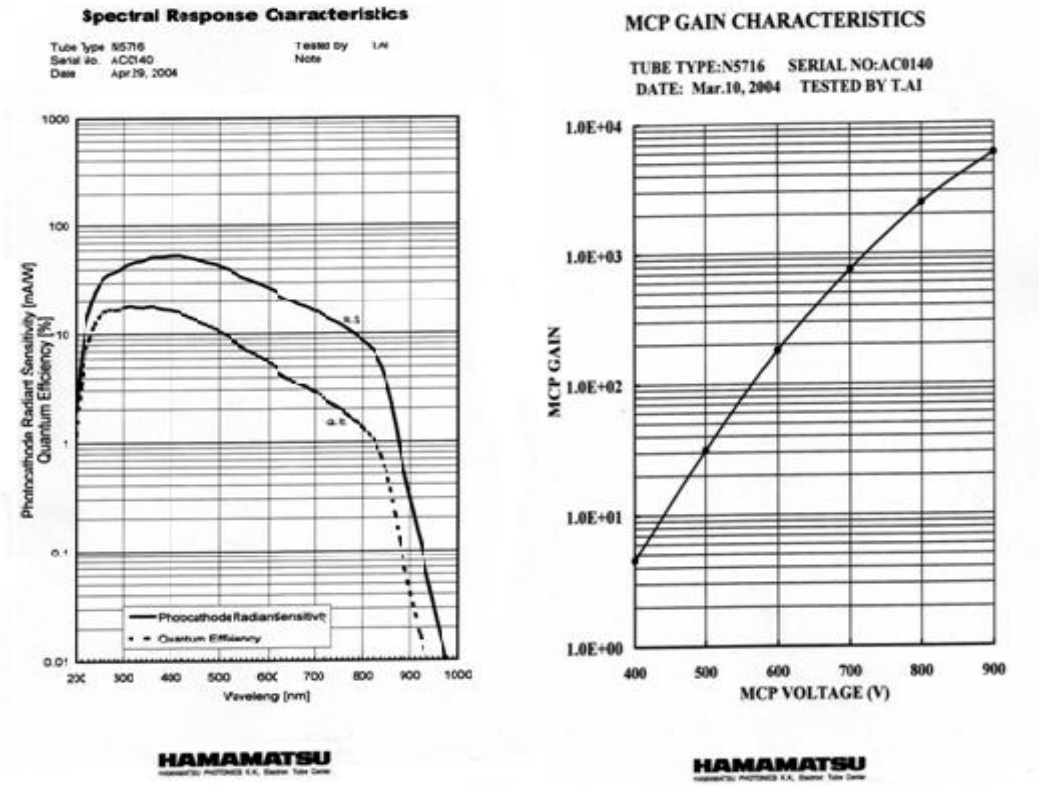

Figure 3.3. (a, b)

Increasing the MCP voltage, the number of photo-generated electrons increases and the broadening of travelling electrons, due to Coulomb repulsion, increases then the time and spectral resolution decreases.

The benefit of MCP gain increasing is that the signal to noise ratio increases because the MCP gain doesn't affect the dark current of CCD.

When the electrons hit the phosphor screen the resulting image is collected by a CCD camera 1064×1280 pixels.

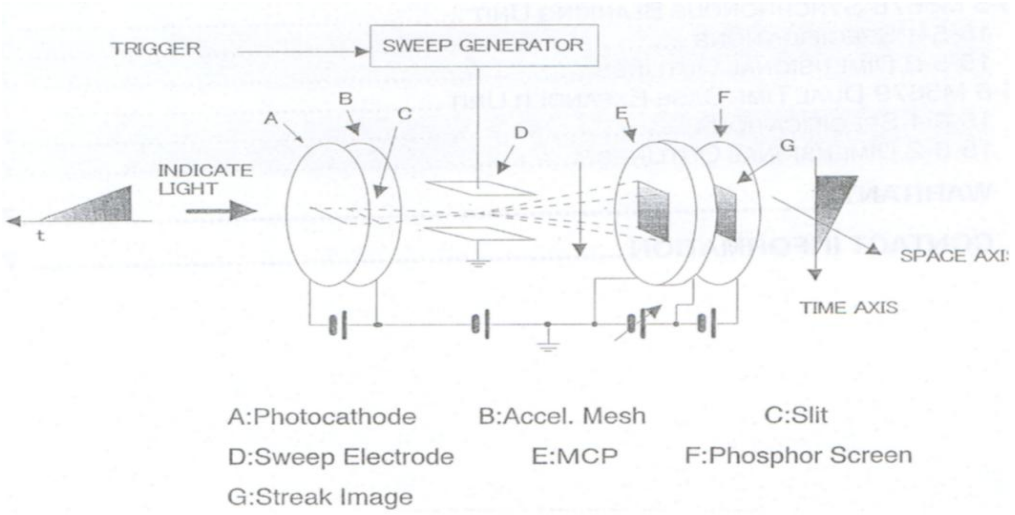

Figure 3.4. *The figure shows the streak scheme*

A given intensity of sweep's potential correspond to a particular time-range, the possible time-range are: 0.2 ns, 0.5 ns, 1 ns, 2 ns, 5 ns ,10 ns, 20 ns and 50 ns.

The time resolution (FWHM of impulse response function) doesn't depend so much on light wavelength, it is about 5 pixels that are ~ 2 ps using the shortest time-range (200 ps).

The characteristic time of analyzed phenomena are of order of ns or less, it's important that the starting of: sawtooth potential, the voltage of accelerating mesh, the voltage of MCP, exposure of CCD camera and the arrival of optical signal are well synchronized.

A detailed description of streak trigger and acquisition modes of CCD are showed in Appendix B.

Setup characterization

In order to estimate the resolution of apparatus and to compare the data acquired for different MCP gain conditions, some streak camera characterizations were performed, acquiring a single pulse at different time range and different gain condition.

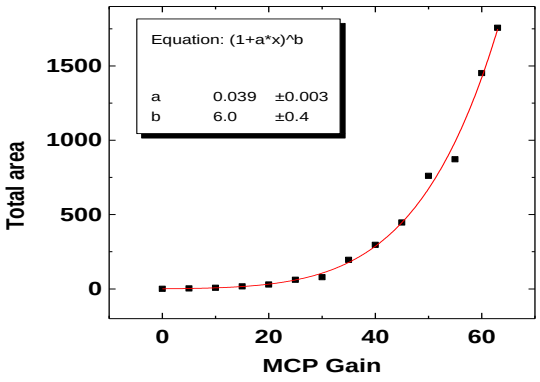

Figure 3.5. *Collected intensity of a single pulse as function of MCP gain.*

To perform the gain correction, a gain calibration curve was acquired. Several decays were collected varying gain condition, the total area under decay as function of MCP gain is shown in figure 3.5.

The points were fitted using the function:

$$\frac{A}{A_0} = (1 + a * g)^b$$

where A is the area, g is the gain, A_0 is the area when g = 0 and a, b are fitting parameters. This calibration curve was used to correct the data acquired varying gain.

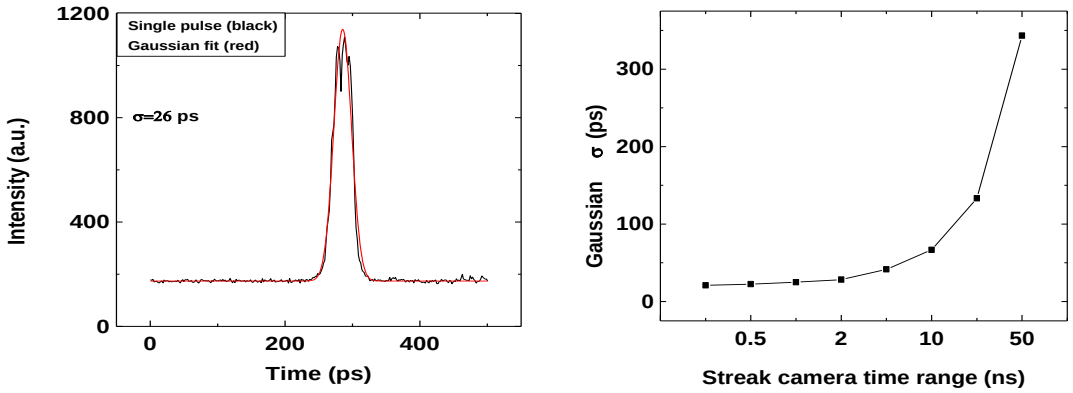

Figure 3.6. *Picture a) shows a laser pulse acquired using 500ps range and relative Gaussian fit. Picture b) shows the estimated width of Gaussian function as function of the used range for acquisition.*

The time resolution of apparatus depends on time range used; to test the resolution a single pulse was acquired and the time profile was fitted using a Gaussian function, the same measure was performed for all time range. In figure 3.6a the pulse acquired using 500ps time range and relative fit are showed. While in figure 3.6b the estimated standard deviation of Gaussian function is represented as function of time range used. The time resolution of apparatus is negligible in comparison with measured time phenomena for time range smaller than 5 ns.

3.3 Spectrometer

The input slit of streak camera is coupled with exit slit of a spectrometer that has three different gratings.
The spectrometer disperses light in wavelength and all monochromatic components hit synchronously the photocatode of streak camera. All processes described in streak's paragraph occur for all monochromatic components separately and synchronously, in this way it's possible to resolve the incident radiation in wavelength and time through a single measurement that produces a bidimensional image where the horizontal axis represents the wavelength, the vertical axis represents the time and the color of image represents the intensity of light as shown in figure 3.7.

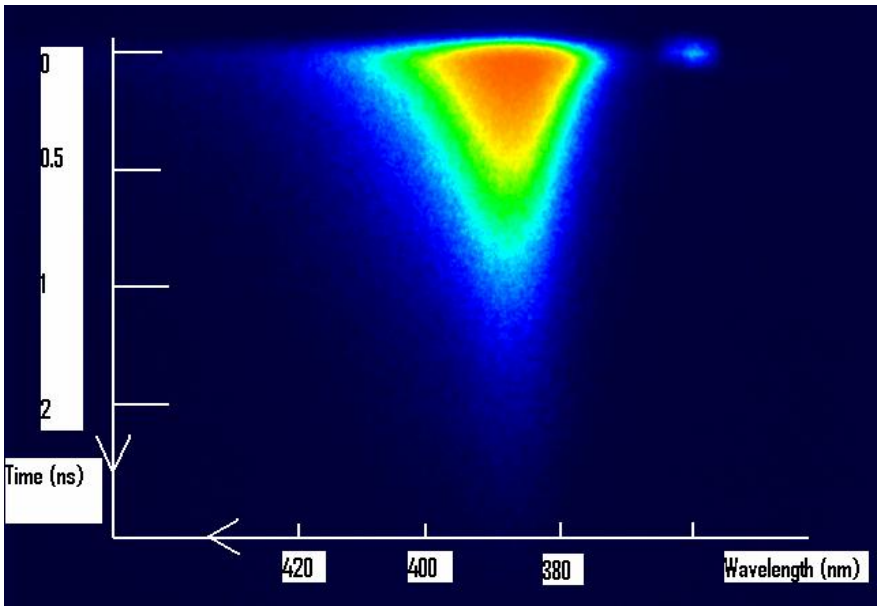

Figure 3.7. *The picture shows a typical false color CCD image where the horizontal axis represents wavelength, the vertical axis the time and the image color represents the intensity of light.*

Three gratings in the spectrometer are:

1) a grating blazed at 300 nm, 300 groves/mm
2) a grating blazed at 500 nm, 150 groves/mm
3) a grating blazed at 500 nm, 600 groves/mm

Through computer is possible to select the particular grating and to move the grating focalizing the selected wavelength on central pixel of CCD. The analyzed wavelength window has a width of 60 nm with a dispersion of 0.047 nm/ch for the first grating, a width of 120 nm and a dispersion of 0.093nm/ch for the second one and a width of 30nm with a dispersion of 0.024 nm/ch for the third one.

The spectrograph has a Czerny-Turner configuration with a f-number of f/4. The entrance slit' s width is computer controlled in a range between from 10 μm to 2 mm.

The spectrometer calibration was performed using a krypton lamp and the spectra acquired with different grating used to calculate dispersion and to calibrate spectrometer are in figure 3.8.

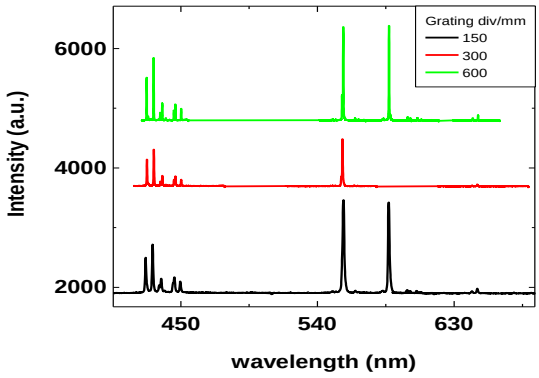

Figure 3.8. *The figure shows three spectra of a krypton lamp used to calibrate the spectrometer*

3.4 CCD

The CCD is the last component of acquisition apparatus which image is stored via camera controller to computer.

The camera controller controls the acquisition's parameters like start, stop of acquisition, gain and other functions as the gate function useful for noise suppression.

The CCD is a scan inter-line CCD with 1064×1280 pixels. The incident photons generate electrons on CCD photodiodes and generated electrons are transferred from photodiodes to one chip amplifier, which converts the electrons to voltage, by using the vertical CCD and horizontal CCD. By supplying the readout signal to the sensor gate, all generated charges are transferred to vertical CCD, then to horizontal CCD and then all charges reach the on-chip amplifier.

This CCD has an electrical shutter function, enabling this function all integrated charges in photodiodes are dumped to the silicon base instantaneously.

It's possible to use binning function to enhance signal/noise ratio in exchange of resolution.

There are 3 kind of binning method with 3 different binning factor (2×2 , 4×4 , 8×8). The binning factor of $n \times n$ means that charges in n^2 near pixels are added in the CCD chip. Thus the signal increases n^2-fold, although total pixel number decreases n^2 times and readout speed increases n-times.

3.5 Acquisition software

All previous components (streak, CCD, spectrometer) are driven by computer through the software HPD-TA of Hamamatsu. The acquisition parameters are controlled via software and is possible to see the image on screen in real time. The acquired image can be saved in ASCII format, in this case it is just a matrix which elements represent the intensity of every pixels.

It is possible to acquire and to save a sequence of images that can be used to perform some correction (see later). In software, several useful tools are available to improve the image's quality and to correct the acquisition's imperfections. The corrections available are: 1) background subtraction, 2) shading correction, 3) jitter correction, 4) defect pixels correction and 5) curvature correction. Below only corrections 1,2 and 3 are explained because they are the corrections utilized in this work.

Background subtraction. The acquired image contains also the background noise that can be subtracted from the image. To do it an image of background is saved and the program automatically subtracts the background in every acquisition and it's possible to subtract the background also in a sequences in real time. When this operation is carried out in final image some pixels can be negative but it's possible to set the program to clip to zero the values of these pixels during background subtraction.

Shading correction. This command corrects non-uniform intensity of an image. The non-uniformities is due to the non-uniformities of imaging's system due to several reasons like uneven illumination, lens shading, different sensitivity of CCD pixels, non-flat width of input slit (especially for small slit width) or non-linearity of streak's sweep which leads to a slowly varying signal amplitude along the time axis. All these effect can be compensated by multiplicative correction called shading correction.

To perform this correction the image of a white and constant (in time) source is needed (reference shading image S), the image should be uniform, if it is non-uniform calculating the intensity distribution it's possible to know the shading of system. After background subtraction on acquired image (D) and on reference shading image S the final image is:

$$C(x,y) = k\frac{D(x,y)}{S(x,y)}$$

where k is a constant calculated to avoid the overflow of data and the notation (x,y) means that the operation is carried out pixel by pixel.

It is possible to perform shading correction in real time and on the sequences too.

Jitter correction. The start of sweep, as above explained, is triggered by an electrical signal with repetition frequency of laser. The temporal distance between the electric signal and optical pulse can be non constant in time and it can oscillate around a value t_0 according to a particular distribution function G(t). This effect, called jitter, introduces a worsening of instrument's resolution because an image acquired through several acquisition should contain the convolution of function G(t) with function describing the real phenomena.

In the software is available the jitter correction function, this function operates on a sequence of images in following manner: firstly it extracts profile from the image along the full length of time axis at the area which has been defined during data setup called "Area for fixed points". Then it searches the global maximum along the profile and calculates the centre of gravity around the maximum in a region which width has been defined by user. Finally, it checks whether this fix point is within the area for fix point detection. If it is outside this sample is excluded automatically from further analysis.

When all fix points are defined the system will shift all samples in a way that the fix points of all samples will be placed to the same place and then overlay (add up) all samples. Only portions of the samples will be used which are present in all samples. The resulting sample will therefore be shrunk along the time axis.

In figure 3.9 are shown two decays due to exciton recombination in a zinc oxide crystal acquired without jitter correction (black line) and using jitter correction (red line). The jitter effect implies an overestimation of time constant as shown in figure 3.9 that is the most important parameter of time resolved measurement. The jitter correction, also if reduces the acquisition speed of about one order of magnitude if sequence of images is stored on RAM and 20 times if is stored on hard disk, is needful when are used range lower than 5 ns.

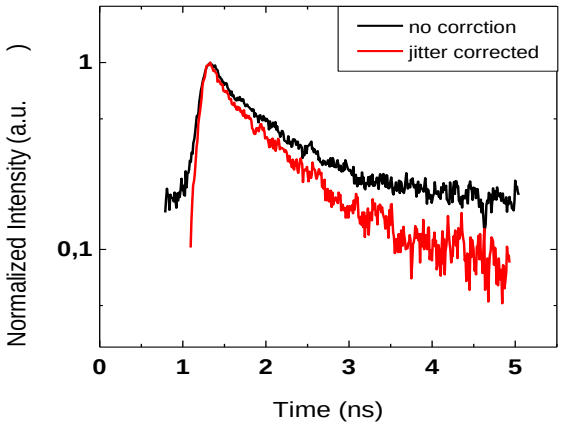

Figure 3.9. *The figure shows two decays acquired with jitter correction (red curve) and without (black curve).*

Chapter 4

Gas Sensing Applications

As discussed in previous chapters ZnO represents an important material for several applications. In this thesis, a first session of measurements was performed to investigate the possibility of using ZnO in gas sensing application.

The gas chosen to test material behavior is nitrogen dioxide (NO_2), which is a very toxic gas produced in many ordinary combustion processes. NO_2 provokes irreversible lung damages also in very small concentration in fact the Italian legislation set the attention level to 0.1 part per million (ppm).

The now-day sensors are based on chemioresistive response of material, due to variation of space charge layer size induced by adsorption of gas molecules. The change of space charge layer dimension originates a change of resistivity, so that applying a voltage and measuring the current intensity it is possible to detect gas by means of current intensity variation.

Another route to gas sensing, alternative to the standard approaches based on chemoresistive response, is based on the modification of material optical response induced by interaction with gas molecules. This approach ('optochemical sensing') may present a number of advantages over the traditional chemoresistive sensing. As electromagnetic waves are described by a certain number of degrees of freedom (intensity, wavelength, polarization); optochemical sensing allows multi-parametric detection, which is not possible in electrical sensing where only a single scalar quantity (electrical conductivity) is involved. Optical sensors do not need electrical contacts, do not suffer

from electromagnetic noise and may allow optoelectronic integration. Different optical responses may be involved in optochemical sensing, such as reflectance, optical absorption, surface plasmon resonances or photoluminescence (PL). The approaches based on PL appear promising in the case of nanostructured metal oxide as SnO_2 [43], a same kind behavior its possible also in ZnO and the first part of measurement in this thesis starts from this thought.
For a better understanding of experimental result, it is useful to show a simple model describing adsorption process which will help interpretation of experimental data. Then an explanation of two possible quenching mechanisms will be given and finally the experimental results.

4.1 Adsorption and Langmuir model

The adsorption is a phenomenon happening on separation surface between two different materials and is the capture of gas molecules by solid surface, for sake of simplicity only the case of solid-gas interface will be considered. Molecules impact continuously on solid surface, at same time a part of adsorbed molecules will be desorbed, in dynamic equilibrium condition the impact rate per unit area (impingment) is equal to desorption rate to keep constant the number of adsorbed molecules.
By means of kinetic theory of gas the impingment is given by:

$$I = \frac{p}{\sqrt{2\pi mkT}}$$

where p is the gas pressure and m the gas molecules mass. Near surface a molecule undergoes an attractive force at large distance and a repulsive one at small distance (figure 4.1) the adsorbed molecule will lie at equilibrium distance r_a that is of order of few Angstroms.

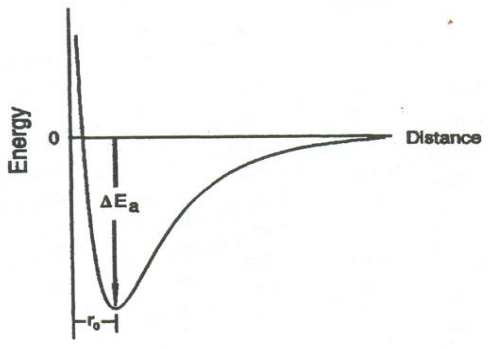

Figure 4.1. *The picture shows a molecule potential energy due to surface* .

The value ΔE_a shown in figure depends on kind of interaction (chemical bounding, van der Waals…).

The desorption frequency v_{des} (the inverse of desorption meant time) can be approximated by following expression:

$$\frac{1}{\tau_a} = \upsilon_{des} = \frac{1}{\tau_0} exp\left(-\frac{\Delta E_a}{kT}\right)$$

At equilibrium condition the impingement is equal to desorption rate E, so using:

$$E = \frac{n_a}{\tau_a} \quad [\#\text{ of molecules / cm}^2\text{ sec}]$$

where n_a is the population of adsorbed molecules per square centimeter; we have the equilibrium equation:

$$E = I \qquad \rightarrow \qquad \frac{n_a}{\tau_a} = \frac{p}{\sqrt{2\pi mkT}}$$

$$\text{so:} \quad n_a = \frac{p}{\sqrt{2\pi mkT}} \tau_0 exp\left(\frac{\Delta E_a}{kT}\right)$$

It's important to remember that ΔE_a can depend on n_a.

Next we assume that the adsorbed molecules doesn't move on surface and only one molecule can occupies a surface site so τ_a has a finite value when molecules impact an empty site and a null value when the site is occupied. Then taking into account this effect we have:

$$n_a = I\left[1 - \left(\frac{n_a}{n_0}\right)\right]\tau_a$$

where n_0 is the density of available sites. Solving respect n_a we have:

$$\theta \equiv \frac{n_a}{n_0} = \frac{\frac{I\tau_a}{n_0}}{\left[1 + \left(I\frac{\tau_a}{n_0}\right)\right]}$$

substituting the expression of I and defining $\chi \equiv \frac{\tau_a}{n_0}\left(\frac{1}{\sqrt{2\pi mkT}}\right)$ the final expression of θ is:

$$\theta = \frac{\chi p}{1 + \chi p}$$

The isothermic behavior of θ as function of pressure is shown in figure 4.2, θ shows a linear behavior for low values of pressure. This model works better in systems that shows strong adsorption because only in these systems it's possible to neglect interactions among adsorbed molecules.

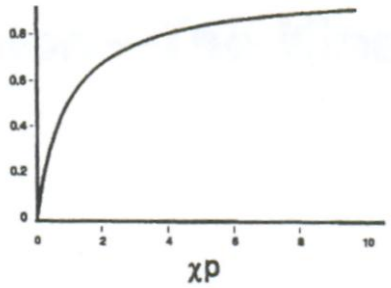

Figure 4.2. *The picture shows the functional form of θ as function of gas pressure.*

4.2 Static quenching and dynamical quenching

Sometimes the adsorbed molecules can interact with material decreasing the photoluminescence yield, this mechanism is called quenching.

When the gas molecules originate new non-radiative recombination mechanisms, the number of excited states (created by optical excitation) starts to decreases by means of usual decay mechanisms (present also when material is immersed in vacuum) and by means of the new recombination channels introduced by the quencher gas. The result is that the total emitted radiation is decreased and also the recombination time of decay is reduced. This kind of quenching is called dynamical quenching and it occurs when the decay constant is larger then τ_a.

An assumption of Langmuir model is that the gas molecules don't interact each other or in other words that the gas-solid interaction is much stronger that gas-gas interaction. It means that after an absorption process the same molecule takes a long time before leaves surface ($\tau < \tau_a$ statical quenching). So when the interactions between solid and gas molecules are weak, the Langmuir model condition is no longer verified, for this reason the Langmuir model is not applicable to dynamical quenching mechanism.

Another possibility is the decreasing of luminescence intensity without a change of decay time, in this case the mechanism is called static quenching. The adsorbed molecules simply quench the number of excited states leading in a diminishing of radiative recombination.
In the case of dynamical quenching the adsorbed gas molecules introduce new non-radiative recombination centers Q_{ads} (in addition to recombination centers X of material when the gas is absent) so the possible processes are:

1) Excitation $X + h\nu \rightarrow X^*$ (where * indicates excited states)

This process is proportional to pump intensity I_{uv} (neglecting non-linear absorption)

2) Radiative decay $X^* \rightarrow X + h\nu'$

proportional to X* trough constant of process (K_r)

3) Non-radiative decay due to quenching $X^* + Q_{ads} \rightarrow X + Q_{ads}^*$

proportional to X* trough constant of process (K_q)

4) non radiative decay (also when quencher is absent) $X^* \rightarrow X + h\nu_{fon}$

proportional to X* trough constant of process (K_{nr})

The rate (W) of previous reaction are respectively:

$W_{ecc} = \alpha I_{uv} [X]$ $W_{pl} = K_r [X^*]$ $W_q = K_q [X^*] [Q_{ads}]$ $W_{nr} = K_{nr} [X^*]$

The dynamical equation is:

$$\frac{d([X] + [X^*])}{dt} = 0$$

and steady state equation is:

$$\frac{d[X]_{ss}}{dt} = \frac{d[X^*]_{ss}}{dt} = 0$$

When the quencher is absent the balance equation is:

$$W_{ecc} = W_{pl} + W_{nr}$$

using the rates expression:

$$[X^*]_{ss} = \frac{\alpha I_{uv}[X]_{ss}}{K_D}$$

where $K_D = K_r + K_{nr}$

So the PL intensity I_0 becames:

$$I_0 = K_r\,[X^*]_{ss} = \frac{\alpha\, I_{UV}\,[X]_{ss}\, K_r}{K_D}$$

When the dynamical quenching occurs the quencher changes the steady states equations producing:

$$\alpha\, I_{UV}[X]_{ss} - K_D[X^*]_{ss} - K_q[X^*]_{ss}\, Q_{ads} = 0$$

and so:

$$[X^*]_{ss} = \frac{\alpha\, I_{uv}\,[X]_{ss}}{K_D + K_q\,[\,Q_{ads}]}$$

And PL intensity becomes:

$$I = \frac{\alpha\, I_{uv}\,[X]_{ss} K_r}{K_D + K_q\,[\,Q_{ads}]}$$

The ratio between non-quenched PL intensity and quenched PL intensity is:

$$\frac{I_0}{I} = 1 + \frac{K_q}{K_D}[\,Q_{ads}]$$

Defining $K_Q = Q_0 K_q$ where: $Q_0 = \frac{Q_{ads}}{\theta}$

We have: $\frac{I_0}{I} = 1 + \frac{K_Q}{K_D}\theta$

using Langmuir model it becomes: $\frac{\mathrm{I_0}}{\mathrm{I}} = 1 + \frac{\mathrm{K_Q}\ \chi\ \mathrm{p}}{\mathrm{K_D}\ (1+\chi\ \mathrm{p})}$

The previous equation shows a linear behavior for small pressure and saturation with an asymptote when $\mathrm{p} \rightarrow \infty$ which equation is:

$$\frac{\mathrm{I_0}}{\mathrm{I}} 1 + \frac{\mathrm{K_Q}}{\mathrm{K_D}}$$

The ratio $\frac{\mathrm{K_Q}}{\mathrm{K_D}}$ represent the quencher intensity.

In the case of static quenching the effect consists in a diminishing of steady state without introducing another recombination channel, using a linear dependence of $[\mathrm{X}]_{\mathrm{ss}}$ on $\mathrm{Q_{ads}}$ we have:

$$[X]_{ss} = [X_0]_{ss}\ (1 - \alpha'[\ Q_{ads}])$$

Using adimensional quantities: $\alpha' Q = \alpha' \theta\ Q_0 = \alpha\ \theta$

We obtain:

$$[X]_{ss} = [X_0]_{ss}\ (1 - \alpha\ \theta)$$

So: $\frac{I_0}{I} = \frac{1}{1-\alpha\ \theta}$

and using Langmuir model becomes:

$$\frac{I_0}{I} = \frac{1 + \chi\ p}{1 + (1 - \alpha\ )\ \chi\ p}$$

In this case: $\alpha = \frac{1}{\theta}\frac{\Delta[X]}{X_0}$ is a measure of gas ability to destroy radiative recombination centers [44].

4.3 Gas-induced PL quenching effects

Photoluminescence response to gas exposure was investigated and experimental results interpreted by means of the model reported in previous paragraph.

The visible PL spectrum was analyzed as it is most likely related to surface states and thus exhibits a strong interaction with environment, being more appropriate for gas sensing applications.

The sample utilized for measurements are ZnO nanowires, the reason of this choice is the large surface to volume ratio. The samples were fabricated by SENSOR Lab in University of Brescia that characterized also the samples by scanning electron microscopy (SEM).

ZnO nanowires were prepared by means of vapor transport process, in which the source material is vaporized and transported by a gas carrier towards the substrates, where it condenses. The experimental set up consists in a furnace capable to reach temperatures needful for oxide evaporation, a vacuum-sealed alumina tube connected to a primary pump, an automated valve and a mass flow meter to control pressure and carrier flow. The deposition conditions have been tailored in order to promote formation of one-dimensional (1D) nanostructures, through changing the evaporation temperature, the carrier gas composition and flow. In order to have a higher uniformity of the nanowires lateral dimensions, the catalysed-assisted growth has been used following the Vapour–Liquid–Solid growth mechanism (VLS). Moreover this type of growth allows selective growth of ZnO nanowires only where gold particles are deposited, thus giving a powerful tool to define sensor layout. Gold catalyst particles were firstly dispersed onto silicon substrates by DC magnetron sputtering at a working pressure of 5×10^{-3} mbar and 70W applied power. The source material was positioned in the middle of the alumina tube, evaporated at a temperature of 1370 $^{\circ}$C and a pressure of 100 mbar. The gold catalysed substrates were placed onto an alumina holder and positioned inside the tube in an area corresponding to a temperature range between 300 $^{\circ}$C and 500 $^{\circ}$C. Furnace heating from room temperature (RT) to 1370 $^{\circ}$C took 1.5 h. During furnace heating and cooling a reverse Ar gas flow (from the substrates to the powder) was applied, to avoid uncontrolled mass deposition under transient conditions. Once desired temperature was reached, the deposition conditions were kept stable for 20min, then the furnace was finally cooled down to RT.

SEM operating at 15kV was employed to determine the morphology of the nanowires. The nanowires are homogeneously deposited over large area substrates; their lateral dimensions depend on the deposition parameters and their length depends on deposition time. Figure 4.3 reports a SEM picture of the nanowires, the length is several microns while the width is 300 nm approximately. A net of nanowires can be observed, this open structure features large accesses for gas penetration,

while many layers of meshed nanowires provide large optical signal. The growth is along the c-axis of the hexagonal crystalline arrangement.

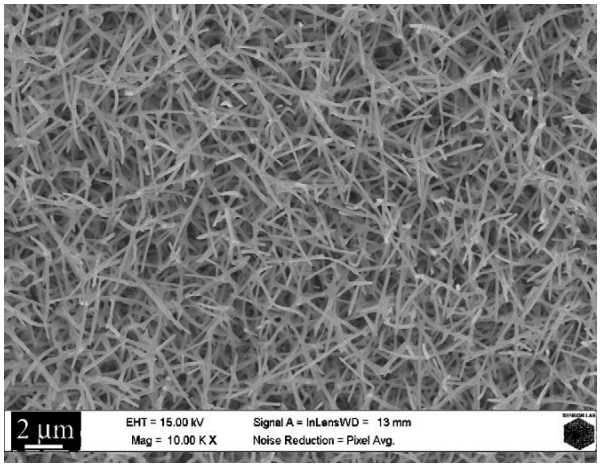

Figure 4.3. *SEM image of a ZnO nanowires sample*

In order to perform continuous-wave photoluminescence characterizations, samples were placed inside a test chamber kept at room temperature (T=20°C), with quartz windows granting easy access for optical measurements. A constant flow of synthetic air at 0.2 l/min, mixed with a desired amount of gaseous species (coming from certified bottles), flowed through the chamber at 20°C and atmospheric pressure. PL measurements were performed using a He–Cd laser as light source at 325nm. PL spectra were acquired perpendicular to the sample surface using a single spectrograph and a Peltier cooled CCD camera.

To study the dynamic behavior of PL with gaseous species, we acquired PL spectra of the visible band every 5s. To have stable baseline signal, dry air was usually fluxed into test chamber for not less than half an hour. Then gas diluted in dry air was introduced and flowed until steady state PL signal in gas was observed. After that, dry air was flowed until the recovery of baseline signal was obtained. In this way, parameters like relative variation, response and recovery time were calculated. In order to quantify the total PL quenching induced by gas exposure, it is useful to define a total PL yield Φ by integration of the PL spectral data over the emission wavelength interval $\Phi = \int \varphi(\lambda) d\lambda$, where $\varphi(\lambda)$ is the measured PL spectrum. In order to compare different results, relative variation of PL yield is calculated as follows, both for oxidizing and reducing gases:

relative variation $\frac{\Delta\Phi}{\Phi_{air}} = \frac{|\Phi_{gas} - \Phi_{air}|}{\Phi_{air}} \times 100$

Response time is defined as the time needful to reach 90% of the steady state response after gas is let in, while recovery time is defined as the time needful to recover 70% of the steady state value

after air is restored. Figure 4.4 shows the spectrum of ZnO nanowires acquired in dry air before measurements as reported in literature, UV exciton peak at 3.2 - 3.3 eV and visible band at about 2.5 eV were observed.

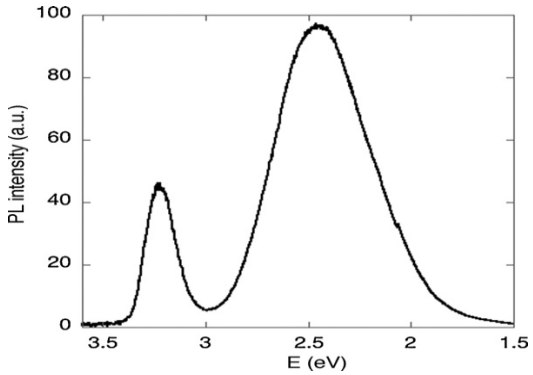

Figure 4.4. Spectrum of ZnO nanowires sample in dry air environment.

After NO_2 introduction, quenching of the PL signal was observed without concomitant peak shift. The quenching was fully reversible as dry air is restored in the test chamber.

Figure 4.5 reports the dynamic response of ZnO nanowires at RT towards low concentrations of NO_2 diluted in dry air.

NO_2 concentration of 0.1 ppm in air was detected with a relative variation of 2.3%, while 0.2ppm of NO_2 induced a relative variation of 3.3%. Italian legislation (following rules of European commission) fixed attention and alarm level for NO_2 presence outdoor to 0.1ppm and 0.2ppm respectively; we can thus affirm that our sensor can easily reach the levels needful for NO_2 monitoring in dry air.

Response time is of the order of 10 min. Once NO_2 is removed from the test chamber and replaced by dry air, NO_2 is desorbed from the surface and the PL signal recovers to initial value with a recovery time of the order of 8min. Indeed, sensing dynamic should be accelerated before ZnO optical sensors can be used for a real application. The parameters that influences response and recovery times are currently under investigation. Relative variations for dynamic quenching are reported versus NO_2 concentrations in right side of figure 4.5, where the points are experimental values, while the dashed line is a fit based on Langmuir function.

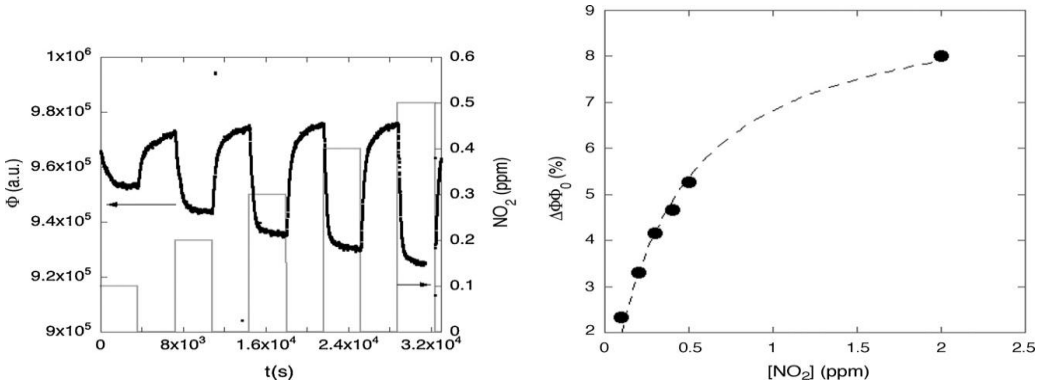

Figure 4.5. *Left: dynamic PL quenching versus time as stepwise NO_2 concentration in the sub-ppm range (right vertical axis) are introduced into test chamber. Sensor was kept at room temperature. Right: relative variation of PL yield versus NO_2 concentration (full circles: data points; dashed line: best fit curve based on the Langmuir function).*

To further investigate gas sensing application, we studied the effect of common interfering gases like ethanol and relative humidity. In ambient air, the presence of changing relative humidity (RH) and of other gases could give spurious signal. The results are reported in figure 4.6, where the dynamic variations of PL yield are plotted for NO_2, ethanol and humidity introduction. A quenching of 8% was observed with 2ppm of NO_2, while the opposite effect was observed with ethanol and RH, which acted as PL enhancer. The relative response to ethanol concentration (1000 ppm) was 1.5%. The PL increasing with RH gave relative response of 2.8%, 3.9% and 4.6% respectively to 20%, 50% and 70% RH, so this interfering effect must be taken in account when dealing with all-optical gas sensor.

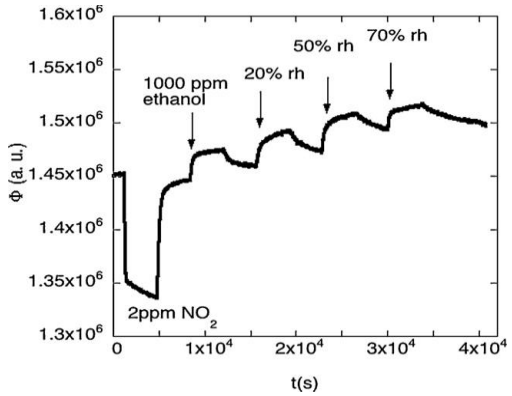

Figure 4.6. *Dynamic of PL quenching and enhancing versus time as stepwise NO_2 ,ethanol and humidity are introduced into test chamber*

The desorption kinetic in the case of humidity is slower than in the case of NO_2 and ethanol, and the recovery of baseline signal after dry air restoration is obtained after three hours (not shown).

Even if this could be a problem for the sensing application, it should be considered that changes from 70% RH to completely dry air is an unlikely event in atmospheric conditions where the sensor could find an application.

4.4 Gas exposure effect on recombination lifetime

A deeper view of the physical mechanisms lying behind the adsorption-related PL modifications can be obtained by investigation of the excited state lifetimes by means of time-resolved photoluminescence (TRPL) technique. The experimental setup is explained in chapter 3.

Photoluminescence time profile in this measurement is obtained with a resolution of about 50 ps. The wavelength detection interval was centered near the peak of the green emission by using a band-pass optical filter allowing detection only in the range 470–530 nm. The samples investigated through TRPL technique were placed inside a test chamber in which a constant flux of synthetic air mixed with the desired amount of nitrogen dioxide, which was flowed through the chamber at 20 ˚C and atmospheric pressure. Three different samples of ZnO nanowires were characterized in dry air and NO_2 environment.

All the samples exhibit TRPL decay curves of ZnO green emission with no simple mono-exponential decay shape. Most importantly, no significant deviation of the decay profiles was observed once NO_2 flow was introduced inside the test chamber. This effect was observed for all the investigated samples and an example is reported in figure 4.7, where the normalized TRPL curves are reported for the case of a ZnO nanowires sample under dry air flow (black full line) and under 30ppm concentration NO_2 flow (blue full line). It can be clearly seen that TPRL curves show very similar decay slopes, after normalizing their experimental values to counterbalance the PL quenching due to NO_2.

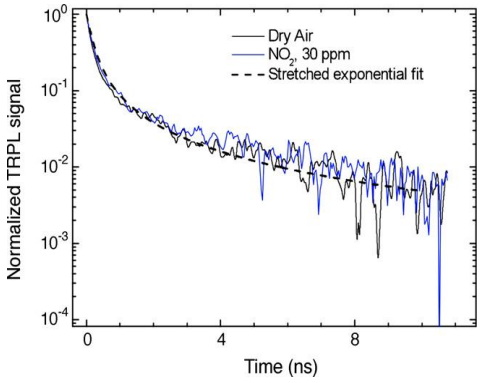

Figure 4.7. *PL decays in dry air (black line) and 30 ppm NO_2 (blue line).*

As the TRPL decay of green band of ZnO does not follow single-exponential behavior, the recombination dynamics is characterized by a finite distribution G(k) of decay constants k. Such distribution is by definition related to the TRPL decay profile by the equality:

$$I_{PL}(t) = \int_0^\infty G(k) exp\,(-kt) dk$$

and can thus be obtained as the Laplace transform of the TRPL decay profile. In order to determine the G(k) corresponding to the measured TRPL curves, the experimental decay profiles was fitted using a Kohlraush stretched exponential function

$$I_{PL}(t) = I_0 exp\left[-\left(\frac{t}{\tau_0}\right)^{\beta}\right]$$

whose inverse Laplace transform can be obtained through the formula developed by Berberan–Santos [45].

The values of fitting parameters are:

$\tau_0 = 0.2 \pm 0.01ns$, $\beta = 0.63 \pm 0.02$ (dry air curve)

$\tau_0 = 0.2 \pm 0.01ns$, $\beta = 0.63 \pm 0.02$ (NO_2 curve)

The resulting distribution of decay constants (G functions) is reported in figure 4.8. It can be noticed that the shapes of distribution functions look very similar. There are only small differences in G functions peak positions (0.56GHz in dry air and 0.57GHz in NO_2). An average decay constant can be defined through the expression:

$$\langle k \rangle = \frac{\int_0^{\infty} kG(k)dk}{\int_0^{\infty} G(k)dk}$$

The results $\langle k \rangle$ = 0.68GHz and 0.67GHz are obtained for the case of the dry air and NO_2 curves respectively, corresponding to an average lifetime $\langle k \rangle^{-1}$ of 1.47 ns and 1.48 ns. However, such results cannot be really considered as numerically distinct, once one takes into account of the uncertainty (of the order of 5%) affecting the lifetimes as obtained by the best fits. To the best of the resolution of our measurements, we can say that no significant difference in the lifetime distribution is observed once interaction with NO_2 is introduced.

These results suggest that the NO_2 molecules act as static quenchers, leading to an overall reduction of the radiative events that give rise to the luminescence band.

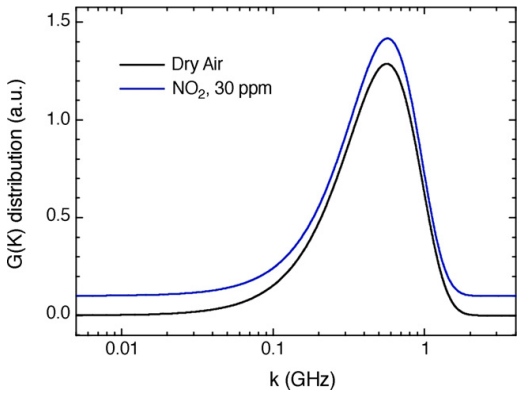

Figure 4.8. *Laplace transforms of PL decays in dry air (black line) and 30ppm of NO_2 (blue line).*

Chapter 5

Visible and UV emission in nanowires

In the previous chapter was shown the relationship between luminescence properties of ZnO nanowires and possible gas sensing application, instead the aim of this paragraph is the study of ZnO emission properties and the possible applications in the field of emitting device.
To carry out this analysis is required a study of mechanisms responsible of UV emission, important for emitting devices, and mechanisms of visible luminescence that probably affects UV emission. It is important to study these two emissions for different injection conditions and how these emissions interact each other in non equilibrium condition (during decay).

5.1 Correlation between UV and Visible emission

The visible emission intensity, that is probably generated by surface states [26], depends on sample specific surfaces so in the nanostructures it is enhanced.
For this reason the analysis of visible luminescence was performed on nanowires, as it can be seen by figure 5.1 the ratio between visible and UV intensity is larger in nanowires in comparison with bulk crystal especially if the sample is excited by means of a pulsed laser as Nd:YAG as it will be explained in next chapter.

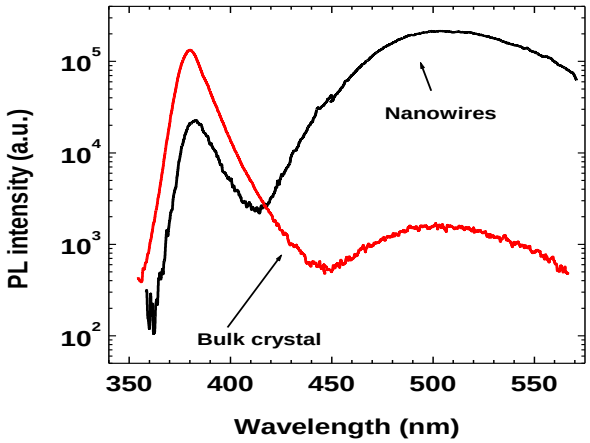

Figure 5.1. *In figure is showed the spectrum of ZnO bulk (red curve) and spectrum of ZnO nanowires (black curve) obtained using Nd:YAG as excitation source. It is clear that the ratio between UV and visible intensity is larger in bulk crystal.*

The aim of this paragraph is to investigate about the possible correlation between UV and visible luminescence emission mechanisms and their eventual interaction in non-equilibrium condition. In order to do it, I developed a model for coupled UV and visible emission in an ideal three-bands system representing valence band (band 1), deep intragap states responsible of Vis emission (band 2) and conduction band (band 3).

The model is next described and its predictions are tested in next paragraph by performing time-resolved PL measurements for both UV and VIS emission on ZnO nanowires samples prepared at University of Brescia (CNR-SENSOR Lab). Samples have been prepared with same process of samples used for measurement shown previously.

In principle one of two possible following situations reflects system behavior: 1) the deep defect states responsible of Vis emission are empty, the radiation excites electrons from valence band to conduction band, the electrons relax to conduction band minimum and to intragap states exciting these states that emit visible luminescence. 2) The deep defect states are occupied, and the radiation excites electrons from valence band to conduction band while no excitation from valence band to deep defect states occurs due to Pauli exclusion principle .

After interband excitation, electrons in CB band can relax by fast non-radiative recombination to CB minimum and to intragap states and then electrons in intragap states can recombine with valence band holes (that now is partly emptied due the excitation) emitting visible photons.

During emptying of intragap states, due to recombination, electrons from CB continue to populate intragap states by phonon collisions and electron-electron collisions.

To have information on equilibrium population of three bands a photoluminescence excitation spectrum (PLE) of visible peak was acquired (figure 5.2).

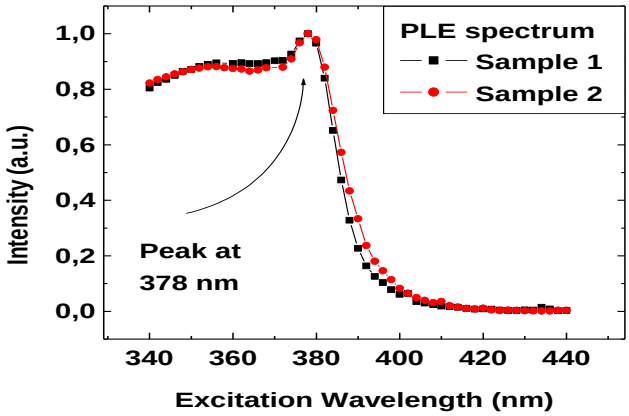

Figure 5.2. In figure is showed the visible PL intensity on vertical axis and corresponding excitation wavelength on horizontal axis. The PLE is negligible at wavelength higher than ~ 400 so to excite intragap states is needful a more energetic radiation, the peak centered at 378nm correspond to exciton states.

The PLE spectrum in figure represents the emission intensity of visible band (area of visible emission peaked at E_{intr} ~ 2.4 or 510 nm) collected at different excitation wavelength. From the figure we can see that a photon energy equal to band gap (or larger) is needful to induce excitation, so the visible states at energy E_{intr} are not excited directly by photons of same energy.

The first of two situations described above (empty intragap states) is not possible as it can be seen by PLE spectrum, in fact if deep states were empty the PLE spectrum should be nonzero at energy comparable with E_{intr} because this radiation should be sufficient to be absorbed by electron in VB that should leave it to move toward empty deep defect states but it doesn't occur. To confirm PLE result also a PL spectrum was collected using line at 442nm of HeCd laser that, as expected, doesn't induce emission.

So we assume that the deep defect states are occupied then to excite an electron is needful a radiation with photon energy of order of bandgap or larger.

In figure 5.3 is represented this case before excitation, after excitation in non-equilibrium condition and after phonon scattering in quasi equilibrium condition.

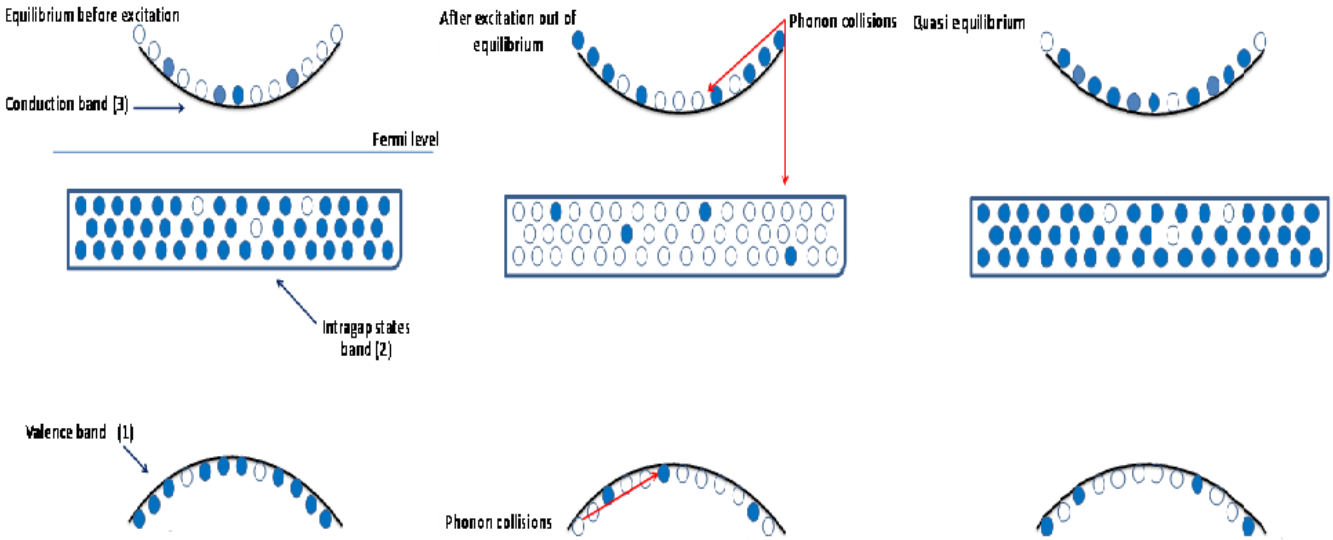

Figure 5.3. *The figure shows the band diagram in equilibrium condition (first picture), after excitation out of equilibrium (second picture), and after that electrons relax in quasi equilibrium states via phonons and electron-electron collisions. The white circle represent the holes and blue circle the electrons.*

Using the band scheme in figure, in the next paragraph will be exposed a model that try to describe time dependent UV and visible luminescence.

5.2 Three bands Model

We want to write a system of differential equations whose incognitos are the holes and electrons population in valence band (band 1), intragap states (band 2), and conduction band (band 3). Moreover we want to find the connection between the solution of equations and measurable quantities like time integrated PL intensity and time resolved PL intensity in green and UV region for different pump energy.

The equations describing the system are the following:

$$-\frac{dn_3}{dt} = \beta_{31}(n_3p_1 - n_3^0p_1^0) + \beta_{32}(n_3p_2 - n_3^0p_2) \qquad \text{band 3 (conduction band)}$$

$$-\frac{dn_2}{dt} = -\beta_{32}(n_3p_2 - n_3^0p_2) + \beta_{21}(n_2p_1 - n_2^0p_1^0) \qquad \text{band 2 (intragap states)}$$

$$-\frac{dp_1}{dt} = \beta_{31}(n_3p_1 - n_3^0p_1^0) + \beta_{21}(n_2p_1 - n_2^0p_1^0) \qquad \text{band 1 (valence band)}$$

Where the symbols n and p represent the density of electrons and holes, the numerical index represent the band.

The second step consists in solving equations and relating the density to observable quantities like intensity of visible and UV as time function and as pump energy function.

The following assumption is demanded:

1) The coupling constants satisfy following relations $\frac{\beta_{32}}{\beta_{31}} \gg 1$ and $\frac{\beta_{32}}{\beta_{21}} \gg 1$

Where β_{32} is the coupling constant between conduction band and intragap states, β_{31} between conduction band and valence band and β_{21} between intragap states and valence band.

This assumptions mean that, after the excitation, electrons in conduction band are immediately captured by intragap states until filling these states.

This assumptions have a theoretical and an empirical justification:

a) in a n-type semiconductor with deep intragap states the capture cross section σ_n, that is related to β_{32} by thermal velocity of electrons, is much larger than the capture cross section σ_p of an hole in valence band that is related to β_{21} [46].

b) if the visible signal and pump are acquired, they start at same time then the transfer time of electrons between conduction band and intragap states can be assumed instantaneous.

In conclusion the model aims to describe the following process:

the radiation excites electrons from valence band to conduction band and from intragap states to conduction band bringing the system out of equilibrium. In some hundreds of fs the phonon collisions and electron collisions relax the electrons from high level of conduction band to the minimum of band and from conduction band to intragap states. Now the system is described by a quasi Fermi statistic for electrons and for holes, this time represents the zero instant of the model. The model describes what happen to populations of the bands after this time (figure 5.3).

Consequentially the densities of electrons $n_2 = n_2^0$ and holes $p_2 = p_2^0$ in intragap states (band 2) are constant, where the index 0 represents the density before excitation. If the index e represents the excess population due to excitation.

We have:

$$n_3 = n_3^e + n_3^0$$

$$n_2 = n_2^0$$

$$p_1 = p_1^e + p_1^0$$

$$p_2 = p_2^0$$

Using the rate equations, the bands populations are related to measurable quantity in following way:

$$\varphi^{UV}(t) \propto \beta_{31}(n_3 p_1 - n_3^0 p_1^0)$$

$$\varphi^{Vis}(t) \propto \beta_{21}(n_2 p_1 - n_2^0 p_1^0)$$

Using the symbols for excited p and n populations the rate equations become:

$$-\frac{dn_3^e}{dt} = \beta_{31}(n_3^e p_1^e + n_3^0 p_1^e + n_3^e p_1^0) + \beta_{32} n_3^e p_2$$

$$\uparrow$$

$$\propto \varphi^{UV}(t)$$

$$-\frac{dn_2^e}{dt} = 0 = -\beta_{32} n_3^e p_2 + \beta_{21} n_2^0 p_1^e$$

$$\uparrow$$

$$\propto \varphi^{Vis}(t)$$

the third equation is needless.

Using second equation we have:

$$p_1^e = A\, n_3^e$$

where $A = \frac{\beta_{32}\ p_2}{\beta_{21}\ n_2^0}$

that substituted in the first one produces an equation for n_3^e :

$$-\frac{dn_3^e}{dt} = \beta_{31}\, A\, n_3^{e\,2} + \beta_{31}\, A\, n_3^0\, n_3^e + \beta_{32}\, n_3^e p_2 + \beta_{31}\, p_1^0\, n_3^e$$

In a n-type semiconductor it's possible to neglect the last term.

The solution of equation is:

$$n_3^e(t) = \frac{n_3^e(0) exp\left(-\frac{t}{\tau}\right)}{1 + \left(\frac{\beta_{31}\ n_3^e(0)}{\beta_{31}\ n_3^0 + \beta_{21}\ n_2^0}\right)\left(1 - exp\left(-\frac{t}{\tau}\right)\right)}$$

where $\frac{1}{\tau} = \frac{\beta_{31}\,\beta_{32}\;p_2\,n_3^0}{\beta_{21}\;n_2^0} + \beta_{32}\,p_2$

the temporal dependence of visible luminescence is:

$$\varphi^{Vis}(t) = K_{Vis}\beta_{32}p_2\;n_3^e(0)\frac{exp\left(-\frac{t}{\tau}\right)}{1+\;\gamma n_3^e(0)\left(1-exp\left(-\frac{t}{\tau}\right)\right)}$$

where K_{Vis} is a constant that depends on geometrical structure of experiment and

$$\gamma = \frac{\beta_{31}}{\beta_{31}\;n_3^0 + \beta_{21}\;n_2^0}$$

The temporal dependence of UV luminescence is:

$$\varphi^{UV}(t) = \frac{K_{UV}\beta_{31}\,\beta_{32}\,p_2\,n_3^0\,n_3^e(0)}{\beta_{21}\;n_2^0}\left\{\frac{\frac{n_3^e(0)}{n_3^0}exp\left(-\frac{2t}{\tau}\right)}{\left[1+\;\gamma n_3^e(0)\left(1-exp\left(-\frac{t}{\tau}\right)\right)\right]^2} + \frac{exp\left(-\frac{t}{\tau}\right)}{1+\;\gamma n_3^e(0)\left(1-exp\left(-\frac{t}{\tau}\right)\right)}\right\}$$

Then the model predicts two functions for temporal dependence of green an UV photoluminescence in which the time constant τ is the same.

The obtained functions $\varphi^{Vis}(t)$ and $\varphi^{UV}(t)$ show a different time dependence.

$\varphi^{UV}(t)$ decreases faster than $\varphi^{Vis}(t)$ because $\varphi^{UV}(t) \propto \varphi^{Vis}(t) + \frac{n_3^e(0)}{n_3^0}\varphi^{Vis}(t)^2$ and the quadratic term is faster than linear term.

In figure 5.4 are shown the normalized time dependences of a $\varphi^{UV}(t)$ (violet line) and $\varphi^{Vis}(t)$ (green line) for the following values τ =5, $\gamma n_3^e(0)$ = 1 and $\frac{n_3^e(0)}{n_3^0}$ = 1.

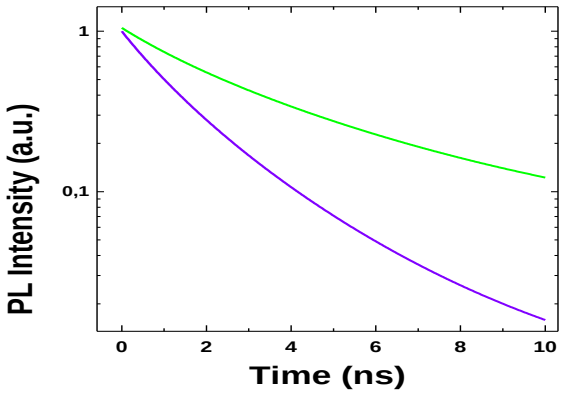

Figure 5.4. In figure are showed the simulation of UV and visible luminescence decays calculated using the result of three bands model.

5.3 Empirical test of three bands model

By the spectra (using third harmonic Nd:YAG and HeCd) shown in figure 5.5, we can see that UV/green PL ratio is larger when Nd:YAG is used. It is justified, in qualitative way, by model; in fact the model predicts (explained below) that the increasing of visible PL intensity as function of $n_3^e(0)$ is slower than UV PL. So the ratio between UV and green intensity is larger for Nd:YAG excitation because it is a pulsed laser and then it generates density of excited electrons larger than density generated by HeCd.

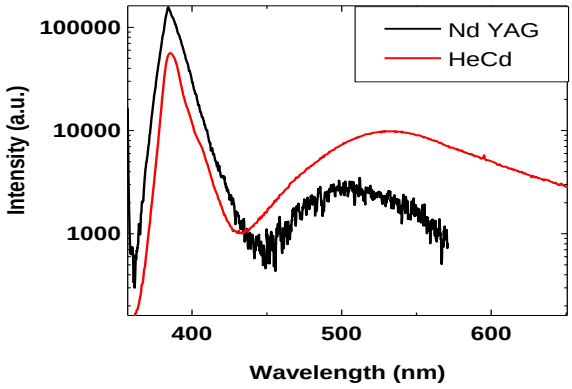

Figure 5.5. In figure are showed the PL spectra of ZnO nanowires using as excitation source Nd:YAG (black curve) and HeCd (red curve). It can be noted that the ratio between intensity of UV a visible is larger when Nd:YAG is used.

We can calculate the dependence of UV and visible on pump energy integrating $\varphi^{Vis}(t)$ and $\varphi^{UV}(t)$ and calculating the total UV and green intensity as $n_3^e(0)$ function.

$$\varphi_{Tot}^{Vis} = \int_0^{\infty} \varphi^{Vis}(t)dt = \frac{K_{Vis}\beta_{32}\, p_2}{\gamma} Log(1 + \gamma n_3^e(0))$$

$$\varphi_{Tot}^{UV} = \int_0^{\infty} \varphi^{UV}(t)dt = \frac{K_{UV}\beta_{31}\,\beta_{32}\, p_2\, n_3^0 \tau}{\beta_{21}\; n_2^0 \gamma^2} \left\{ \frac{\gamma n_3^e(0)}{n_3^0} + \left[\frac{\gamma n_3^0 - 1}{n_3^0} \right] Log(1 + \gamma n_3^e(0)) \right\}$$

Using a source with short pulses and low repetition rate it's possible to obtain high levels of $n_3^e(0)$ for which is possible to approximate the pervious expression with following one:

$$\varphi_{Tot}^{UV} = \frac{K_{UV}\beta_{31}\,\beta_{32}\, p_2\, n_3^0 \tau}{\beta_{21}\; n_2^0 \gamma^2} \left\{ \frac{\gamma n_3^e(0)}{n_3^0} \right\}$$

The number of excited electrons by laser source is:

$$n_3^e(0) \backsimeq \frac{\alpha\left(\frac{E}{S}, \nu\right) E(1-R)}{Sh\nu}$$

where α is the absorption coefficient, E is the laser pulse energy, S the spot area, ν the laser frequency, h the Plank constant and R the reflectance of sample.

The non linear dependence of absorption coefficient on $\frac{E}{S}$ ratio can be approximated by the following empirical expression:

$$\alpha\left(\frac{E}{S}, \nu\right) = \frac{\alpha_0(\nu)}{1 + \frac{E}{E_{Sat}}}$$

where $\alpha_0(\nu) = \lim_{E \to 0} \alpha\left(\frac{E}{S}, \nu\right)$ and E_{Sat} is a constant.

Inserting the expression for $n_3^e(0)$ and $\alpha\left(\frac{E}{S}, \nu\right)$ in the expression of φ_{Tot}^{UV} and φ_{Tot}^{Vis} we have:

$$\varphi_{Tot}^{Vis} = a * Log\left(1 + \frac{bE}{1 + \frac{E}{E_{Sat}}}\right) \qquad \varphi_{Tot}^{UV} = \frac{cE}{1 + \frac{E}{E_{Sat}}}$$

Where a, b and c are three constants related to model parameters. We can see that the functional dependence of φ_{Tot}^{UV} on laser energy is faster than functional dependence of φ_{Tot}^{Vis} justifying the behavior of UV/Visible ratio as pump power increases.

Concerning the time resolved curves, the model predicts that visible and UV photoluminescence follow the $\varphi^{Vis}(t)$ and $\varphi^{UV}(t)$ behavior respectively.

To test the model we measured the visible luminescence of samples for different pump energies (figure 5.6).

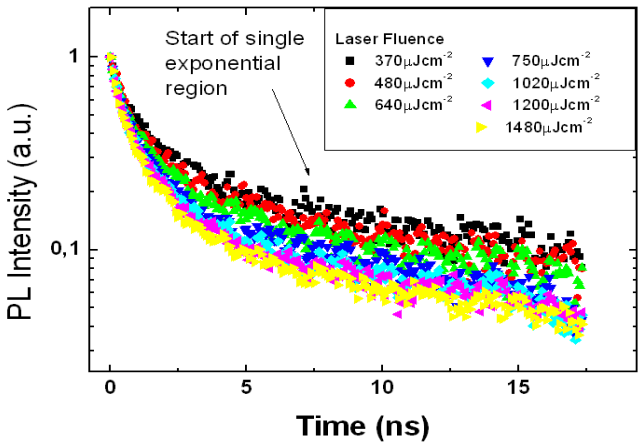

Figure 5.6. In figure are showed the normalized decays of visible luminescence (integrated between 460 and 560nm) for different laser fluences. The decays show a first part which slope depends on laser fluencies and a second part (after about 8ns) where all curves are single exponential with same lifetime.

After about 10ns, as showed in figure, the slopes of each curve on Linear-Log scale become constant and equal to each other.

All decays for t >10ns were fitted with a single exponential function and the estimated value of τ was used to fit the same curves for all time by means of model's function $\varphi^{Vis}(t)$:

$$\varphi^{Vis}(t) = K_{Vis}\beta_{32}p_2\, n_3^e(0)\frac{exp\left(-\frac{t}{\tau}\right)}{1+\ \gamma n_3^e(0)\left(1-exp\left(-\frac{t}{\tau}\right)\right)}$$

Three visible decays for different pump energies are shown in figure 5.7 with corresponding fits.

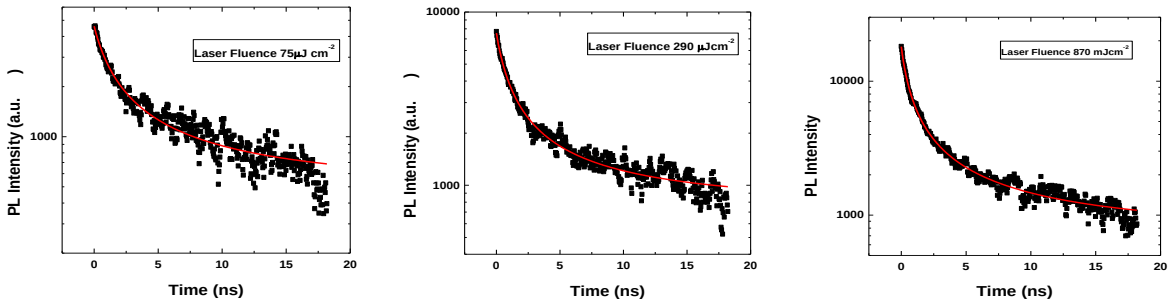

Figure 5.7. In figure are showed three decays integrated between 460 and 560 nm for different laser fluences and the corresponding fitting function obtained from equation describing the visible PL temporal behavior in three bands model.

To test the fitting procedure is necessary to verify a feedback on estimated parameters.

In fact could be possible to fit decays, at different energies, with same function but if fitting parameters of different data-set are random distributed and don't follow the trend of theory, the curves could fit the data but the parameters could not be trustworthy.

In this case the fitting parameter are:

1) τ that assumes the same value for all curves,
2) $K_{Vis}\beta_{32}p_2\, n_3^e(0)$ that increases if energy increases but should be an expected control because it is a multiplicative factor and it is obvious that increases if energy increases,
3) $\gamma n_3^e(0)$ that increases if energy increases but because it regards the decay speedy and not only the intensity it could be a good feedback.

In figure 5.8 is shown the $\gamma n_3^e(0)$ parameter estimated for different laser energies, the trend is rising but slower than linear as anticipated by the theory.

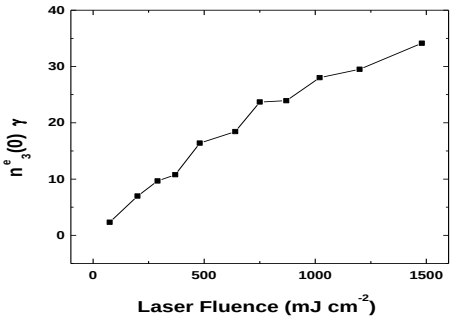

Figure 5.8. The figure shows the estimated parameter $\gamma n_3^e(0)$ for all curves obtained at different laser energies. This parameter is proportional to excited states density at t=0 so the under linear increasing behavior is consistent with model.

On this sample were performed also time resolved measurements on exciton peak.

The function that should fit the decay is:

$$\varphi^{UV}(t) = \frac{K_{UV}\beta_{31}\,\beta_{32}\,p_2\,n_3^0}{\beta_{21}\;n_2^0}\; n_3^e(0)\left\{\frac{\frac{n_3^e(0)}{n_3^0}\,exp\left(-\frac{2t}{\tau}\right)}{\left[1+\;\gamma n_3^e(0)\left(1-exp\left(-\frac{t}{\tau}\right)\right)\right]^2}+\frac{exp\left(-\frac{t}{\tau}\right)}{1+\;\gamma n_3^e(0)\left(1-exp\left(-\frac{t}{\tau}\right)\right)}\right\}$$

It is a very intricate function with too much parameters, it surely fits well the data but the values of parameters could not be trustworthy.

Expanding to first order the expression of $n_3^e(t)$, inserting it in expression for $\varphi^{UV}(t)$ and neglecting the linear term in $n_3^e(0)$ (this is possible for short time and high energy) we have:

$$\varphi^{UV}(t) \approx \frac{K_{UV}\beta_{31}\,\beta_{32}\,p_2}{\beta_{21}\;n_2^0}\left(\frac{n_3^e(0)^2}{\left(1+\;n_3^e(0)\gamma\frac{t}{\tau}\right)^2}\right)$$

That is a good approximation for high pump energy.

The measurements on exciton peak were performed using 2ns range (high resolution) and performing a jitter correction, the decays were acquired for different laser energy.

On each curve was performed a fitting procedure using the short time approximate form of $\varphi^{UV}(t)$. Some measures with corresponding fitting curves are shown in figure 5.9.

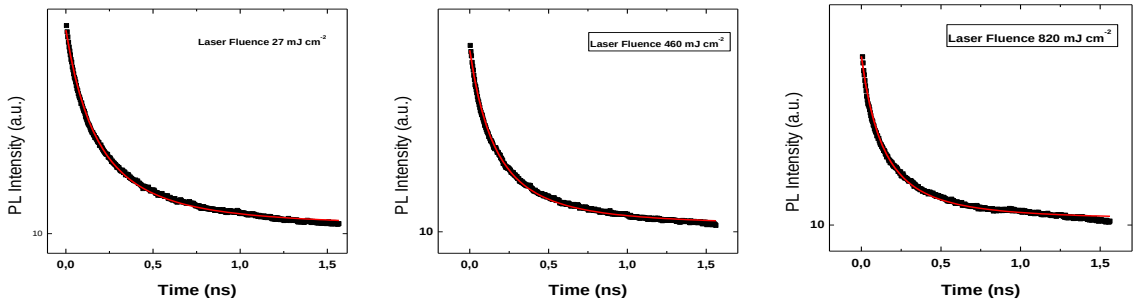

Figure 5.9. In figure are showed three decays integrated between 363 and 393 nm for different laser fluencies and the corresponding fitting function describing the UV PL temporal behavior obtained by three bands model.

To obtain a control on fitting curves we show the estimated parameter $\frac{n_3^e(0)\gamma}{\tau}$ for all decays as fluency function (figure 5.10), the values of parameter increases when energy increases as predicted by the model. Unlikely the decay lifetimes of UV emission and visible emission are not equal to each other so the system is not describable using a simple three bands model because the experimental results contradict model prediction.

So the mechanism is more sophisticated (for example could be needful other recombination channels). What is certain is that impurities are not excited using under gap radiation but only by UV radiation or by excited electrons in conduction band.

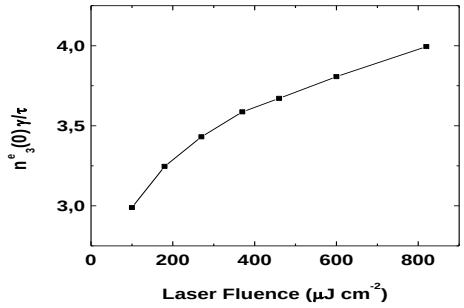

Figure 5.10. The figure shows the estimated parameter $\gamma n_3^e(0)/\tau$ for all curves obtained at different laser energies. This parameter is proportional to excited states density at t=0 divided by τ so the under linear increasing behavior is consistent with model.

The dynamic depends on laser fluence used to excite the sample especially for UV emission, in following paragraphs will be showed some time resolved measurements in several injection regimes both visible and UV, moreover will be showed what results is possible to obtain by these measures and if is possible to obtain stimulated emission effects.

The UV luminescence, due to exciton spontaneous emission and to exciton-exciton scattering (p-line that is not visible in bulk crystal as will be showed in next chapter), shows an amplified spontaneous emission (ASE) confirmed by at least three experimental results: fast decreasing of recombination time, spectral FWHM, and typical integrated intensity ASE behavior as pump energy increases. Moreover a peak red-shift was observed increasing laser energy and the same effect was observed on bulk crystal (next chapter).

The ZnO spectrum, as showed in previous paragraph, exhibits also a visible luminescence due to intragap states which origin is misunderstood, moreover the estimation of intragap states density is a nontrivial problem because they don't contribute to conductivity so they are not measurable by means of electrical measurements. One of the aims of this work is to study the electrons recombination dynamic by means these states and if they affect the stimulated emission processes to some extent.

5.4 Visible emission in nanowires

The visible and UV PL were studied for two new samples of nanowires.

The figure 5.11 shows two spectra using HeCd and Nd YAG as pump, the UV/visible intensity ratio is four order of magnitude lower when HeCd instead Nd:YAG laser is used, moreover the visible component shows the peak at 530 nm when the sample is excited using HeCd laser (or lamp) and it moves to 500nm when excitation is carried out by Nd YAG laser.

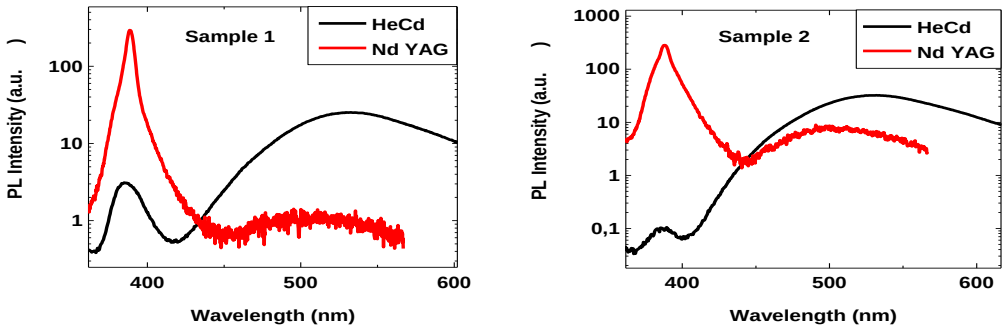

Figure 5.11. *In the figures the PL spectra are showed using both HeCd and Nd:YAG laser for two samples of nanowires. The ratio between UV and visible is larger when Nd:YAG is used. Moreover the maximum of visible peak is centered at 530nm when the excitation is done using HeCd and it shifts to 500nm when Nd:YAG is used.*

The variation of ratio and peak position depends on pump power because several spectra using different wavelength selected by a lamp were collected and there wasn't any spectrum change

confirming they don't depend on excitation wavelength. The change is due to different powers of sources that excite deep states to different extent.

To excite these intragap states is needful pump achieves a photon energy higher then energy gap. Radiation with same photon energy of visible emission doesn't excite these states (as seen in paragraph 5.1). There are two possible reasons of UV/visible ratio change as pump energy increases: 1) the states generating visible luminescence are less than UV states so when excitation intensity increases enough, to populate UV states is simpler then to populate visible states with a consequent enhancement of UV luminescence compared with visible luminescence.

2) the presence of adsorbed oxygen that bends the bands [24] and generates an electric field that dissociates the exciton. When the e-h pairs concentration is large (high pump energy) the UV luminescence increases because the screening diminishes region length where is electric field.

So UV luminescence in high e-h pairs density condition is very stronger than UV luminescence in low e-h density condition (not in a proportional way) resulting in an illumination enhanced PL effect in ZnO [29].

To investigate the behavior of visible states we performed time resolved measurements on green component of spectrum (~460nm-550nm) at different pump energies on two samples of nanowires.

In figure 5.12 four decays collected for different excitation fluencies are shown with corresponding fitting function (biexponential).

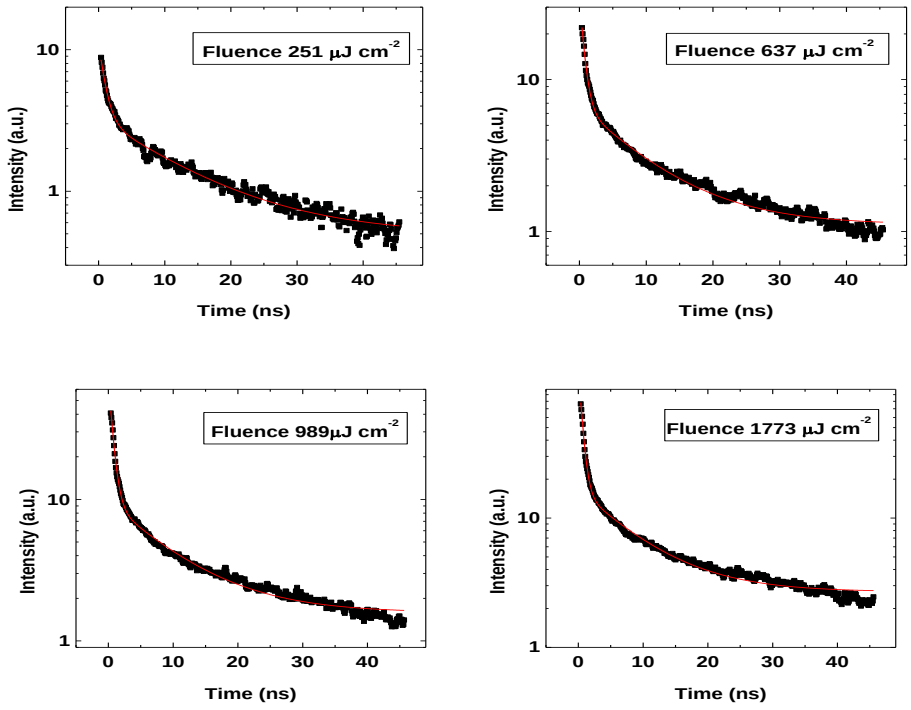

Figure 5.12. *In the figures are showed four decays integrated between 460 and 560nm for different laser fluencies and the corresponding fitting function. The fitting function utilized are biexponential functions.*

The decays show two different slopes, when the pulse energy is decreased as much as possible two slopes behavior is still observable and it's impossible to decrease the laser energy in way that the decay is well fitted by a single exponential function. Two case are possible: 1) the dynamic is bimolecular but it is impossible to observe the unimolecular regime (that is the low energy limit of bimolecular dynamic) because an energy too low for this laser repetition rate should be needful 2) the visible luminescence is originated by two different kinds of states with different decay lifetimes and with overlapping (at least partly) wavelength emission.

We have performed the fit with a biexponential function:

$$I_{Vis} = A_1 \exp\left(\frac{t}{\tau_1}\right) + A_2 \exp\left(\frac{t}{\tau_2}\right)$$

Plotting the estimated parameters (A_1, A_2) as pump energy function (figure 5.13) we can see that A_1 increases faster than A_2 so, extrapolating value of A_1 and A_2 in fluence $\rightarrow 0$ condition, the value of A_1 should be negligible respect on value of A_2 and unimolecular regime exists but it's impossible to observe it using these laser fluencies (case 1). It can be also due to different excitation cross sections of two possible kinds of states, in this case in low fluency limit only one set of states is excited justifying the single exponential behavior (case 2).

However in both previous case it's obvious that the decay curves when t>10ns are single exponential functions which τ is about 10ns .

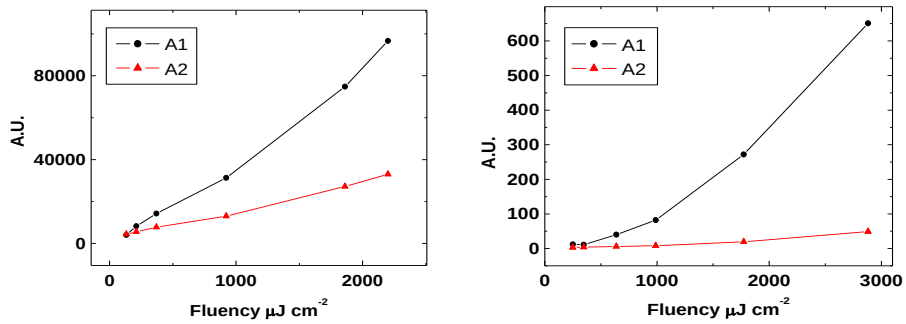

Sample 1 Sample 2

Figure 5.13. *In figure are showed the amplitudes A_1 and A_2 of biexponential functions obtained fitting the decays for different laser fluencies, both parameters increases as laser fluencies increases but the rise of A_1 is higher than A_2. Then extrapolating the values of A_1 and A_2 in fluency $\rightarrow$ 0 condition, the value of A_1 should be negligible respect on value of A_2 .*

Looking at PLE results (figure 5.2), the visible states are probably not excited by photons, but they are excited by conduction band electrons excited by laser pump. The time needful to conduction band electrons to excite visible states is very small because this energy transfer occurs by means of

phonons collisions or electron-electron collisions. This statement can be confirmed by simultaneous time resolved measurement of visible luminescence and laser pulse, observing that time delay between laser pulse and visible luminescence is smaller than time resolution of apparatus.

After excitation, part of excited conduction band electrons will form exciton in a time $\tau_{cond\rightarrow ex}$ larger than some ps (to $\tau_{cond\rightarrow ex}$ must be given the same meaning given to band to band transition (bimolecular dynamic)) [47] and a part will excite intragap states in a time lower than about 1ps because of phonon scattering. The rate of deep states excitation VIS_{rate} is proportional to $N_{cond}^{occupied}\tau_{cond\rightarrow vis}N_{vis}^{empty}$ where $N_{cond}^{occupied}$ is the density of occupied conduction band states $\tau_{cond\rightarrow vis}$ is the inverse of coupling constant between conduction band and visible states and N_{vis}^{empty} is the density of unexcited deep states. The rate of exciton formation ex_{rate} is proportional to $N_{cond}^{occupied}\tau_{cond\rightarrow ex}N_{ex}^{empty}$ where $\tau_{cond\rightarrow ex}$ is the formation time of exciton and N_{ex}^{empty} is the density of empty exciton states. So when excitation is performed using continuous HeCd laser or lamp (low power) because of $\tau_{cond\rightarrow vis} \ll \tau_{cond\rightarrow ex}$, VIS_{rate} is bigger than ex_{rate} and the visible luminescence is stronger than UV luminescence or at least the density of deep excited states is larger than number of excitons.

When excitation is performed with Nd:YAG laser, that excites a large number of electrons, the term N_{vis}^{empty} in vis_{rate} is decreased in comparison with N_{ex}^{empty} in ex_{rate} expression (because $\tau_{cond\rightarrow vis} \ll \tau cond\rightarrow ex$) and the visibile/UV ratio decreases.

The previous reason of Vis/UV variation doesn't void the aforementioned explanation of Wang and Seo [24] but the Vis/UV change can be due to the contributions of two effects.

Moreover, using HeCd as excitation source, the visible region shows a peak centered at 530nm (figure 5.11) this peak shifts to 500 nm when Nd:YAG is used (figure 5.11) it means the power that fulfils a density of visible occupied states of order of total number of visible states is obtained with power larger than HeCd laser but lower than lowest power used of Nd:YAG laser, when Nd:YAG laser is used, $N_{vis}^{occupied}$ is the same order of magnitude of $N_{vis}^{occupied} + N_{vis}^{empty}$. These kind of consideration may be a starting point to measure density of intragap states that is impossible to measure in electrical way.

5.5 UV emission in nanowires

Also TRPL measurements on UV part of spectrum have been performed to understand if these samples show amplified spontaneous emission (ASE) processes and what is the recombination dynamic of these states in different injection regimes.

We can see by figure 5.13 that UV emission, when excited at low laser power, is centered at 385 nm and is due to spontaneous emission [37]. When pump power increases, the wavelength of peak position experiences a red shift.

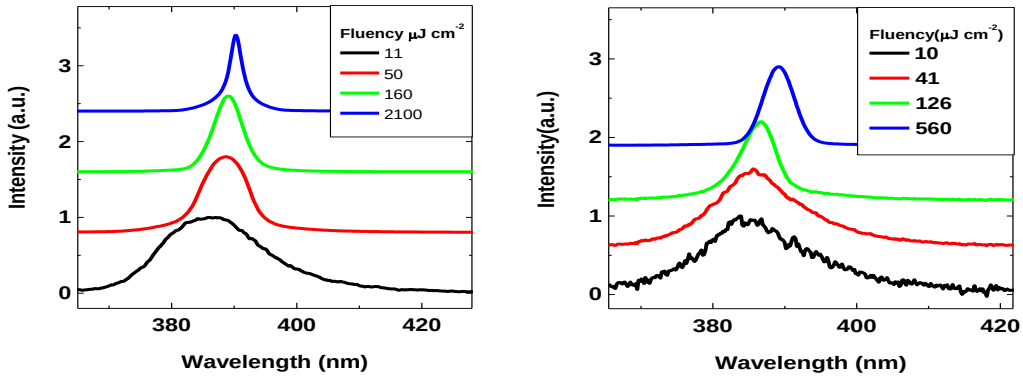

Figure 5.14. *Four normalized spectra of UV emission are showed for two nanowires samples. The FWHM of peaks decreases as pump fluencies increases, it is an evidence of stimulated emission process and doesn't occur in bulk sample as will be showed in next chapter.*

The principal feature in figure 5.14 is the FWHM decreasing when pump energy increases and this is a strong evidence of an ASE process [37] as confirmed also next by other experimental evidences. The radiation emitted in stimulated way is emitted along nanowires axis [38], because of random distribution of nanowires it is impossible to observe regular cavity mode [37].

The ASE peak, centered at 390 nm (3.18 eV), is due to p-line as explained in paragraph 1.7.

The time of exciton formation is larger than 3-4ps [47]. Time resolved measurement of emitted radiation and laser pulse at same time are showed in figure 5.15 for low, intermediate and high Nd:YAG powers. We can see that when the laser power is low, the decay starts about 20ps after excitation conversely for high power the pulse and decay start at the same time (below setup resolution), confirming the presence of ASE process for p-line. The time reduction of decay onset is due to increase of exciton density that increases the scattering probability. This phenomenon is not observed in ZnO bulk crystal excited using these pump powers as it can be observed by figure 5.15b where the same measurement of figure 5.15a is showed but performed on bulk crystal.

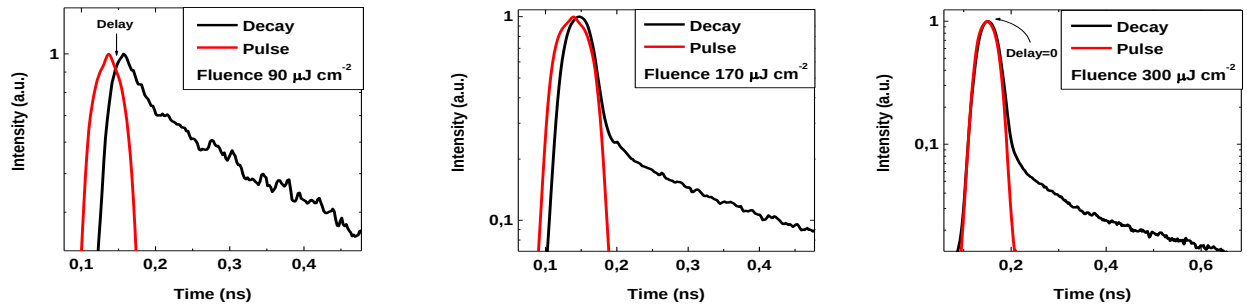

a) Nanowires

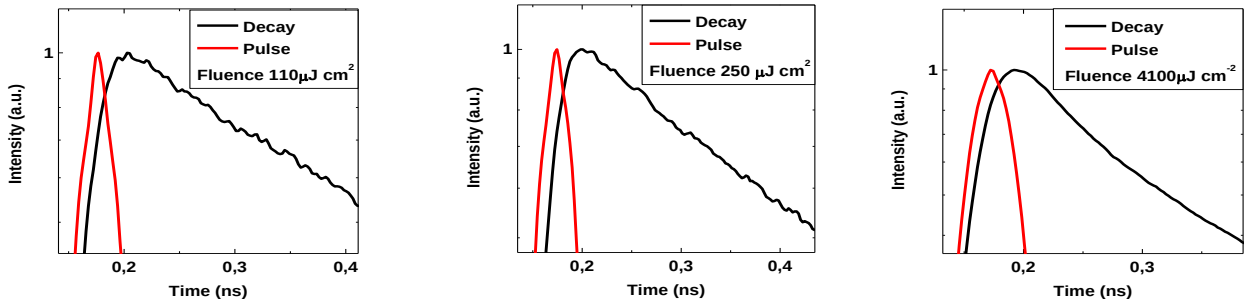

b) Bulk crystal

Figure 5.15. *The first three pictures show the laser pulse and the decay integrated between 363 and 393 nm acquired on nanowires instead on bulk crystal the other three pictures. The delay between laser pulse and decay decreases in nanowires as laser energy increases and is constant for bulk confirming that stimulated emission occurs in nanowires.*

The total energy of decay and the intensity at decay onset, both integrated between 363 nm and 403 nm, are plotted in figure 5.16, for two sample. We can see that, after a first part where the behavior is almost linear, when the fluency is about 10 µJ cm^{-2} the curves start to grow in superlinear way and it is a typical behavior of ASE process [38].

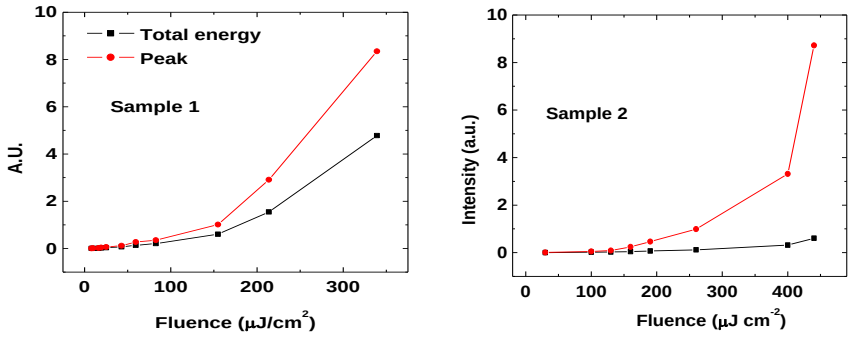

Figure 5.16. The figure shows the total emitted intensities (black points) and peak intensities (red points) of two nanowires samples as function of laser fluencies. The superlinear behavior of these quantities is an indication of stimulated emission.

The decay behavior strictly depends on rate equations involved in to the process and it depends on injection level. For visible luminescence was impossible to separate the different injection regimes but in this case we can use a bimolecular equation for carrier recombination generating UV emission that produces (eq. 2.1) the following temporal behavior for luminescence intensity.

$$I_{PL}(t) = K\left\{ rN_D \frac{\Delta p_0 exp\left(-\frac{t}{\tau}\right)}{1+\frac{\Delta p_0}{N_D}\left(1-exp\left(-\frac{t}{\tau}\right)\right)} + r\left[\frac{\Delta p_0 exp\left(-\frac{t}{\tau}\right)}{1+\frac{\Delta p_0}{N_D}\left(1-exp\left(-\frac{t}{\tau}\right)\right)}\right]^2\right\}$$

Previous equation are valid in constant quantum efficiency approximation so when stimulated emission regime starts they are no longer valid.

$I_{PL}(t)$ is approximated by an hyperbole in high injection regime (high pump energy and $t < \tau$) and it is approximated by a single exponential function in low injection regime (low energy for all time or high energy for $t >> \tau$). In ZnO oxide bulk crystal these two recombination dynamics are observed in a wide fluency range (as will be showed in next chapter) instead in this case the single exponential behavior is observed (unimolecular dynamic) but, because of ASE process (in nanowires), it's possible to observe the bimolecular dynamic only in a narrow fluencies region. In fact, when the fluency exceeds the threshold, the characteristic decay time decreases quickly and the recombination dynamic is no longer described by the previous equation.

In figure 5.17 are showed three decay: one in unimolecular regime, one in bimolecular regime and the third one when ASE appears.

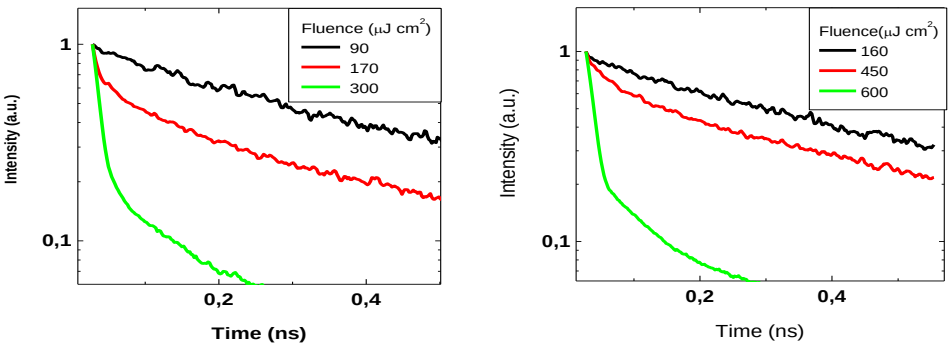

Figure 5.17. *In the pictures are showed the UV decay (between 363 and 393nm) in three different injection conditions for two samples of nanowires. The black curve represents the unimolecular regime, the red one the bimolecular regime and the green curve the stimulated emission in which the lifetime becomes very small.*

Some images, collected on the streak camera's CCD, are showed for different fluencies (figure 5.18). It can be noted that the peak narrows on horizontal axis (photon energy) and vertical axis (time) as fluence increases . Moreover we can see, by zoom of intermediate injection level figure (where both exciton and p-linen are present), that emission at wavelength of black spot (p-line) starts and decays faster than wavelength region on the right of p-line.

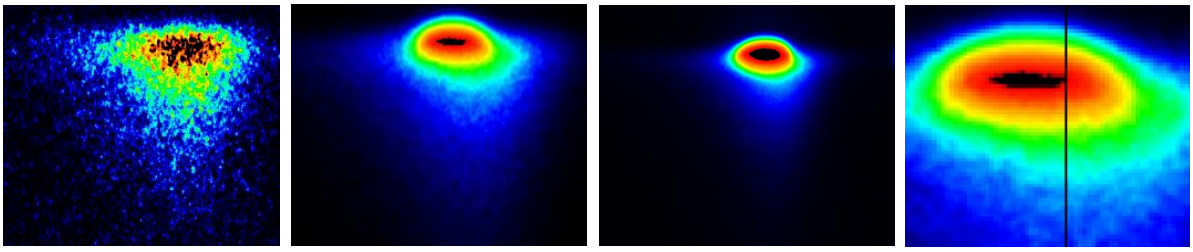

Figure 5.18. CCD images for three different injection levels (160 μJ cm^{-2}, 450 μJ cm^{-2}, 600 μJ cm^{-2}). In the first three figures are showed the CCD false color image of decays in different injection conditions time resolved (along vertical axis) and wavelength resolved (along horizontal axis). It is possible to see that when the laser fluence increases the lifetime decreases and FWHM of spectrum gets smaller. The fourth image is a zoom of the second picture and is possible to see that the speed of decay is not constant for all spectral components but in the left part of picture, where is the p-line, the decay is faster indicating that stimulated emission is due to exciton p-line.

The UV peak positions doesn't shift between HeCd and lowest power of NdYAG but it shifts between low power and high power of NdYAG. When the laser energy is large enough that the recombination dynamic is in stimulated emission regime due to p-line, the visible states don't affect the UV emission because (further decreasing N_{vis}^{empty}) p-line emission is obtained immediately and the waiting to empty the UV states is no more and UV decay follows faithfully laser shape while the visible state are completely occupied and due long lifetime they remain filled during laser pulse.

Chapter 6

ZnO Bulk

In this chapter will be shown some experimental results regarding emission properties of ZnO bulk crystal and will be underlined the difference with ZnO nanowires.

In the ZnO applications as light emitter, to have optical gain, an high injection density usually have to be induced and so a ZnO properties comprehension in such conditions is demanded.

For example, non-radiative recombination processes which may become predominant at high injection rates, such as Auger processes, may quench the stimulated emission processes and thus inhibit the lasing action. So, in the first paragraph, an analysis of the effects induced by high excited carrier density will be carried out.

In the second part will be used TRPL measurement as an useful tool in order to gain insight in the issue of charge recombination in ZnO and to obtain a quantitative outline of ZnO excitonic dynamics.

Furthermore TRPL, which is the standard technique to investigate recombination dynamics, is very often employed as a characterization tool testing material quality and device performance, as the value of exciton lifetime is indicative of the crystalline quality (lifetime becomes longer as the quality increases). However, such characterization-oriented approach requires attention as, in general, the lifetime itself is not a well-defined constant quantity but it depends on excitation

density. Moreover, decay functions routinely used to extract lifetimes (such as biexponentials) may just represent a phenomenological tool not reflecting the overall recombination dynamics. Far from representing a mere extension of static PL analysis, TRPL studies may give much more than simple qualitative indications, once the experimental results are analyzed in the framework of a reasonable recombination model. Such ideas are the basic inspiration of the second part of chapter, whose goal is to generalize the concept of t_{eff} exposed in second chapter when also non-radiative recombination channels, as SHR recombination, are and evidence qualitative and quantitative aspects of recombination dynamics in ZnO by means of simple modelling and data analysis. Moreover will be shown that, for injection densities of the order of Mott density, charge recombination follows a bimolecular recombination kinetic that is well described by a "second order approximation" for total electron-hole recombination rate. The analysis, using generalized t_{eff} method, also allows determination of characterizing parameters such as unimolecular lifetime and bimolecular coefficient, as well as estimation of other parameters such as equilibrium free-carrier density N, radiative bimolecular coefficient and non radiative lifetimes.

Then will be shown the emission spectra at different time interval after excitation identifying different recombination mechanisms for different parts of spectrum and a multifitting procedure will be used to fit all curves with one function of two variables (time and laser fluency) assuming density of e-h pairs proportional to laser fluency.

Afterward an analysis of annealing effects on emission properties of ZnO bulk crystal will be performed comparing some measures carried out on crystal before and after oxygen annealing.

In the last paragraph will be shown a possible extension of multifitting procedure at fluency values where non-linear absorption phenomena occur but it is not ultimate and some improvement are needful.

6.1 High injection effects

A representative example of TIPL spectra in the UV region obtained at different conditions of optical injection is reported in figure 6.1.

The PL spectrum of curve (a) was acquired under CW He-Cd laser excitation, which gives rise to a stationary electron-hole density much smaller than typical ones obtained by pulsed laser excitation. The PL spectra obtained by picosecond laser excitation are shown in curves from (b) to (f) for different values of excitation fluency. In all investigated samples, no significant shift of the PL peak

was noticed for excitation fluencies of the order of few microjoules per square centimetres (cfr. curve (b) of figure 6.1), while a red-shift of excitonic emission is clearly observed at increasing fluency.

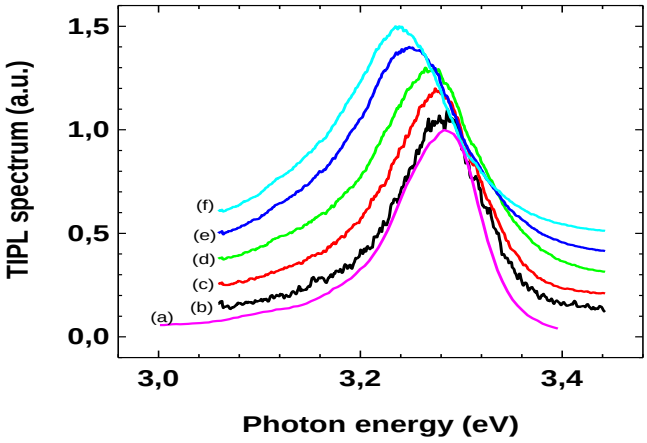

Figure 6.1. *Time-integrated normalized PL spectra obtained at different conditions of optical injections. Curve (a) corresponds to CW excitation (HeCd laser). Other curves correspond to Nd:YAG excitation at optical excitation fluencies (absorbed energy divided by excitation area) of (b)10 μJcm^{-2}, (c): 50 μJcm^{-2}, (d): 276 μJcm^{-2} , (e): 1190 μJcm^{-2}, (f): 1940 μJcm^{-2}. The curves have been vertically shifted for more clarity.*

The maximum shift of emission energy observed in the investigated range of optical pumping was about 50 meV (figure 6.2), leading to a PL emission peak of 3.24 eV at 1940 μJcm^{-2} excitation fluency. Such shift is not large enough to infer activation of "p-line" exciton-exciton scattering, which gives rise to emission peaked at 3.18 eV [35], nor to infer the complete exciton dissociation due to screening of Coulomb potential by electron-hole plasma [34], which leads to emission peaked at 3.1 eV [35].

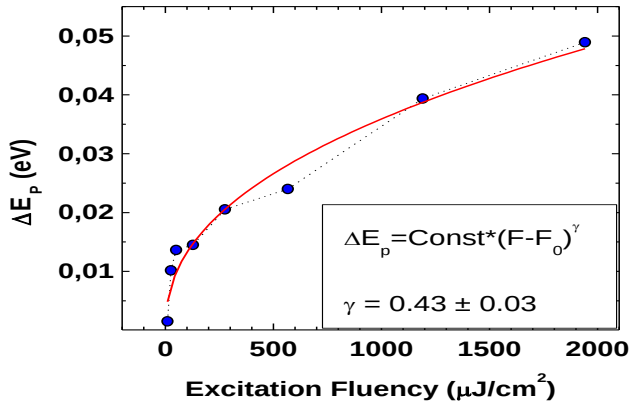

Figure 6.2. *Experimental shift of UV photoluminescence peak energy as a function of excitation fluency. The data refer to the* same *set of measurements giving the PL spectra reported in fig.6. 1. The full curve is a fit of the data points using Eq.(6.1) which is also reported in the inset.*

The values of emission shifts are instead compatible with those characterizing band-gap narrowing due to electron-electron and hole-hole exchange interactions as explained in paragraph 2.11. Excitonic emission spectra of figure 6.1 shift toward red while retaining the overall shape and width, thus suggesting that for investigated fluencies excitons retain their individual character, while the red shift of their absolute energy results from a bandgap narrowing. In figure 6.2 the shift of emission peak energy ΔE_p is reported as a function of excitation (reflection corrected) laser fluency. A good empirical fitting vs. excitation fluency is provided by an empirical power law as follows:

$$\Delta E_p = A*(F-F_0)^{\gamma} \qquad (6.1)$$

where ΔE_p is the shift expressed in eV, F is the optical fluency and A is a proportionality constant, this expression was used by Lu and coworkers [31] that shown such empirical behaviour fits with the experimental bandgap narrowing in Al doped ZnO (Al:ZnO) films. It is to be noted that the empirical relation expresses the energy shift as a function of excess carrier density and not as a function of optical fluency. In principle, these two latter quantities are not trivially proportional. However, it is also to be noted that the value $\gamma = 0.44 \pm 0.01$ found for data in figure 6.2 is quite close to the one $\gamma = 0.40$ reported by Lu et coworkers for Al:ZnO [31]. This result is of interest for the issue of determination of free carrier density, which we discuss now.

In the case of high injection regimes (as our case), it is not easy to obtain a well-definite determination of injected free carrier density (indicated as ρ_0) once excitation fluency is known. A rough estimation of a spatially uniform photo-injected free carrier density can be given by

$$\rho_0 = \frac{\alpha\left(\frac{E}{S}, \nu\right) E(1-R)}{Sh\nu}$$

as explained in paragraph 2.8. The α dependence on pump energy considers an eventual presence of nonlinear absorption effects such as band filling or thermal effects.

Furthermore, direct measurement of absorption coefficient was not possible on our optically thick films (as already cited above). For linear absorption coefficient at 355 nm wavelength, a reference value of $\alpha = 1.5*10^5$ cm^{-1} can be taken from optical transmittance analysis, by Muth and coworkers [48], of single-crystal epitaxial ZnO films grown on sapphire.

To verify if non-linear absorption happens, some reflectance measurements were performed on all samples at different pump intensity, reflectance measure on one sample is shown in figure 6.3 (the

measures on the other samples are equal to each other). Non linear phenomena on reflectance data are not observed so, very likely, at these fluencies non-linear absorption doesn't occur.

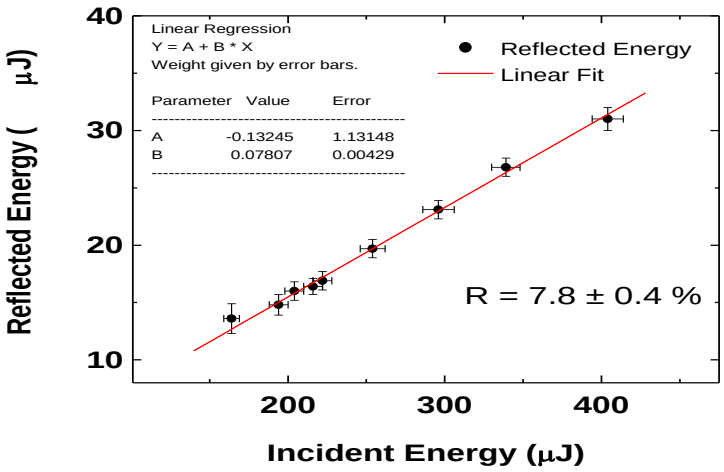

Figure 6.3. *The figures shows the laser pulse reflected intensity by ZnO crystal as function of laser pulse energy. The beam used was the third harmonic of Nd:YAG that was focalised on the sample at 45 degrees. The behaviour is linear so the reflectivity doesn't depend on pulse energy then the non linear absorption phenomena are absent.*

Moreover it is worth underlining the similarity between the γ value (0.44) obtained fitting data with Eq. (6.1) and the one (0.40) reported by Lu [31], indicating that the ΔE_P vs fluency scales approximately with the same rate as vs. the free-carrier concentrations and thus suggesting again negligible nonlinear absorption. However, due to the lack of quantitative literature reference on single-crystal ZnO nonlinear absorption, the issue remains open and further work has to be performed to define optically injected carrier density at a precise quantitative level. Therefore, it is all the same helpful to use the expression $\rho_0 = \frac{\alpha E(1-R)}{Sh\nu}$ in order to estimate the optically injected electron-hole concentrations, recalling that they should be considered as reference values.

Using α =1.5*10^5 cm^{-1} [48], one gets a photo-injected electron-hole concentration of 2*10^{18} cm^{-3} for curve (b), while for curves (d), (e) and (f) the estimations give 5.5*10^{19} cm^{-3} , 2.4*10^{20} cm^{-3} and 3.9*10^{20} cm^{-3}. It is to underline that, regardless the estimation of ρ_0, the results indicate that effects related to photo-injection of carriers become important at excitation fluency of the order of 100 μJ/cm^2 and above, suggesting that photo-injected carrier density is larger than (or is at least comparable to) the density of equilibrium free-carriers N in such range of optical injection, which was thus also explored by TRPL analysis.

6.2 Generalization of τ_{eff}

In excited wide gap semiconductor, although direct bandgap semiconductor, because of states lying in the forbidden gap, recombination are not only radiative but they occur also in other way as explained in paragraph 2.9.

Band to band recombination due only to phonons is very improbable then the intragap states act as recombination centers by means of SHR recombination mechanism. If the excitation is not too large so it's possible to neglect Auger effect, the SRH recombination are the only processes affecting quantum efficiency.

In this paragraph will be shown a generalization of τ_{eff} method (see chapter 2) when quantum efficiency (η) is not constant considering only SRH processes as non radiative recombinations. Moreover a second order approximation of SHR recombination is used to allow that equations were resolved in analytical way.

After laser pulse excitation, the system recovers to equilibrium through recombination of excess carriers density, whose time evolution will be dictated by a rate equation of the form $W = -\frac{d\rho}{dt}$, which defines the total recombination rate W as the number of recombination per unit time and volume. Indicating W_R and W_{NR} the radiative and non-radiative recombination rates respectively (of course $W=W_R+W_{NR}$) the TRPL kinetics can be interpreted by the presence of linear and quadratic term in the expression of W versus ρ. Both terms are obviously present in the standard expression of electron-hole radiative recombination rate:

$$W_R = -\frac{d\rho}{dt} = BN\rho + B\rho^2 \qquad (6.2)$$

where B is the radiative bimolecular coefficient. As W_R quantifies the emitted photon flux per unit volume, the TRPL yield $I_{PL}(t)$ can be taken as proportional to W_R using as $\rho(t)$ the solution of the (total) rate equation.

In the following the discussion proceeds by neglecting Auger processes and all other terms of the order of ρ^3 (and higher powers) in the total recombination rate, showing that the analysis can be simplified while still retaining the peculiar features of experimental results described afterward.

In the framework of such "second-order approximation" the excess carrier density kinetics is described by:

$$W = -\frac{d\rho}{dt} = \frac{\rho}{\tau} + b\rho^2 \qquad (6.3)$$

where both radiative and non radiative (SRH) recombination contribute to terms $1/\tau$ and b.
The W_{SRH} rate and its second-order expression in the case of recombination centers positioned near middle-gap with a density N_t, are given by (see paragraph 2.9):

$$W_{SRH} = \frac{\rho N+\rho^2}{\tau_{min}(N+\rho)+\tau_{maj}\rho} = \frac{\rho}{\tau_{min}} - \frac{\tau_{maj}}{\tau_{min}^2}\frac{\rho^2}{N} \qquad (6.4)$$

As in paragraph 2.8 we have:

$$\frac{1}{\tau_{eff}(t)} \equiv -\frac{\frac{dI_{PL}(t)}{dt}}{I_{PL}(t)} = \frac{BN+2B\rho}{BN\rho+B\rho^2}\frac{d\rho}{dt}(t) = \frac{N+2\rho}{N\rho+\rho^2}\frac{d\rho}{dt}(t)$$

But now taking into account also non radiative effects with simple calculation we have:

$$\frac{1}{\tau_{eff}}(t) = \left(1/\tau + b\rho(t)\right)\frac{N+2\rho(t)}{N+\rho(t)}$$

that at t = 0 the expression becomes:

$$\frac{1}{\tau_{eff}}(0) = \left(1/\tau + b\rho(0)\right)\frac{N+2\rho(0)}{N+\rho(0)} \qquad (6.5)$$

In the limit case of only radiative processes ($1/\tau = BN$ and b = B) we have the same expression of paragraph 2.8. Determining the experimental initial effective lifetimes by numerical derivative of TRPL signals, the values of b, τ and N can be obtained by data fitting using function (6.5) (figure 6.5).

It is worth noting that the non-linear dependence of data points (figure 6.5) vs. optical fluency is an indication that the N quantity is comparable, larger or smaller than $\rho(0)$ (if $N << \rho(0)$ or $N >> \rho(0)$, eq.(6.5) would imply a linear behavior of $1/t_{eff}(0)$ vs optical fluency (with two different slope).
It's important to underline function (6.5) shows a weak dependence on N parameter that implies a large uncertainty on N estimation.
Considering the second-order W_{SRH} rate (Eq. (6.4)) and W_R rate (Eq.(6.2)), the following relations can be obtained:

$$bN = BN - \frac{\tau_{maj}}{\tau_{min}^2} \qquad \frac{1}{\tau} = BN + \frac{1}{\tau_{min}} \qquad (6.6)$$

If the τ_{maj}/τ_{min} ratio was known, the eqs (6.6) allows to obtain an estimation for the radiative bimolecular coefficient B and for the SRH non-radiative minority and majority lifetime from b, τ and N.

It has to be noted that such values are however affected by the uncertainties in the values of b, τ and N then independent measurements of N would therefore improve the results.

6.3 Measure of material parameters by TRPL

In figure 6.4 we report normalized TRPL curves obtained for a representative ZnO sample at different values of optical fluency. It is evidenced that different decay kinetics take place at different regimes of optical injection. For larger injection, the TRPL signal can be described as a superposition of an initial faster non-exponential decay which dominates from t = 0 to (about) t = 200 picoseconds and whose slope is fluency-dependent, followed by a regime of slower decay in which the logarithmic slope becomes approximately constant and independent on laser fluency. The same behaviour was observed in all the investigated samples. Decreasing the injection density, the fast component of TRPL signal becomes less pronounced and the signal eventually evolves towards a single-exponential curve. Such behaviour was observed in all samples and is the signature of a bimolecular recombination.

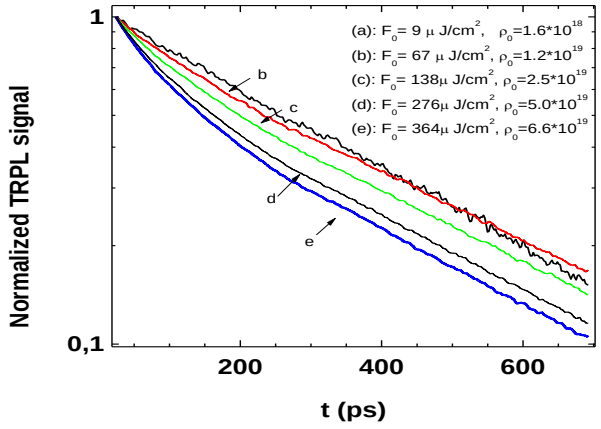

Figure 6.4. *Normalized time-resolved PL decay curves obtained for different values of laser fluency. Estimated optically-injected free carrier densities are reported in the inset.*

In our discussion, the concepts explained in paragraph 6.2 will be used.

In fact solving eq. (6.3) and substituting the solution $\rho(t)$ in eq. (6.2) we have the PL temporal behavior:

$$I_{PL}(t) = BN\frac{\rho_0 \exp\left(-\frac{t}{\tau}\right)}{1+b\tau\rho_0\left(1-\exp\left(-\frac{t}{\tau}\right)\right)} + \frac{B\rho_0^2\exp\left(-\frac{2t}{\tau}\right)}{\left(1+b\tau\rho_0\left(1-\exp\left(-\frac{t}{\tau}\right)\right)\right)^2} \qquad (6.7)$$

It can be easily seen that the above function meets the features of experimental data, as it exhibits a fluency-dependent initial slope and a fluency-independent constant slope for longer times (as for $t >> \tau$ the $I_{PL}(t)$ tends to a single exponential function).

Measurements show the existence of a transition from single exponential to bimolecular recombination kinetics once high photo-injected carrier concentration are achieved. Even if a sharp threshold for activation of bimolecular kinetics cannot be defined, the bimolecular dynamics was observed for estimated carrier concentrations of about $1*10^{19}$ cm^{-3} and greater.

Several unknown quantities appear in Eq. (6.7), thus making it hard to extract physically relevant information from fitting of experimental data, unless time-consuming multi fitting procedures are employed. Here we use the generalized "effective lifetime" τ_{eff} method shown in paragraph (6.2) in fact determining the experimental initial effective lifetimes by numerical derivative of TRPL signals, values of b, τ and N can be in principle obtained from data fitting of eq. (6.5):

$$\frac{1}{\tau_{eff}}(0) = \left({}^{1}/_{\tau} + b\rho(0)\right)\frac{N + 2\rho(0)}{N + \rho(0)}$$

once the density of photoinjected excess carrier ($\rho(0)$) is known for different optical fluencies.

In figure 6.5 the measured $\frac{1}{\tau_{eff}}(0)$ values are reported as a function of absorbed fluency for all investigated samples. The low value of $\frac{1}{\tau_{eff}}(0)$ is close to the fluency-independent logarithmic slope τ^{-1} of TRPL curves, while $\frac{1}{\tau_{eff}}(0)$ increases at increasing fluency. The values of optically injected carrier density determined through the expression $\rho(0) = \frac{\alpha(1-R)E}{S\,h\upsilon}$ are reported in units cm^{-3} on top axis of figure 6.5 for each excitation fluency. The curves in figure 6.5 represent the best fit curves, and the resulting fitting parameters are reported in Table 6.1. Notwithstanding the approximation used, it can be noticed that similar values are obtained for all (nominally identical) samples and close to typical ones of direct bandgap semiconductors such as GaAs. It has to be noted that values determined for equilibrium free carrier density N (Table 6.1) likely overestimate the real quantity because of two reasons: a) the measure is performed in a region near semiconductor surface

(~50nm), because of high absorption coefficient, where an high density of donor defect appear; b) an overestimation of fluency is made because not all the CB electron recombine by means band to band recombination so the fluency that should be used is the fluency which originates electrons that recombine by band to band transition that obviously is unknown (see next paragraph).

Further considerations can be made using the second-order expression of non-radiative SRH recombination rate eq.(6.6):

$$bN = BN - \frac{\tau_{maj}}{\tau_{min}^2}$$

$$\frac{1}{\tau} = BN + \frac{1}{\tau_{min}}$$

Assuming that $\tau_{maj} \sim \tau_{min}$ [49], determination of τ, N and b allows to obtain an estimation for the radiative bimolecular coefficient B and for the SRH non-radiative minority carrier lifetime τ_{min} by simple algebra. We obtained values of 0.8 ns (sample 1 and 2) and 0.6 ns (sample 3) for τ_{min} and $1*10^{-10}cm^{-3}$ (sample 1 and sample 3) and $0.7*10^{-10}cm^{-3}$ (sample 2) for B.

It has to be noted, as already pointed out in previous paragraph, that such parameters are however affected by uncertainties and so independent measurements of N would therefore improve the results.

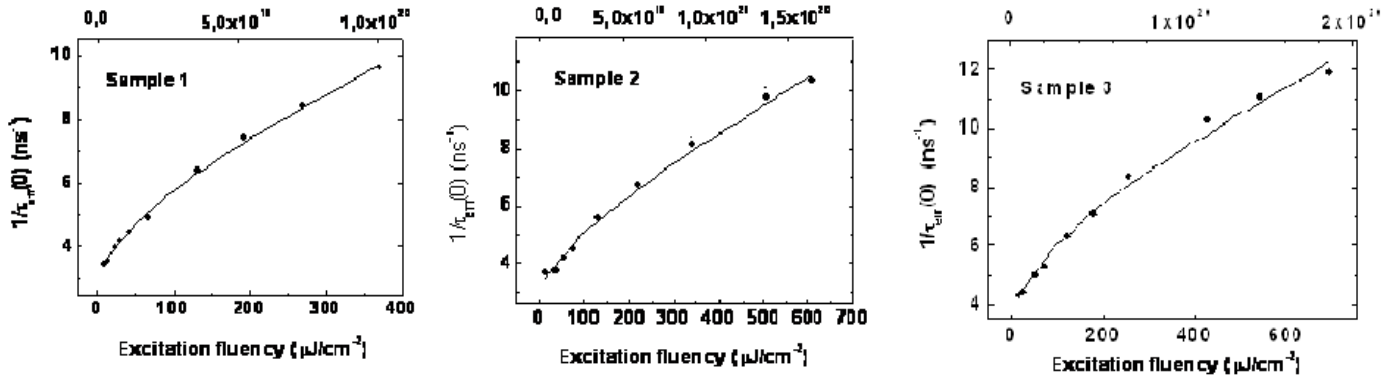

Figure 6.5. Plot of $1/\tau_{eff}(0)$ vs. excitation fluency for the three samples analyzed. Lines correspond to the best-fit curves obtained using Eq.(6.5). On top axis the estimated optically injected carrier density obtained with $\alpha = 1.5*10^5\ cm^{-1}$ and neglecting nonlinear absorption is reported.

	Sample 1	Sample 2	Sample 3
τ (ns)	0.33 ± 0.03	0.32 ± 0.03	0.27 ± 0.03
b ($cm^3\ s^{-1}$)	$(3.3 \pm 0.2)*10^{-11}$	$(2.2 \pm 0.1)*10^{-11}$	$(2.2 \pm 0.2)*10^{-11}$
N (cm^{-3})	$(1.3 \pm 0.4)*10^{19}$	$(3 \pm 1)*10^{19}$	$(2 \pm 1)*10^{19}$

Table 6.1. *Recombination constants and physical parameters as determined by effective lifetime analysis (b,t,N).*

6.4 Multi fitting procedure and competitive recombination channels

The remarks made so far consider the UV luminescence due to only one recombination channel.
In this paragraph we will see that this is not the case so performed calculation must be interpreted as a first order calculation which produces reasonable results but that could be improved.
Some spectra were acquired at different time delays after excitation pulse on other two samples of ZnO bulk crystal.
Figure 6.6 shows the spectra of two samples collected at different delays, we can see that the spectrum changes over time in particular the left part of spectrum changes and right part doesn't.
For this reason the UV luminescence is probably generated at least by two different processes, that because of inadequacy of experimental apparatus, we see as one process.

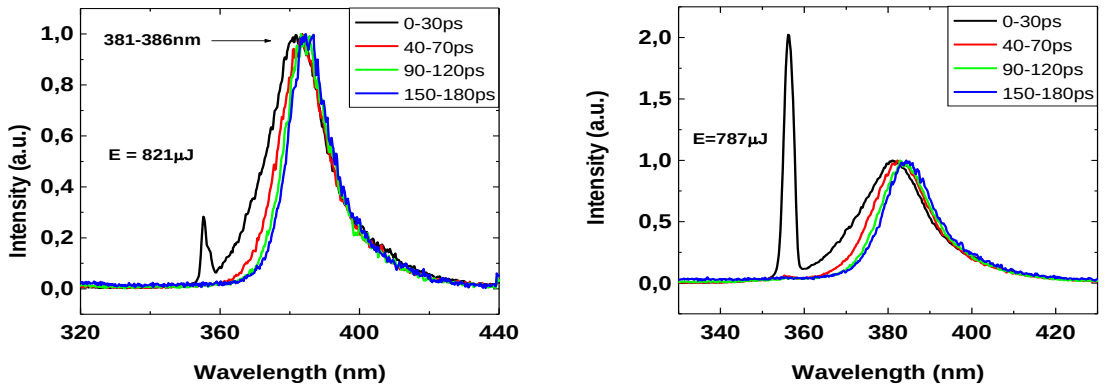

Campione 1 *Campione 2*

Figure 6.6. *In the figure are shown the normalized spectra of two samples (ZnO bulk) acquired at different time delay after excitation. The increasing of delay induces a red shift of spectrum. So the decay dynamic depend on wavelength.*

If the same measures were performed at low temperature, we should see at least two peaks, then we can select the band to band recombination peak and then to correct the previous result.
In this condition we can only select parts of image, to handle them separately and try to understand if they follow a different recombination dynamic.
By the CCD image the decays of two parts of spectrum were extracted for all used laser energy and they really behave in different way (figure 6.7).

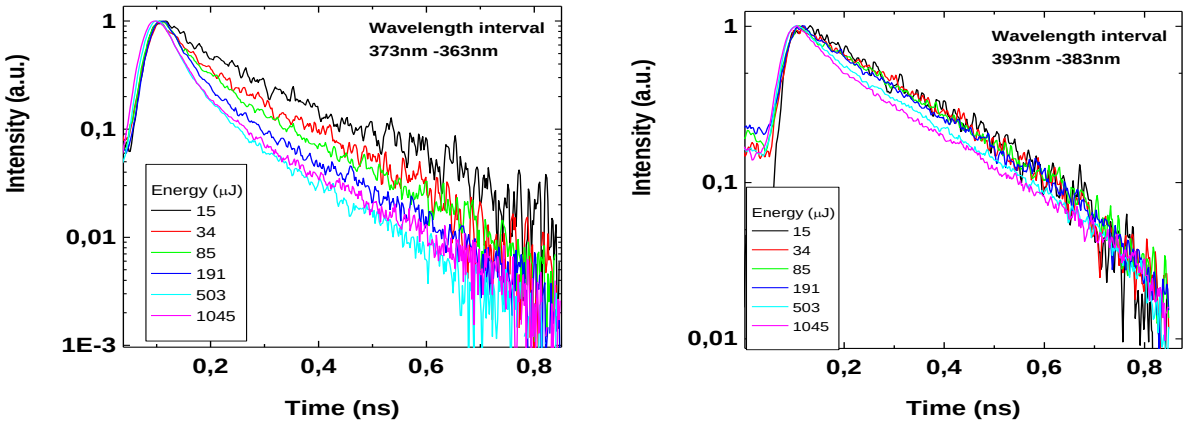

Figure 6.7. *In figure are shown the decay curves for different laser fluencies integrated between 363 and 373nm (first picture) and between 383 and 393nm (the second figure). The decay dynamic is bimolecular in the first picture and unimolecular in the second one.*

In fact the left part, centered at 368nm (arbitrary choice), has a single exponential behavior at low pump fluency and changes its slope in first instant of decay at high pump energy, this behavior is typical of a bimolecular dynamic. Instead the right part of spectrum is a single exponential for all used fluencies.
To test previous statement, a global fit was performed on all decays of left part of spectrum.
The function used is the typical bimolecular function Eq. (6.7).
The aim is the data fitting with a two variable function, the variables are time t and laser fluency F.
In the function expression the fluency doesn't appear but it's possible to introduce his dependency by means ρ_0 using the expression:

$$\rho_0 = \frac{\alpha(\nu)E(1-R)}{Sh\nu}$$

assuming negligible all non linear absorption phenomena as justified by results exposed in paragraph 6.1.
The fitting procedure was carried out using both Matlab and Minuit software. The program producing better results is Minuit and the fitting curves with corresponding experimental data are shown in figure 6.8.

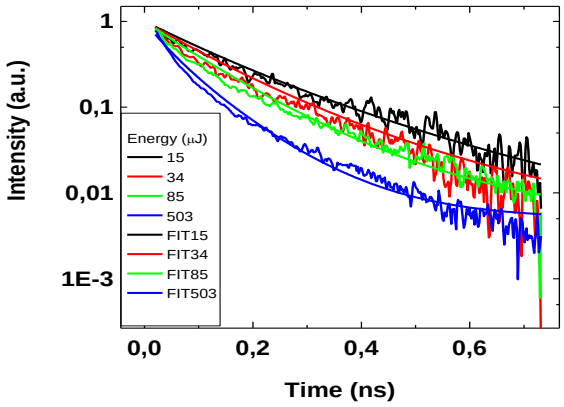

Figure 6.8. *In figure are shown the decay curves for different laser fluencies integrated between 363 and 373nm and the corresponding fit functions obtained using multifitting procedure.*

Using estimated parameters were calculated the values of b and N that are: b = 1.9 *10^{-11} cm^3 s^{-1} (sample 1) and b = 1.3 *10^{-11} cm^3 s^{-1} (sample 2), N = 8.3*10^{18} cm^{-3} (sample 1) and N = 8.5*10^{18} cm^{-3} (sample 2).

These values are the same order of magnitude of values obtained with generalized τ_{eff} method.

In this condition it's impossible to understand what is the best method but a good improvement could be made by low temperature measurements.

To understand if the laser pulse introduced incontrollable defects on samples surface that in turn changed the samples conductivity, some electrical measurements were performed.

On a ZnO sample two metallic contacts were deposed then it was linked to an electrometer (Kethley 6517A) to measure the sample resistance varying applied voltage. A Volt-Amperometric characteristic (figure 6.9) was acquired before laser irradiation and one after 10 minutes of third harmonic Nd:YAG irradiation (2mJ pulse energy).

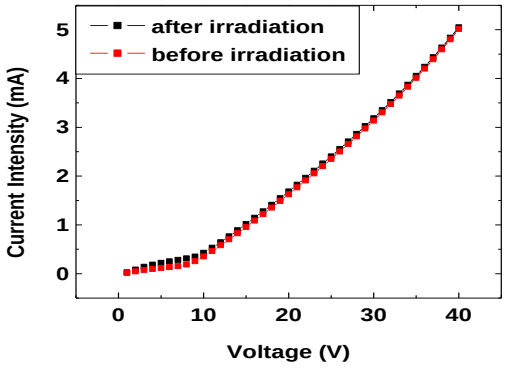

Figure 6.9. *The figure shows the voltage vs current intensity characteristic of a sample acquired before and after 10 minutes laser irradiation (355nm and 2mJ pulse energy). It is clear that irradiation doesn't change the conduction band electron density.*

By the figure it's possible to see that laser doesn't affect sample conductivity, moreover the measured resistivity is of order of some Ω/m that is a very large value for a semiconductor justifying the measured large value of conduction band electron density by TRPL.

6.5 Oxygen annealing

The models and measures performed in previous paragraphs concerned with UV emission of bulk crystal, this paragraph will deal with the effects of annealing on both UV and visible emission properties.

To investigate the origin of visible luminescence, some PL measures were carried out on samples after performed an annealing process in oxygen environment.

The sample annealing was performed by MODA Laboratory in Physics Department of Federico II University. The samples were annealed in Oxygen for 1 hour at 1350 Kelvin, this kind of process reduces the number of oxygen vacancy on sample surface.

In figure 6.10, a comparison between PLE spectra before and after annealing and a comparison of PL spectra using HeCd as pump are shown.

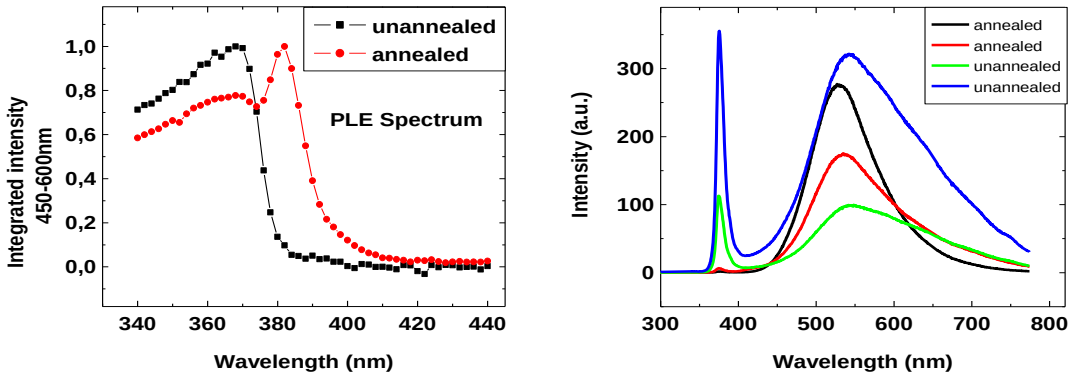

Figure 6.10. *The first picture shows the PLE spectrum of a sample before (black curve) and after oxygen annealing (red curve). The second picture shows the PL spectra of two samples before (green and blue) and after oxygen annealing (red and black curves). It is clear annealing change the visible emission band shape and ratio between UV and visible intensity.*

By PLE spectra we can see a little red shift of absorption onset. Instead by PL spectra we can see that the visible luminescence of annealed samples shows a band also in yellow region (not resolved by green band) that in unannealed samples was weaker.

Another important change regards the UV/Visible intensity ratio that is reduced after annealing, consequently the visible luminescence is not generated by oxygen vacancy. The UV/Visible change

confirms the model exposed in paragraph 1.6 that attributes the UV quenching to an electric field generated by adsorbed O^{2-} ions [27].

To understand if annealing process introduces change in recombination dynamic also TRPL measurements were performed on annealed samples.

The fitting procedure both using unimolecular and bimolecular dynamic, doesn't work on these decay curves. For these reason the function used to fit curves is a biexponential function (figure 6.11):

$$I_{PL}(t) = A_1 exp\left(-\frac{t}{\tau_1}\right) + A_2 exp\left(-\frac{t}{\tau_2}\right)$$

The estimated values of A_1 and A_2 as fluency function follow a correct behavior (linearly rising in linear absorption fluency region). Moreover τ_1 (~200ps) and τ_2 (~50ps) have the same value for all fluencies, so the biexponential function fits, at same time, all curves but the reason of this behavior introduced by annealing process is unknown.

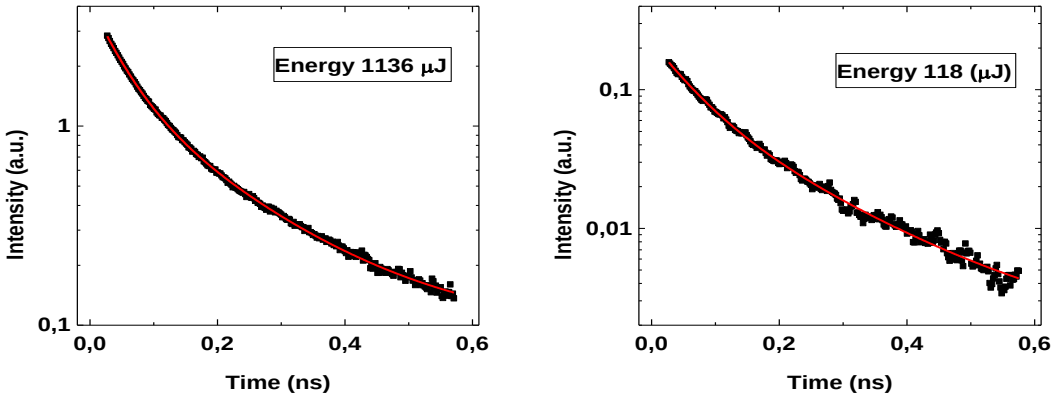

Figure 6.11. *In figure are shown two UV decays acquired at different laser fluencies on a sample after annealing in oxygen and corresponding fit curves using biexponential functions.*

6.6 Multi fitting extension

In this last part we analyze the possibility to apply the multi fitting procedure to non linear fluencies region. The PL intensity expression for bimolecular dynamic is given by Eq. (6.7):

$$I_{PL}(t) = BN\frac{\rho_0 \exp\left(-\frac{t}{\tau}\right)}{1 + b\tau\rho_0\left(1 - \exp\left(-\frac{t}{\tau}\right)\right)} + \frac{B\rho_0^2 \exp\left(-\frac{2t}{\tau}\right)}{\left(1 + b\tau\rho_0\left(1 - \exp\left(-\frac{t}{\tau}\right)\right)\right)^2}$$

The difficult to fit all curves for all laser energies is to introduce the dependence on laser energy in I_{PL} intensity using ρ_0. The quantity ρ_0 cannot be directly estimated once *E* is known due to the possible presence of nonlinear absorption effects which is expected to take place at high densities of photogenerated carriers. A direct determination (or estimation) of ρ_0 would thus require to know *a priori* the functional form of the absorption coefficient as a function of *E* that is not measurable because of sample thickness. Instead of choosing such an approach, we will use another one involving only the quantities which are directly measured in the TRPL experiments. These quantities are the decay profile of PL ($I_{PL}(t)$) and the total PL signal (time-integrated PL signal) obtained by integration of the TRPL signal over time:

$$I_{PL}^{Tot} = \int_0^\infty I_{PL}(t)\, dt$$

That produces:

$$I_{PL}^{Tot} = B\ \frac{b * \rho_0 * \tau + (b * N * \tau - 1) * \mathrm{Log}(1 + b * \rho_0 * \tau)}{b^2\, \tau}$$

This relationship between *E* and ρ_0 indicates how the generic TRPL curve $I_{PL}(t)$ can be seen as a function of time (t) and of its area (I_{PL}^{Tot}). Thus, the whole set of TRPL curves $I_{PL}(t)$ obtained at different values of laser pump energy (*E*) (and thus corresponding to different experimental values of TIPL) can be simultaneously fitted through equation (6.7) as an unique function of the two physically measured variables (t, I_{PL}^{Tot}). The major advantage of this approach is in the fact that the physically relevant quantities are obtained without absorption coefficient knowledge. On the other hand, a disadvantage exists, in fact the relationship between E and ρ_0 is transcendent, due to the presence of the logarithmic term $\mathrm{Log}(1 + b * \rho_0 * \tau)$. In other words, the relation cannot be inverted in order to express ρ_0 as a simple function of $I_{PL}^{Tot}(E)$.

However, it is easy to see that the logarithmic term $\mathrm{Log}(1 + b * \rho_0 * \tau)$ increases as a function of ρ_0 much more slowly compared to the linear term $b * \rho_0 * \tau$ and therefore the approximation $E \sim B * \rho_0/\tau$ is valid for pulse energies large enough to ensure the condition:

$$b * \rho_0 * \tau \gg (b * N * \tau - 1) * \mathrm{Log}(1 + b * \rho_0 * \tau)$$

For example in the case of ZnO visible emission the above condition is verified only for high fluencies. In fact using following value: $b = 10^{-10}$ cm^3 s^{-1} $\tau = 10^{-8}$ s $N = 2*10^{18}$ cm^{-3} the relation is verified for $\rho_0 > 4 * 10^{19}$ that correspond to fluencies larger than 250μJ cm^{-2}. To test the procedure, a global fit was performed on visible decays in very high fluencies range (figure 6.12)

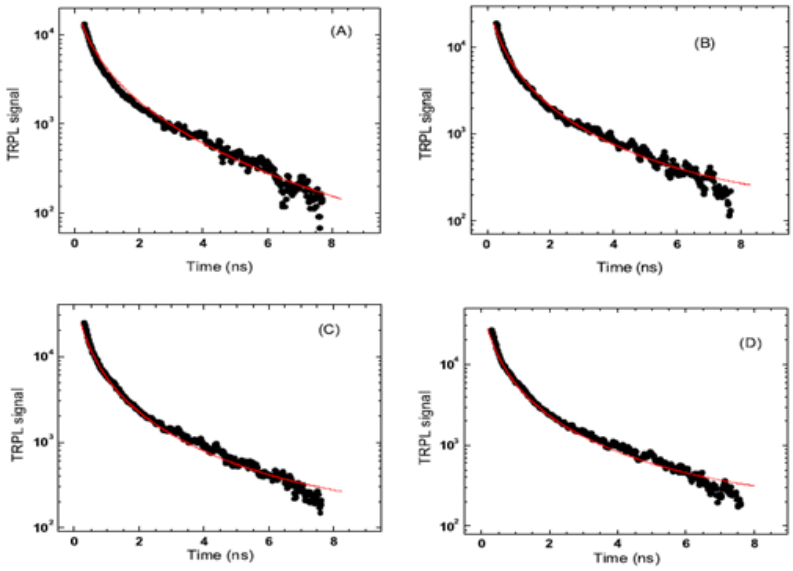

Figure 6.12. *TRPL curves obtained for excitation laser fluencies of: (A) 2.08 mJ cm^{-2}, (B) 4.5 mJ cm^{-2}, (C) 9.2 mJ cm^{-2}, (D)12.5 mJ cm^{-2}. The full line curves represent the best fit curves obtained through the multifitting procedure.*

Conclusions

In this work were studied the PL properties of ZnO both nanowires and bulk crystals. The first part of work examined the connection of emission properties of ZnO with possible applications of material as sensing device. The results suggest the response to environment is speed enough for gas sensing applications, moreover it is not too fast to induce dynamical quenching effects.

Then were shown the results regarding ZnO as candidate for light emitting material in blue / near UV region. First the connection between visible and UV emission was studied and then an analysis of UV emission leaded to the conclusions that in nanowires is possible to observe stimulated emission phenomena due to exciton-exciton scattering (p-line) that produces a diminishing of decay time, FWHM of spectrum and a superlinear increasing of emitted radiation as function of laser fluency. Moreover in nanowires the time delay between laser pulse and UV decay onset approaches to zero increasing pump intensity because of exciton scattering probability increasing in nanostructured samples. Instead the study of the bulk crystal doesn't show stimulated emission phenomena but only a red-shift of UV wavelength maximum due to many body effects.

Then the time resolved measurements were used to measure the conduction band electron density using a generalization of an existing technique. The same results were obtained using a multifitting procedure to fit all curves at same time with only one function.

A possible improvement of results obtained in this work is the measure of conduction band electron density in independent way (for example by means Hall effect) moreover, because the material parameters change near surface, the same measures adding spatial resolution could give information also in devices composed by different materials and so several interfaces.

Appendix A

Nd:YAG laser (detailed description)

The EKSPLA PL2143 (figure A1) is composed of a master oscillator that produces a train of pulses (about 5μJ energy) using a Nd:YAG rod as active medium, a regenerative amplifier in which the pulse is amplified to 500μJ and a power amplifier which amplifies the pulses up to 30 mJ by means of a double pass through another Nd YAG rod.

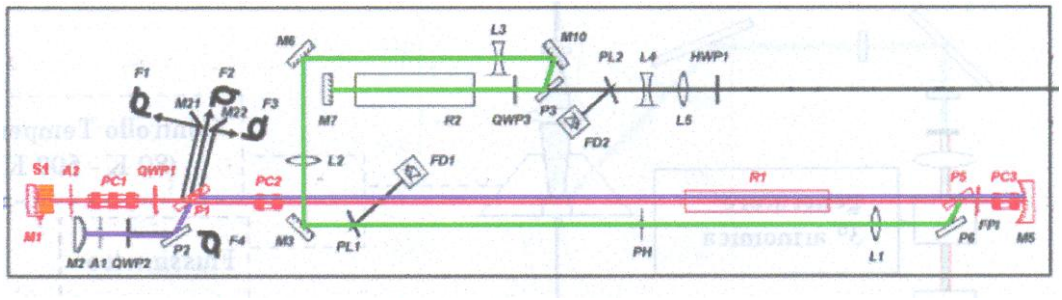

Figure A1

The master oscillator cavity consisting of a planar mirror M1 and a concave mirror M5 both with a reflectivity of 99.9%. The active medium is a Nd YAG rod (R1) placed in a diffusive chamber to ensure uniform illumination of medium.

The pulse formation is carried out by means of active and passive mode-locking.

To perform the dynamic losses a radio frequency modulated Pockels cell (PC1) and a polarizer (P1) are used.

When the potential is applied to PC1 the polarization of beam is rotated, resulting a variable transmission through P1 and then a variable attenuation.

The variable attenuation is modulated using a frequency that matches the round trip of cavity to accelerate the evolution of a single pulse. Moreover the variable attenuation is used to stabilize the energy of generated pulses using a negative feedback. A pin photodiode, connected to light-guide F2, measures the energy of beam component reflected by P1 and a voltage proportional to this quantity is applied to Pockels cell. The higher pulse energy the higher losses to ensure a pulse energy of 5 μJ, the actual pulse duration is about 16-20 ps.

A Fabry Perrot etalon (FP1), placed in the cavity, introduces frequency dependent losses and then narrows the spectral width of gain curve resulting a time broadening of pulse up to 25ps.

When a stable pulse is obtained in master generator, the PC2 Pockels cell rotates the beam polarization and P1, that now reflects the light, dumps the beam to regenerative amplifier.

The regenerative amplifier cavity comprises the mirrors M2 and M5, this branch is characterized by low optical losses and the pulsed is amplified to ~ 500μJ energy level.

In regenerative amplifier the beam passes several times in rod R1 to maximize the power then the Pockels cell rotates the polarization and dumps the beam to power amplifier. A small fraction of light is reflected by PL1 glass plate to photo-detector FD1 that measures pulse energy and displays it on keypad.

The lamp flash that pumps rod R1 has a 80μs duration, the start of flash triggers the start of RF generator (that applies the potential to PC1) and it is switched off after about 200μs.

When the generation starts (80-120μs after the flash start) a circuit triggers an electric pulse (SYNC 1) that in figure A2 is represented as time instant 2. SYNC 1 is a 2.8V signal which duration is about 2.5μs and it is directed to the SYNC 1 output that is observable on oscilloscope.

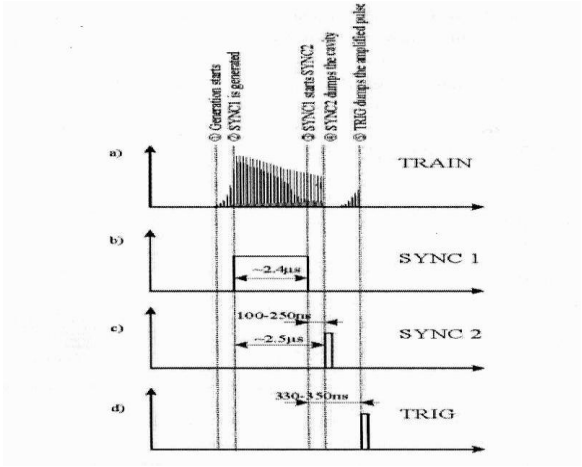

Figure A2

The falling edge of SYNC 1 (time instant 3) triggers two circuit, the first one starts the signal SYNC2 (time instant 4), and the other circuit starts the signal TRIG (time instant 5).

The SYNC 2 signal switches the PC2 cell then the polarization is rotated by 90^{o} and P1 directs the light to regenerative amplifier.

The first circuit tunes the delay between time instant 3 and 4 the, delay may be outward selected.

The second circuit starts an electric signal that switches on a driver which applies a voltage to PC3 Pockels cell. The beam, after passing two times through PC3 with resulting 90^{o} rotation, is reflected by P5 polarizer that dumps a single picoseconds pulse to power amplifier cavity. A number of optical components are placed beyond the P5 to filter the beam so only the TEM_{00} is transmitted to power amplifier.

In power amplifier the beam is amplified by means of another Nd YAG rod (R2) across which the beam passes two times. The amplification is tunable varying the delay between amplifier flash and generator flash, when the amplifier is off the pulse energy is 0,5 mJ on the contrary when the delay is optimum the pulse energy is 30mJ.

Appendix B

Streak Trigger

There are three basic methods of trigger's configuration apiece of kind of measurements (laser power, frequency repetition). In all these methods is needful a voltage signal applied in "Trig in " input of streak camera to trigger the start of sawtooth which delay is ruled varying BNC cable's length and using a delay unit that delays the electric signal of a tunable time between 0 and 32ns. This signal must arrive h ns before that light arrives in input slit, the h quantity depends on used time-range and it assumes values between 13 ns and 81 ns. The different trigger methods are: Not synchronized method, Enclosing Method and Sequential method.

In the first method the readout camera runs asynchronously to the streak camera.

When enclosing method is used the CCD is started and stopped by computer control. After start of an exposure the trigger starts. When all triggers have been processed the CCD camera exposure is ended by computer control and the resulting image is read out. This method is called "Enclosing method" since all action related to streak triggering happen during the exposure time of CCD camera (fig B1).

This method is useful when an high repetition laser is used.

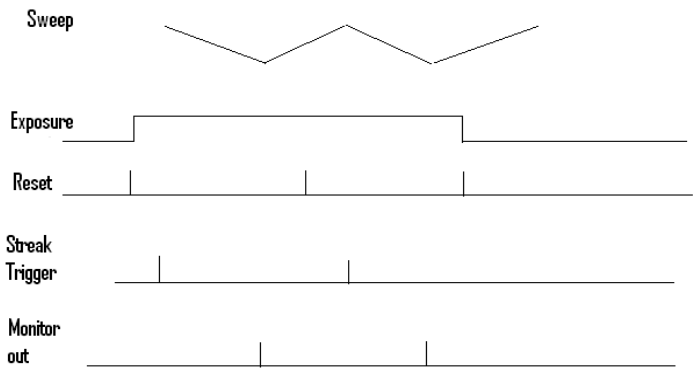

Figure B1

In the sequential method streak trigger and CCD camera exposure are done one after the other. The monitor out signal of streak camera triggers the start of exposure. The exposure time is defined by the user and fixed for all trigger events.

In this method the CCD is switch off during the time interval between two events and then the noise due to photon out of interesting time interval is suppressed.

The time diagram is shown below (figure B2).

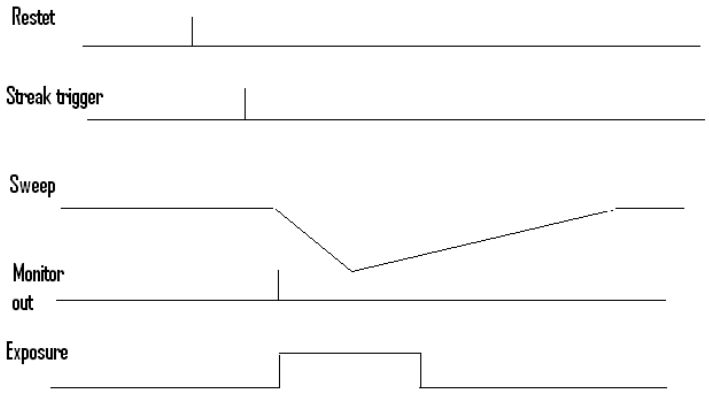

Figura B2

Gate mode

An useful way to suppress the noise due to incoming photons out of temporal window of interested phenomena is to switch off, when possible, the voltage of accelerating mesh and voltage of MCP (gate mode). There are three kind of gate mode:

Normal mode. The MCP is gated off during the post return sweep. In addition the horizontal blanking unit shifts off screen the post return sweep.

However, because the maximum repetition frequency of gate circuit is 10 kHz, the gate remains open for frequency of sweep larger than 10 kHz and only horizontal blanking unit operates to blank the return sweep up to 2 MHz. In normal mode only external trigger that triggers the sweep is needful. A gate trigger signal is not required and internal gating is synchronized with streak trigger and sweep range automatically.

Gate mode. In this mode operation of streak tube is limited to the interval of streak sweep. This mode reduces the background noise of incident light and the noise due to the dark current.

The external signal input in “gate trigger in” connector opens the gate (cathode + MCP) after about 300 ns. The external signal input in “streak trig” connector triggers the start of sweep, the completion of sweep is detected and the gate is automatically closed.

Ext mode. This mode allows to the streak tube to be operating for a desired period of time according to the pulse width of the gate trigger signal. The gate opens on the rising edge of the gate trigger input through the gate trig in connector, and closes on the failing edge. With this mode, the cathode gate remains open, and only the MCP gate functions.

References

[1] Haranath, Sonal Sahai, Amish G. Joshi, and V. Shanker NANOTECHNOLOGY (2009)

[2] Kohan, Ceder, Morgan PHYS. REW. B (2000)

[3] Van de Walle , PHYS. REW. LETT. (2000)

[4] Cox, Davis, Cottrell, King , PHYS. REW. LETT. (2001)

[5] Hoffmann, Hofstaetter, Leiter, Zhou , PHYS. REW. LETT. (2001)

[6] Nickel, Fleischer , PHYS. REW. LETT. (2003)

[7] Kim, Niki, Oh, Song, J. APP. PHYS. (2005)

[8] Park, Zhang, Wei, PHYS. REW. B (2002)

[9] Wardle, Goss, Briddon, PHYS. REW. B (2005)

[10] Wang, Wu, Webb, APP. PHYS. A (2003)

[11] Ryu, Zhu, Look, Wrobel, J. CRYSTAL GROWTH (2000)

[12] Look, Renlund, Burgener APP. PHYS. LETT. (2004)

[13] Tuomisto, Saarinen, Look, PHYS. REW. LETT. (2003)

[14] Vanheusden, Seager, Warren, Tallant, J. APP. PHYS. (1996)

[15] Studenikin, Golego, Cocivera, J. APP. PHYS. (1998)

[16] Lin, Fu, Jia, APP. PHYS. LETT. (2001)

[17] Garces, Wang, Bai, Giles APP. PHYS. LETT. (2002)

[18] Cox, Block, Hervé, Picard, SOLID STATE COMMUN.(1978)

[19] Garces, Giles, Halliburton, Cantwell, APP. PHYS. LETT. (2002)

[20] Cho, Ma, Kim, Sun, Wong, Ketterson APP. PHYS. LETT (1999)

[21] Chen, Liu, Ma, Zhao, Zhi, Lu, J. CRYST. GROWTH (2002)

[22] Mari, Manjon, Mollar, Cembrero, Gomez, APP. SURF. SCIENCE (2006)

[23] Wang, Lau, Lee, Yu, Tay, Zhang, Hng J. OF APPLIED PHYSICS (2003)

[24] Wang, Seo, Tin, Bozack, Williams, Park, Sathitsuksanoh, J. APP. PHYS. (2006)

[25] Shalish, Temkin, Narayanamurti PHYS. REW B (2004)

[26] Nobis, Kaidashev, Rahm NANO LETTERS (2004)

[27] Lagowski, Sproles, Gatos, J. APP. PHYS. (1977)

[28] Korsunska, Borkovska, Bulakh, J. LUMIN (2003)

[29] Jin, Tiwari, Narayan JOURNAL OF APPLIED PHYSICS (2005)

[30] Shih, Winkler, Voss, Mazur, APPLIED PHYSICS A (2009)

[31] Lu, Fujita JOURNAL OF APPLIED PHYSICS (2007)

[32] Deng, Zhang JOURNAL OF LUMINESCENCE (2008)

[33] Ye, Gu, Zhu, Liu, Zheng, Zhang, and Shi APPLIED PHYSICS LETTERS (2005)
[34] C.F. Klingshirn, SEMICONDUCTOR OPTICS, Springer
[35] Bagnall, Chen, Zhu, Yao, Shen, Goto APP. PHYS. LETT (1998)
[36] Yamamoto, Kido, Goto, Chen, Yao, and Kasuya, APP. PHYS. LETT (1999)
[37] G. P. Zhu, Xu, J. Zhu, Zheng, Liu, Lu, Cui OPTICAL MATERIAL (2008)
[38] Mariano, Zimmler, Bao, Capasso, Muller, Ronning APP. PHYS. LETT (2008)
[39] Zimmler, Voss, Ronning, Capasso APP.PHYS. LETT. (2009)
[40] Barry Bebb "SEMICONDUCTOR AND SEMIMETAL", Vol 8, chap 4, Academic Press
[41] Bassani Franco, Grassano Umberto, FISICA DELLO STATO SOLIDO, Bollati Boringhieri
[42] Ahrenkiel, Lundstrom, "Micority carrier lifetime in III-V semiconductors, Academic Press
[43] Faglia, Baratto, Sberveglieri, Zha,Zappettini, APP. PHYS. LETT. (2005)
[44] John B. Hudson, SCIENCE SURFACE, Wiley-Interscience
[45] Berberan, Santos, Bodunov, Valeur, CHEMICAL PHYSICS (2005) 171–182
[46] Blakemore, "Semiconductor statistics" Cap. 8, pag.250-254.
[47] Leung, Kwok, Djurisic NANOTECHNOLOGY (2005)
[48] Muth, Kolbas, Sharma, Oktyabrsky, Narayan, J. APP. PHYS. 85, 7884 (1999)
[49] Liang, Yoffe, PHYS. REV. LETT. 20, 59 (1968)